PERIODIC ERROR IN HETERODYNE INTERFEROMETRY: MEASUREMENT, UNCERTAINTY, AND ELIMINATION

By

HYO SOO KIM

A DISSERTATION PRESENTED TO THE GRADUATE SCHOOL
OF THE UNIVERSITY OF FLORIDA IN PARTIAL FULFILLMENT
OF THE REQUIREMENTS FOR THE DEGREE OF
DOCTOR OF PHILOSOPHY

UNIVERSITY OF FLORIDA

2009

To my wife, daughter, and son

ACKNOWLEDGMENTS

I would like to thank my advisor, Dr. Tony L. Schmitz, for his research guidance and moral support. It would have been impossible to complete this work without my family, so I would like to thank them from the bottom of my heart. Also, I gratefully acknowledge partial financial support from the National Science Foundation (Grant No. CMMI-0555645), the Korea Science and Engineering Foundation (Grant No. D00010), and a University of Florida Alumni Fellowship.

TABLE OF CONTENTS

LIST OF TABLES

LIST OF FIGURES

Abstract of Dissertation Presented to the Graduate School
of the University of Florida in Partial Fulfillment of the
Requirements for the Degree of Doctor of Philosophy

PERIODIC ERROR IN HETERODYNE INTERFEROMETRY: MEASUREMENT, UNCERTAINTY, AND ELIMINATION

By

Hyo Soo Kim

December 2009

Chair: Tony L. Schmitz
Major: Mechanical Engineering

The purpose of this study is to construct, test, and verify a new heterodyne displacement measuring interferometer design that eliminates the current accuracy limitation imposed by periodic error, which appears as a cyclical oscillation of the measured displacement about the true value during motion. In the new design, the two (heterodyne) frequencies are generated and spatially separated using acousto-optic modulators. By removing the potential for overlap and frequency mixing within the interferometer, periodic error is eliminated. The new concept replaces the traditional method of 'polarization coding', where the two beams (with different frequencies) are initially coincident with orthogonal polarization states and then separated using polarization dependent optics. Experimental results are presented for two arrangements of the new design at multiple target velocities. Spectral content (collected using an analog spectrum analyzer) is analyzed to verify zero periodic error. These results are compared to data collected using a traditional polarization coded heterodyne interferometer with variations in the optical alignment to demonstrate different levels of first and second order periodic error. Again, frequency spectrum data are provided.

CHAPTER 1
INTRODUCTION

Since its introduction in the mid-1960s, displacement measuring interferometry has offered high accuracy, range, and resolution for non-contact displacement measurement applications. Important examples include: 1) positional feedback of precision stages on photolithographic steppers for integrated circuit fabrication; 2) transducer calibration; and 3) positional feedback/calibration for machine tools, coordinate measuring machines, and other metrology systems. A common configuration choice in these situations is the heterodyne (or two frequency) Michelson-type interferometer with single, double, or multiple passes of the optical paths. These systems infer changes in displacement of a selected optical path by monitoring the optically induced variation in the photodetector current, which is generated from the optical interference signal. The phase measuring electronics convert this photodetector current to displacement using an assumed relationship between corresponding changes in detector current and displacement, where this relationship is defined by idealized performance of the optical elements.

Many error sources inherent to displacement measuring interferometers can be corrected or compensated by setup or additional metrology. Some of these errors are briefly introduced here and are described in detail in Chapter 2.

- Abbe – if the moving target is not located at the point of interest (e.g., the tool point in a machine tool), rotational error motions are converted to displacement errors by any offset;
- cosine – an angular misalignment between the interferometer's optical axis and motion direction leads to a measured displacement value which is smaller than the true value;

Reprinted with permission from Kim H, Schmitz T, Beckwith J. Periodic error in heterodyne interferometry: Examination and Elimination. In: Halsey D, Raynor W, ed. Handbook of Interferometers: Research, Technology and Applications. Hauppauge, NY: Nova Science; 2009.

- thermal expansion/contraction – changes in the optical dimensions with temperature can cause apparent displacements if the optical path lengths between the moving and fixed targets are not balanced; also, deformations of the support structure can cause errors;
- atmospheric – air refractive index, which relates the optical path difference to the geometric motion, depends on temperature, pressure, humidity, and composition; and
- deadpath – unequal path lengths at initialization (of the phase measuring electronics) accompanied by uncompensated refractive index variation during the measurement.

Others, such as laser wavelength stability and electronics error, are typically small (although non-negligible in some cases). Periodic error, however, remains an intrinsic error source that prevents traditional configurations from achieving sub-nanometer level accuracy. The purpose of this research is to validate the absence of periodic error in a new interferometer design that does not rely on polarization coding, where the two (heterodyne) optical frequencies are carried on coincident, linearly polarized, mutually orthogonal laser beams and are separated/recombined using polarization dependent optics. Rather, the two frequencies are carried on spatially separate beams in a polarization independent optical configuration that also enables the user to select the beat (or split) frequency. The new design is based on two acousto-optic modulators with different driving frequencies that function as beam splitters/recombiners. By eliminating the potential for mixing between the two heterodyne frequencies, the periodic error source is removed.

Figures 1-1 and 1-2 depict the simplest setups for the traditional polarization coded interferometer and the new design of the heterodyne displacement interferometer, respectively. In polarization coding, the f_2 frequency beam is (ideally) linearly polarized in the horizontal plane, while the collinear f_1 frequency beam is linearly polarized in the vertical plane. A polarization dependent beam splitter is then used to separate the two beams and direct them toward the moving and fixed targets, respectively. Inherent imperfections in the beam

polarization states and optics allow a portion of both frequencies to travel to the two targets. The resulting periodic error degrades the measurement system accuracy.

In this research, the two frequencies are kept spatially separate to avoid leakage into the unintended paths and eliminate periodic error. In the Figure 1-2, the f_2 (up-shifted frequency) beam generated by the acousto-optic modulator (AOM) travels to the moving target, while the f_1 beam from the single frequency, Helium-Neon laser source travels separately to the fixed target. After reflection, the two beams interfere during their return path through the AOM without the possibility for frequency leakage and corresponding periodic error. No other optical components are required. This is an important consideration because the existence of first or second order periodic errors[1], with amplitudes that vary cyclically with the target position, leads to nonlinear performance and limits the achievable accuracy.

In addition to constructing the new heterodyne displacement measuring interferometer, the calculation of first and second order periodic error from spectrum analyzer data is also analyzed and the displacement measurement uncertainty is evaluated. Identifying the magnitude of periodic error for a particular setup enables alignment adjustments to be made to minimize the error magnitude. The calculation of periodic error magnitude, which builds on a prior analysis [2] that considered each error order individually, is completed for the general case. A single expression is developed for calculating both first and second order error magnitudes from spectrum analyzer data.

The typical approach for displacement interferometry uncertainty analysis is to evaluate the uncertainty due to the individual error sources and then combine them in a root sum squares manner to represent the total uncertainty [3, 4]. In this work, a single expression for displacement

[1] First and second order periodic errors exhibit spatial frequencies of one and two cycles per displacement fringe, respectively.

including all significant error sources is presented and its uncertainty is evaluated using Monte Carlo simulation. The uncertainty due to periodic error, described using the analytical model developed by Cosijns *et al*. [5], is also included. The remaining chapters describe this work in detail.

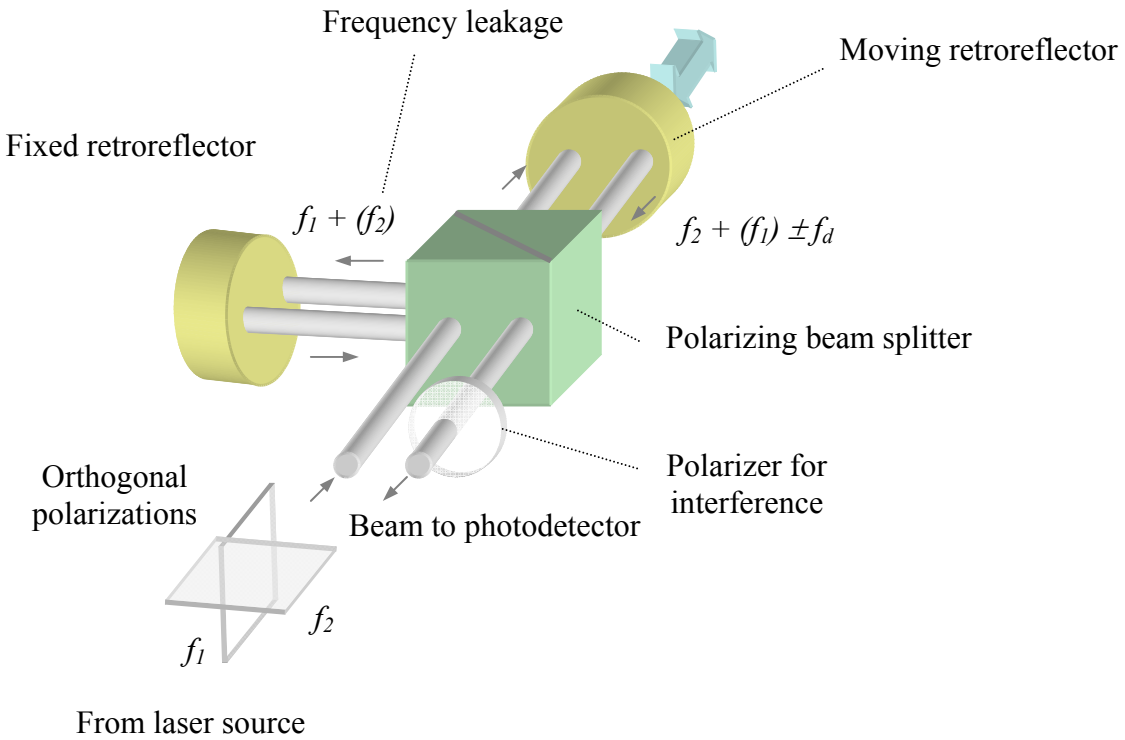

Figure 1-1. A simple polarization coded heterodyne interferometer where the two beams are overlapped and imperfectly separated.

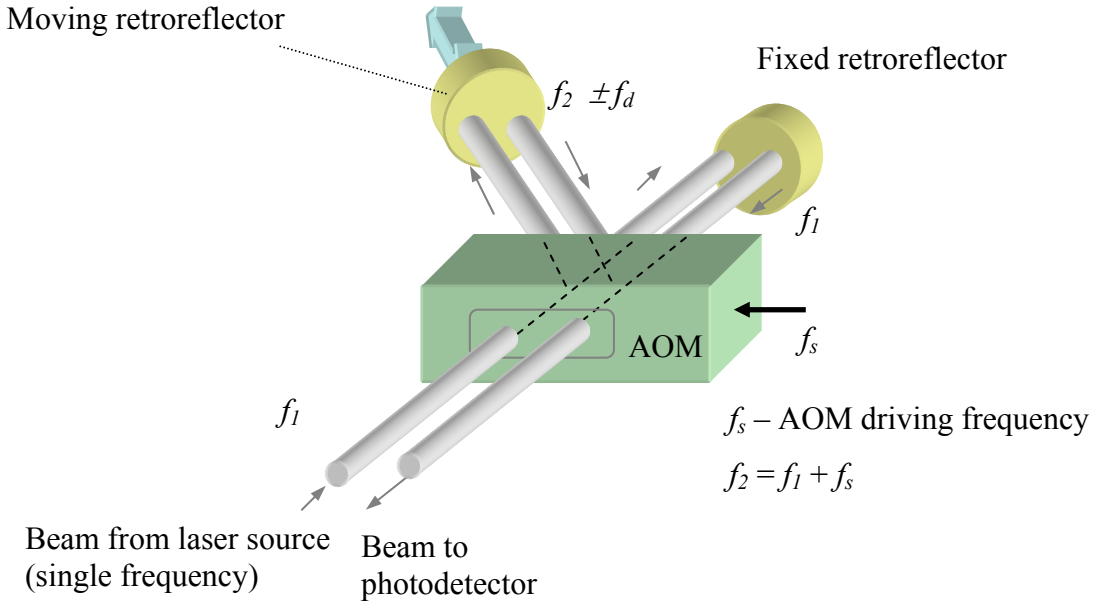

Figure 1-2. New heterodyne interferometer design that uses an acousto-optic modulator (AOM) to eliminate frequency mixing.

CHAPTER 2
BACKGROUND

Introduction

Interferometry is a technique for diagnosing the properties (i.e., magnitude, phase, and frequency/wavelength) of two or more light waves by analyzing the pattern of interference generated by their superposition. The instrument used to generate interference of the light waves is called an interferometer. Interferometry plays an important role in the fields of astronomy, engineering metrology, optical metrology, and many others. One common interferometer is the Michelson interferometer used to measure displacement [6]. In this chapter, two types of the Michelson interferometer are introduced. Also, the error sources for one of the two types, the heterodyne displacement measuring interferometer, are described.

Since interferometry is based on the physical phenomenon of the interference of light, understanding the basic concepts of interference is essential. These concepts are introduced in the following sections.

Light Waves

Light can be described as a transverse electromagnetic wave propagating through space. Since the electric and magnetic fields are orthogonal to each other and propagate together as shown in Figure 2-1, it is usually sufficient to consider only the electric field at any point [6].

The electric field can be treated as a time-varying vector perpendicular to the direction of propagation of the wave. If the field vector always lies in the same plane, the light wave is said to be linearly polarized in that plane. The electric field at any point due to a light wave propagating along the z direction is then described by Eq. 2-1,

$$E(x,y,z,t) = E_0 \cos\left[2\pi\left(ft - z/\lambda\right)\right] \tag{2-1}$$

where E_0 is the amplitude of the light wave, f is its frequency, and λ is its wavelength. The term within the square bracket, called the phase of the wave, varies with time as well as with distance along the z-axis from the origin. With varying time, a light wave specified by Eq. 2-1 moves along the z-axis with a speed of [6],

$$c = f\lambda_{vac} \tag{2-2}$$

where c is the speed of light in a vacuum, approximately 3 x 10^8 m/s and λ_{vac} is the vacuum wavelength. In a medium with a refractive index, n, the speed of the light wave is expressed by Eq. 2-3.

$$v = \frac{c}{n} \tag{2-3}$$

Since its frequency remains unchanged, its wavelength is determined by Eq. 2-4,

$$\lambda = \frac{\lambda_{vac}}{n}. \tag{2-4}$$

Equation 2-1 can be rewritten in a compact form according to Eq. 2-5,

$$E(x, y, z, t) = E_0 \cos(\omega t - kz) \tag{2-5}$$

where $\omega = 2\pi f$ is the circular frequency and $k = 2\pi/\lambda$ is the propagation constant.

The representation of a light wave in terms of a cosine function in Eq. 2-5 is easy to visualize, but not well adapted to mathematical manipulation. It is often convenient to use a complex exponential representation as shown in Eq. 2-6 [7],

$$\begin{aligned} E(x, y, z, t) &= \mathrm{Re}\left[E_0 e^{i(\omega t - kz)}\right] \\ &= \mathrm{Re}\left[A e^{i\omega t}\right] \end{aligned} \tag{2-6}$$

where $A = E_0 e^{-i\phi}$ is known as the complex amplitude and $\phi = kz = 2\pi z/\lambda$.

The energy of the electromagnetic radiation per unit area is proportional to the time average of the square of the electric field as shown in Eq. 2-7 [7],

$$\begin{aligned}
\left\langle E^2 \right\rangle &= \lim_{T\to\infty} \frac{1}{2T} \int_{-T}^{T} E^2 dt \\
&= \lim_{T\to\infty} \frac{1}{2T} \int_{-T}^{T} \left(E_0 \cos\left(\omega t - kz\right)\right)^2 dt \\
&\text{Expand to obtain:} \\
&= \lim_{T\to\infty} \frac{E_0^2}{2T} \int_{-T}^{T} \frac{1+\cos 2\left(\omega t - kz\right)}{2} dt \\
&= \frac{E_0^2}{2} + \underbrace{\lim_{T\to\infty} \frac{E_0^2}{4T} \int_{-T}^{T} \cos 2\left(\omega t - kz\right) dt}_{\text{time average of cosine function is zero}} \\
&= \frac{E_0^2}{2}
\end{aligned} \tag{2-7}$$

where T is the averaging time. The intensity of electric field can be expressed as the square of the complex amplitude; see Eq. 2-8,

$$\begin{aligned}
I &= \frac{1}{2} E_0^2 \\
&= \frac{1}{2}\left(AA^* \right) \\
&= \frac{1}{2}\left| A \right|^2
\end{aligned} \tag{2-8}$$

where A^* is the complex conjugate of A.

Interference of Light

When two light waves are superimposed, the resultant intensity at any point depends on whether they interfere constructively (in phase) or destructively (out of phase) [6]; see Figures 2-2 and 2-3. Given that the two light waves are propagating in the same direction, both are linearly polarized, and they have different amplitudes and the same frequency with a phase difference, $\Delta\phi$, they can be described according to Eq. 2-9,

$$
\begin{aligned}
E_1 &= E_{01}\cos\left(\omega t - kz\right) \\
E_2 &= E_{02}\cos\left(\omega t - kz + \Delta\phi\right)
\end{aligned}
\tag{2-9}
$$

where E_{01} and E_{02} are the amplitudes of E_1 and E_2, respectively. Equation 2-10 shows the complex exponential representations of the two waves,

$$
\begin{aligned}
E_1 &= \mathrm{Re}\left(A_1 e^{i\omega t}\right) \\
E_2 &= \mathrm{Re}\left(A_2 e^{i\omega t}\right)
\end{aligned}
\tag{2-10}
$$

where $A_1 = E_{01}e^{-i\phi_1}$ and $A_2 = E_{02}e^{-i\phi_2}$ are the complex amplitudes and $\phi_1 = kz$ and $\phi_2 = kz - \Delta\phi$. The resultant wave, E, after superposition is then given by the sum of the two waves, E_1 and E_2. See Eq. 2-11.

$$
\begin{aligned}
E &= E_1 + E_2 \\
&= E_{01}\cos\left(\omega t - kz\right) + E_{02}\cos\left(\omega t - kz + \Delta\phi\right) \\
&= \mathrm{Re}\left(A_1 e^{i\omega t}\right) + \mathrm{Re}\left(A_2 e^{i\omega t}\right)
\end{aligned}
\tag{2-11}
$$

The intensity of the resultant wave is then half of the square of the sum of the two complex amplitudes as shown in Eq. 2-12,

$$
\begin{aligned}
I &= \frac{1}{2}\left|A_1 + A_2\right|^2 \\
&= \frac{1}{2}\left(A_1 + A_2\right)\left(A_1^* + A_2^*\right) \\
&= \frac{1}{2}\left(A_1 A_1^* + A_2 A_2^* + A_1 A_2^* + A_2 A_1^*\right) \\
&= \frac{1}{2}\left(E_{01}^2 + E_{02}^2 + E_{01}E_{02}e^{i(\Delta\phi)} + E_{01}E_{02}e^{-i(\Delta\phi)}\right) \\
&= I_1 + I_2 + 2\sqrt{I_1 I_2}\cos\left(\Delta\phi\right)
\end{aligned}
\tag{2-12}
$$

where I_1 and I_2 are the intensities due to the two waves and the third term is the intensity due to interference between the two waves.

The Michelson Interferometer

The Michelson interferometer was first introduced by Albert Michelson in 1881 [6]. It has played a vital role in the development of modern physics. A schematic of the Michelson interferometer is shown in Figure 2-4. From an extended light source, S, beam 1 is split by a semireflective coating on the surface of a beam splitter. The same beam splitter is used to recombine the beams reflected back from the two mirrors, M1 and M2. The recombined beam (beam 4) leaves the interferometer and the interference pattern is imaged on the screen. To align the beams, at least one of the mirrors is equipped with a tilting mechanism that allows the surface of M1 to be made perpendicular to that of M2. Also, one of the mirrors is movable along the beam direction to generate an optical path difference between beams 2 and 3.

When using a white light source [8] to obtain the interference fringes in the Michelson interferometer, the two optical path lengths must be equal for all wavelengths [6]. Therefore, both arms must contain the same thickness of glass having the same dispersion. However, beam 3 traverses the beam splitter three times while beam 2 traverses it only once. Accordingly, a compensating plate (identical to the beam splitter, but without the semireflective coating) is inserted in the path of beam 2.

Some important developments have extended the scope and accuracy of displacement measurements made using the Michelson interferometer. These include the invention of the laser, photodetector, optical fibers, and digital electronics for signal processing. The schematic of the Michelson interferometer equipped with these improvements is shown in Figure 2-5. The extended light source is replaced by the laser, which produces monochromatic (single wavelength) light, and the screen used to observe the interference fringes is replaced by a photodetector. Digital electronics are added after the photodetector to interpret the measurement signal, either intensity variation or phase change depending on the interferometer type

(homodyne or heterodyne, which are described in next section) and convert the fringe information to displacement.

Two Displacement Measuring Interferometer Types

Two types of the Michelson interferometer are commonly used for displacement measurements. A homodyne displacement measuring interferometer uses a single frequency laser head and the intensity variation induced by interference is converted into displacement. A heterodyne displacement measuring interferometer, on the other hand, uses a two-frequency laser as a light source and determines displacement from the phase change between the measurement and reference signal. The homodyne approach is briefly described in the next section, while the heterodyne approach used in this research is discussed in more detail in the subsequent section.

Since the Michelson-type interferometer is implemented with a certain configuration (i.e., single, double or multiple passes of the optical path), the characteristics and implementations of the single pass and double pass configurations are introduced before proceeding to a description of the two interferometer types. In the single pass configuration shown in Figure 2-6, a beam having both the vertical, V, and horizontal, H, polarization components splits at a polarizing beam splitter (PBS). Conventionally, the polarizing beam splitter transmits the horizontally polarized beam while the vertically polarized beam is reflected. The reflected beam, referred to as the reference beam, travels toward the fixed retroreflector and returns to the polarizing beam splitter. The transmitted beam, referred to as the measurement beam, is reflected from the moving retroreflector where phase change occurs during the target motion. The measurement and reference beams are recombined at the polarizing beam splitter and interfered after passing through a linear polarizer (LP) which makes the same polarization plane for the two beams by orienting the transmission axis (TA) at 45 deg with respect to the vertical axis.

The path change for the measurement beam is twice the displacement of the target in the single pass interferometer. In other words, the phase change, $\Delta\phi_{\text{single}}$, of the measurement beam due to the target motion is proportional to twice the target displacement; see Eq. 2-13,

$$\Delta\phi_{\text{single}} \propto 2d \tag{2-13}$$

where d is the displacement of the target.

Assume that the initial phases of the measurement and reference beams are the same at the initial position as shown in Figure 2-7A. That is, the two waves interfere constructively so that bright light is detected for the static case. When the target moves $\lambda/4$, where λ is the wavelength of the beam, the phase of the measurement beam changes by π rad as shown in Figure 2-7B which leads to destructive interference (i.e., no light at the detector). Another movement of the target by $\lambda/4$ in the same direction changes the measurement beam phase by 2π rad so that the constructive interference occurs; see Figure 2-7C.

The bright-dark-bright pattern induced by the interference of the two beams during the target motion is defined as a fringe, where one fringe is referred to as the optical resolution. The optical resolution of the single pass system is half of the source wavelength as shown in Figure 2-7D. Therefore, the total displacement of the target in the single pass interferometer can be determined by multiplying the number of fringes by $\lambda/2$; see Eq. 2-14.

$$d = \frac{\lambda}{2} \times (\text{\# of fringes}) \tag{2-14}$$

Figure 2-8 shows a schematic of a double pass configuration, where the retroreflectors are replaced by plane mirrors and quarter wave plates are added. The quarter wave plate (QWP) retards the phase of an incident beam by $\pi/2$. When a linearly polarized beam transmits through a QWP, the polarization state is converted to circular [6].

The vertically polarized reference beam is reflected at the polarizing beam splitter and passing through the upper QWP, converting the state of polarization to circular. The reflected beam from the fixed plane mirror passes through the QWP again, which converts the circular polarization state to linear, but in the horizontal plane so that the polarizing beam splitter now transmits it. The offset beam reflected from the retroreflector passes through the polarizing beam splitter and the QWP, converting from linear (horizontal) to circular polarization. The circularly polarized beam passes back through the QWP on the return path from the fixed mirror, is converted back to a vertical polarization, and is directed to the detector by reflecting at the beam splitter. The transmitted horizontally polarized measurement beam from the source follows a similar path to the moving plane mirror. This behavior may be modeled analytically using the Jones vector/matrix notation. Readers may find more information on describing polarization states using Jones vectors and Jones matrices in reference [6].

Unlike the single pass configuration, the measurement beam travels four times more than the target in the double pass system. The phase change, $\Delta\phi_{\text{double}}$, due to the target motion is therefore proportional to four times the target displacement.

$$\Delta\phi_{\text{double}} \propto 4d \tag{2-15}$$

Again, assume that the initial phases of the measurement and reference beams are the same at the initial position as shown in Figure 2-9A. Then, constructive interference occurs (i.e., bright light is detected) prior to motion. When the target moves by $\lambda/8$, the phase of the measurement beam changes by π rad which leads to the 180 deg out of phase condition with respect to the reference beam phase. In that case, the two beams destructively interfere and no light is detected as shown in Figure 2-9B. If the target moves by an additional $\lambda/8$ in the same direction, constructive interference occurs; see Figure 2-9C.

In the double pass configuration, one fringe is obtained for motion equal to $\lambda/4$ as shown in Figure 2-9D. That is, the optical resolution of the double pass interferometer is twice that of the single pass interferometer. The total displacement of the target in the double pass interferometer can be determined by multiplying the number of fringes by $\lambda/4$; see Eq. 2-16.

$$d = \frac{\lambda}{4} \times (\text{\# of fringes}) \tag{2-16}$$

Homodyne Displacement Measuring Interferometer

In homodyne interferometry, a single frequency laser is used as a light source and intensity variation due to constructive/destructive interference is converted into displacement [9]. A homodyne interferometer system consists, at minimum, of a laser source, beam splitter, retroreflectors, photodetector and measurement electronics as shown in Figure 2-10. A single frequency, linearly polarized beam oriented at 45 deg with respect to the vertical axis from, typically, a Helium-Neon laser head is split into two beams at the polarizing beam splitter. One of the beams is reflected to the fixed retroreflector while the other beam is transmitted to the moving retroreflector. They recombine at the polarizing beam splitter where the beam reflected from the fixed retroreflector remains at the same frequency while the frequency of the beam from the moving retroreflector is shifted by the Doppler frequency. The interference signal is passed through intensity measuring electronics to count fringes equivalent to half the wavelength of the laser source (λ = 633 nm for a He-Ne laser) in the single pass system. Since the frequencies of the two beams are the same and the phase change (or frequency shift) is caused by the Doppler shift due to target motion, the intensity variation detected on the photodetector in the homodyne interferometer is the same as in Eq. 2-12.

Some limitations to the simple homodyne system include the inability to detect the direction sense of the target when motion is stopped and sensitivity to changes in the laser power

and ambient light intensity. To resolve these limitations, the detector configuration in the system can be modified, but this adds system complexity.

Heterodyne Displacement Measuring Interferometer

A heterodyne interferometer system uses two frequencies and measures the phase change between the fixed and moving arms [10]. A schematic of a single pass heterodyne interferometer is provided in Figure 2-11. Two polarized beams having slightly different frequencies are generated using either a Zeeman approach, where two frequencies are obtained by placing a magnetic field around the laser tube, or by combining a single frequency laser with an acousto-optic modulator, which produces a second diffracted beam with a modulated frequency [11] .The two beams with different frequencies are made collinear with orthogonal polarizations, which allows a polarizing beam splitter to separate them based on polarization state.

The frequency f_1 beam is reflected at the polarizing beam splitter and travels to the fixed retroreflector, while the frequency f_2 beam transmits through the beam splitter and travels to the moving retroreflector. The f_2 beam is reflected from the moving retroreflector and is shifted (by the Doppler frequency f_d) due to target motion. The two beams are then recombined at the beam splitter and directed to the detector. Since the polarization states are orthogonal, a linear polarizer (LP) with a 45 deg transmission axis is inserted in the beam path to produce interference.

The intensity variation of the two interfered beams is now investigated. The two light waves, E_1 and E_2, with amplitudes, E_{01} and E_{02}, and angular frequencies, ω_1 ($2\pi f_1$) and ω_2 ($2\pi f_2$), propagate to the fixed (path1) and moving (path2) retroreflectors (as shown in Figure 2-11), respectively. See Eq. 2-17.

$$\begin{aligned} E_1 &= E_{01}\cos\left(\omega_1 t - k_1\left(FF\right)x_1 + \phi_1\right) \\ E_2 &= E_{02}\cos\left(\omega_2 t - k_2\left(FF\right)x_2 + \phi_2\right) \end{aligned} \tag{2-17}$$

In Eq. 2-17, the second terms in the parentheses, $k_i(FF)x_i$, where i = 1 and 2, are the values of the phase changes due to the motions of both the fixed (x_1) and moving (x_2) retroreflectors. As described in the earlier section, $k_i = 2\pi/\lambda_i$ is the propagation constant (λ_i is the wavelength) and FF is the fold factor (equal to 2 for a single pass and 4 for a double pass configuration). The phase change ($k_1(FF)x_1$) of the wave E_1 is zero because there is no motion of the fixed retroreflector ($x_1 = 0$). On the other hand, the phase change ($k_2(FF)x_2$) of the wave E_2 is produced due to the motion of the moving retroreflector. The initial phases, ϕ_1 and ϕ_2, described in Eq. 2-17, represent the kz term in Eq. 2-5. Equation 2-17 can be rewritten as shown in Eq. 2-18 by letting $\Delta\omega = \omega_2 - \omega_1$ and substituting zero for $k_1(FF)x_1$.

$$\begin{aligned} E_1 &= \mathrm{Re}\left(A_1 e^{i\omega_1 t}\right) \\ E_2 &= \mathrm{Re}\left(A_2 e^{i\omega_1 t}\right) \end{aligned} \tag{2-18}$$

The complex amplitudes are $A_1 = E_{01}$ and $A_2 = E_{02}e^{i\left(\Delta\omega t - k_2(FF)x_2\right)}$. Note that the initial phases are assumed to zero. When they interfere by passing through the linear polarizer, the resultant wave, E, in Eq. 2-19, is the sum of the two waves.

$$\begin{aligned} E &= E_1 + E_2 \\ &= \mathrm{Re}\left(A_1 e^{i\omega_1 t}\right) + \mathrm{Re}\left(A_2 e^{i\omega_1 t}\right) \end{aligned} \tag{2-19}$$

The interference between the waves produces a sinusoidal current variation in the photodetector with a frequency difference, $\Delta f = \Delta\omega/2\pi = f_2 - f_1$, which is referred to as the beat or split frequency; see Eq. 2-20. The terms in the parenthesis give the phase of interfered waves. The phase change, $\Delta\phi$, is induced by motion of the target. If there is no motion, the phase change is zero and the output frequency of the interference signal remains at the split frequency. Therefore,

the operating point of a system is shifted from 0 Hz (DC) for a homodyne interferometry system to the split frequency, Δf , for a heterodyne system.

$$\begin{aligned} I &= \frac{1}{2}\left|A_1 + A_2\right|^2 \\ &= \frac{1}{2}\left(A_1 + A_2\right)\left(A_1^* + A_2^*\right) \\ &= \frac{1}{2}\left(\mathrm{E}_{01}^2 + E_{02}^2 + E_{01}E_{02}e^{-i\left(\Delta\omega t - k_2\left(FF\right)x_2\right)} + E_{01}E_{02}e^{i\left(\Delta\omega t - k_2\left(FF\right)x_2\right)}\right) \\ &= I_1 + I_2 + 2\sqrt{I_1 I_2}\cos\left(\Delta\omega t - \underbrace{k_2\left(FF\right)x_2}_{\text{phase change, }\Delta\phi}\right) \end{aligned} \tag{2-20}$$

Figure 2-12 shows the interference signal as displayed by a spectrum analyzer for both homodyne (Figure 2-12B) and heterodyne interferometer system (Figure 2-12C). The phase change, $\Delta\phi$, during target motion is given by Eq. 2-21,

$$\Delta\phi = \left(FF\right)\frac{2\pi n}{\lambda_{vac}}vt \tag{2-21}$$

where λ_{vac} is the vacuum wavelength, n is the refractive index of the medium in which the measurement occurs, v is the velocity of the target motion, and t is time.

The intensity expression, Eq. 2-20, can be rewritten to isolate the frequency shift caused by target motion. See Eq. 2-22.

$$I = I_1 + I_2 + 2\sqrt{I_1 I_2}\cos\left[2\pi\left(\Delta f - \frac{(FF)n}{\lambda_{vac}}v\right)t\right] \tag{2-22}$$

The resulting Doppler frequency shift, f_d, is proportional to the target velocity. The sign of the frequency shift depends on the direction of motion so that heterodyne system enables direction sensing by monitoring the sign of the Doppler frequency. See Eq. 2-23.

$$f_d = \frac{\left(FF\right)n}{\lambda_{vac}}v \tag{2-23}$$

The total phase difference is then the integral of the frequency shift, as shown in Eq. 2-24, and is directly related to the displacement, *d*; see Eq. 2-25.

$$\begin{aligned}\Delta\phi &= 2\pi\int_0^t \frac{(FF)nv}{\lambda_{vac}}dt \\ &= (FF)\frac{2\pi n}{\lambda_{vac}}d\end{aligned} \tag{2-24}$$

$$d = \frac{1}{FF}\frac{\lambda_{vac}}{2\pi n}\Delta\phi \tag{2-25}$$

Therefore, if the total phase difference is measured, the displacement can be determined.

In order to measure the phase difference, the reference signal[1] is needed to be compared to the measurement signal. There are two ways to generate the reference signal as shown in Figure 2-13. An internal reference signal can be directly derived within the laser head (beam 1) [12] or an external reference signal can be obtained using a non-polarizing beam splitter immediately after the laser output (beam 2). The measurement and reference beams are launched into photodetectors which convert the optical signals to electrical signals. The phase measuring electronics measure the total phase change for both the measurement and reference signals, then subtract the measured phase of the reference signal from that of the measurement signal to determine their phase difference; see Figure 2-14. The following section describes a phase measuring technique that is used in commercially-available phase measuring electronics.

Phase Measurement

There are several approaches to measure the phase of a signal such as the traditional analog phase measuring technique and the phase digitizing technique [13]. In this section, the phase digitizing technique used in this research is described. Figure 2-15 is a flow chart that shows how

[1] The interference signal of the two heterodyne frequencies (prior to reaching the interferometer) is $I_{ref} = I_1 + I_2 + 2\sqrt{I_1 I_2}\cos(\Delta\omega t)$. Naturally, this signal does not contain the Doppler phase shift.

the phase is determined from the incoming analog signal for both the reference signal (channel 1) and the measurement signal (channel 2). Since the signal processing procedure for both signals is the same, only the phase determination for the measurement signal is described.

An optical interference signal, Eq. 2-26, is converted into an electrical signal, Eq. 2-27, by a photodetector, composed of photovoltaic cells which converts light (i.e., photo) into electricity (i.e., voltaic).

$$E = E_0 \cos\left(2\pi f_{\text{meas}} t - \phi\right) \tag{2-26}$$

$$V = V_0 \cos\left(2\pi f_{\text{meas}} t - \phi\right) \tag{2-27}$$

In Eqs. 2-26 and 2-27, f_{meas} is the frequency of the incoming measurement signal ($\Delta f + f_d$), ϕ is the initial phase (or phase error in [13]), and E_0 and V_0 are the amplitudes of the electric field and current, respectively. The analog electrical signal is digitized at a sampling rate of 80 MHz by a 12 bit analog-to-digital converter (ADC). The digitized data sampled at 80 MHz is then divided by 256 (with a modula-256 counter) which slows the phase to 312.5 kHz (80 MHz divided by 256).

Within the 3.2 μs time frame (the period of 312.5 kHz digitized data), the frequency, f_{meas} is assumed to be constant. The initial frequency estimation is illustrated in Figure 2-16. The first step is to capture N samples (2048 for the electronics used in this study) of the digitized signal sampled at 80 MHz. The discrete Fourier Transform (DFT) is then performed on the captured data set. Next, the cell number (or index) of the frequency axis, k, with the largest transform modulus (i.e., the square root of the sum of the real and imaginary parts of the cell) is identified. Finally, the initial frequency is estimated by $k \times$ [sampling rate (80 MHz)]/N. This initial frequency is used to begin the linear regression to determine the amplitude of the signal (V_0) and the initial phase (ϕ) in Eq. 2-27.

Equation 2-27 can be expanded to form Eq. 2-28. There are 256 values on the left hand side of Eq. 2-28

$$V_0 \cos\left(2\pi f_{\text{meas}} t - \phi\right) = V_0 \cos\left(2\pi f_{\text{meas}} t\right)\cos(\phi) + V_0 \sin\left(2\pi f_{\text{meas}} t\right)\sin\left(\phi\right) \tag{2-28}$$

On the right hand side, $\cos\left(2\pi f_{\text{meas}} t\right)$ and $\sin\left(2\pi f_{\text{meas}} t\right)$ are provided by cosine and sine look-up tables for 256 values of time, t. Note that the frequency, f_{meas}, in the cosine and sine functions is the initial frequency, which is estimated as described in the previous paragraph and is used only once for the first segment of the data analysis. This forms a system of 256 equations and two unknowns, X_c and X_s, where $X_c = V_0 \cos\left(\phi\right)$ and $X_s = V_0 \sin\left(\phi\right)$. Linear regression is applied to determine the best-fit values of X_c and X_s. Accordingly, V_0 and ϕ are obtained after a polar-to-rectangular transformation as shown in Eq. 2-29.

$$\begin{aligned} V_0 &= \sqrt{X_c^2 + X_s^2} \\ \phi &= \tan^{-1}\left(\frac{X_s}{X_c}\right) \end{aligned} \tag{2-29}$$

The output phase of the segment, ϕ_{seg}, is estimated by integrating the latest frequency estimation (a phase accumulator performs the integration) and updated by adding the initial phase, ϕ, obtained by linear regression. See Eq. 2-30:

$$\phi_{\text{seg}} = \int_a^b f_{\text{update}} dt + \phi\,, \tag{2-30}$$

where $a = 0$ and $b = 3.2$ μs in this research and f_{update} is the frequency updated using the latest phase of the segment. As noted, the initial frequency is used for the phase determination of the first segment of data. The phase of the first segment is stored in a phase accumulator and the phases for the subsequent segments are estimated and accumulated to determine the total phase of the measurement signal, ϕ_{meas}. Since frequency is the derivative of phase, it can be estimated

by taking the finite difference between the latest two successive phase outputs divided by the time increment (3.2 μs). This updated frequency, f_{update}, is used in the linear regression for the next segment.

The total phase for the reference signal, ϕ_{ref}, can be determined using the same process. The phase difference, $\Delta\phi = \phi_{\text{meas}} - \phi_{\text{ref}}$, between the two phases is finally calculated and converted into displacement in the electronics using Eq. 2-25.

Error Sources in Heterodyne Interferometry

In this section, the errors in a heterodyne system are reviewed. Each error source is described briefly and compensations or corrections for the errors are discussed. Errors in heterodyne interferometry can be divided into three primary categories: environmental errors, geometry errors, and system errors, as shown in Figure 2-17 [14].

Atmospheric Error

The refractive index of a medium is a function of its density, which depends, for air, on temperature, pressure, and composition. Since most displacement measuring interferometers operate in air, it is necessary to identify the local refractive index. Any changes in the air's refractive index due to changes in the atmospheric conditions during a measurement introduce an apparent displacement which degrades the measurement accuracy. Atmospheric error can be expressed as shown in Eq. 2-31, where Δn is the refractive index variation and PD is the physical displacement of the moving target. The error caused by the refractive index variation is often the largest component in the error budget [14]. Therefore, it must be compensated.

$$\text{Atmospheric Error} = \Delta n \times PD \tag{2-31}$$

The refractive index can be estimated by a direct measurement of index using a wavelength tracker, which measures changes in the air's refractive index, or by using an empirical expression.

For the latter, the air pressure, temperature and relative humidity, are measured and these values are substituted into an appropriate equation [15] to approximately determine the refractive index during the measurement.

Material Thermal Expansion Error

Since the mechanical parts' dimensions in the interferometer are a function of temperature (due to thermal expansion or contraction), it is required to correct for this dimensional variation. This requires that the temperature of the part and its coefficient of linear thermal expansion are known.

Optics Thermal Drift

Temperature changes of the optical components during the measurement can also cause measurement error. When a change in temperature occurs, the physical size of the optical elements will vary which causes an apparent displacement. Optical thermal drift can be reduced by either controlling the temperature of the measurement environment or by using an optical configuration that is insensitive to temperature changes.

Deadpath Error

Deadpath error is caused by an uncompensated change in refractive index combined with a difference in length between the fixed and moving paths at initialization. A conventional linear interferometer with unequal path lengths is shown in Figure 2-18A. The measurement beam, f_2, has a longer path length than the reference beam, f_1, by the deadpath length, *DP*.

Even in the absence of moving target motion, an apparent displacement is caused by any uncompensated refractive index change over the deadpath, *DP*. Deadpath error can be expressed as shown in Eq. 2-32. This leads to a shift in the initialized position and, therefore, causes

measurement error. In most applications, deadpath errors can be minimized by reducing the deadpath length, as shown in Figure 2-18B. The interferometer is located at its initial position.

$$\text{Deadpath Error} = \Delta n \times DP \tag{2-32}$$

Abbe Error

Abbe error occurs when the measurement axis of interest is offset from the actual measurement axis and angular errors exist in the positioning system. Abbe error can be expressed as shown in Eq. 2-33,

$$\text{Abbe error} = d_{\text{offset}} \tan(\psi) \tag{2-33}$$

where d_{offset} is the offset distance and ψ is the angular change during motion. An example of Abbe error is shown in Figure 2-19. The measurement axis is offset by d_{offset} from the displacement axis and angular motion of the target generates Abbe error. To eliminate Abbe error, the axis of measurement must pass through the point of interest.

Cosine Error

Angular misalignment between the measurement axis (laser beam axis) and axis of motion results in an error. It is called cosine error because its magnitude is proportional to the cosine of the angle of misalignment [16]. Figure 2-20 illustrates cosine error with an angle γ between direction of motion and the beam axis. The measured displacement, l_{m}, is always less than the actual displacement, l. See Eq. 2-34. Cosine error can be minimized by aligning the laser beam parallel to the axis of motion as closely as possible.

$$\text{Cosine error } = l - l_m = l\left(1 - \cos(\gamma)\right) \tag{2-34}$$

Laser Wavelength Stability

The laser source of any interferometer system has some type of frequency stabilization to maintain its wavelength accuracy. As discussed previously, interferometer systems generate

fringes when displacement occurs. Each fringe is equivalent to a fraction of a wavelength of the laser. If the wavelength changes, the result is an apparent displacement. This apparent movement appears as a measurement error.

Electronics Error

In a heterodyne displacement measuring interferometer, the phase change between measurement and reference signals is measured. The optical measurement resolution, one fringe ($\lambda/2$ for the single pass configuration), can be electrically or optically extended. The electronics measurement resolution is based on how many points represent one complete period of phase. For example, if 2π radians of phase are subdivided by 1024 parts, the resolution can be extended up to $\lambda/2048 = \lambda/2(1024)$ for the single pass configuration. The electronics error can be taken to be equal to the electronics measurement resolution. However, amplifier nonlinearity may also to be considered [12].

Periodic Error

Imperfect separation of the two light frequencies into the moving and fixed paths has been shown to produce first and second order periodic error, or errors of one and two cycles per wavelength of optical path change, respectively. In other words, during the target motion, the measured displacement oscillates cyclically about the true displacement, typically with amplitude of several nanometers [1].

Sources of frequency leakage between paths include non-orthogonality between the linear beam polarizations, elliptical polarization of the individual beams, imperfect optical components/coatings, parasitic reflections from individual surfaces, and/or mechanical misalignment between the interferometer (laser, polarization dependent optics, and targets) [10]. Figure 2-21A shows a measured displacement (solid line) where periodic nonlinearity is

superimposed on the true value of displacement (dashed line). Figure 2-21B isolates periodic error by removing the least squares fit line from the constant velocity displacement data. Periodic error is described in more detail in Chapter 3.

An Example of Application

As noted, heterodyne displacement measuring interferometry has been widely used in applications that require high precision displacement. Those applications include position feedback for integrated circuit (I.C.) wafer steppers in the semiconductor fabrication industry, precision cutting machines, coordinate measuring machines, and calibration of transducers. In this section, the interferometer system applied for the position feedback of an I.C. wafer stepper stage, one of the most accuracy demanding application, is described using a commercially available interferometer system. The two major suppliers for a displacement measuring interferometer system are Agilent Technologies and Zygo. In this example, an Agilent 5527A laser system is described and measurement errors are provided [14].

Figure 2-22 shows the typical configuration for the I.C. wafer stage application. A two axis (X and Y), double pass heterodyne displacement measuring interferometer is used to measure the position of the wafer stage and provide position feedback to a controller. A wavelength tracker measures changes in the air's refractive index which is used to compensate atmospheric and deadpath errors (which occur due to environmental changes).

The interferometer system accuracy is determined using specifications provided in [14]. The list of parameters is summarized below.

- Maximum displacement measured (L): 0.2 m
- Environment:
    - Temperature: 20 °C ± 0.1 °C (temperature-controlled environment)
    - Pressure: 760 mmHg ± 25 mmHg (no pressure control)
    - Humidity: 50 % ± 10 % (humidity-controlled environment)

- Deadpath length: 0.1 m
- Abbe error: none (assume zero offset)
- Cosine error: 0.05 ppm (worst case)
- Laser wavelength stability:
    - Short-term (< an hour): ± 0.002 ppm
    - Long-term (> an hour): ± 0.02 ppm
- Electronics error (measurement resolution): ± 0.15 nm
- Periodic error: ± 2.2 nm

Note that the error components are divided into proportional and fixed terms. Proportional error terms are generally specified in parts-per-million (ppm) and these errors are a function of the target motion. Fixed error terms are noncumulative and do not depend on the target displacement. Units of fixed terms are given in length, such as meters and nanometers. Each error component is calculated individually and then the errors are combined to determine the system accuracy.

Atmospheric error depends on the air's refractive index variation due to changes temperature, pressure, humidity, and chemical composition. The wavelength tracker measures the air's refractive index variation and gives compensation information. The performance of the wavelength tracker is given in Eq. 2-35 for the compensation accuracy [14].

$$\text{Compensation accuracy} = \pm\,[0.067\ \text{ppm} + (0.06\ \text{ppm}/^{\circ}\text{C} \times \Delta T) + (0.002\ \text{ppm/mm Hg} \times \Delta P)] \tag{2-35}$$

In Eq. 2-35, ΔT is the temperature variation about 20 °C and ΔP is the pressure variation about 760 mm Hg. Using Eq. 2-35 and the environmental conditions, the compensation accuracy is ± 0.14 ppm. At the maximum displacement, the atmospheric error due to the wavelength tracker compensation is calculated as ± 28 nm (± $0.14 \times 10^{-6} \times 0.2$ m) using Eq. 2-31 where the compensated air's refractive index variation is used for Δn. The material thermal expansion error

is assumed to be zero and the optics thermal drift is given as ± 4 nm (40 nm/$^\circ$C × (±0.1°C)) for the plane mirror used in this application.

Geometric errors (deadpath, Abbe, and cosine error) are calculated next. The deadpath error is a function of deadpath length, method of compensation, and environmental conditions. Using the wavelength tracker compensation information and Eq. 2-32, the corrected deadpath error can be calculated as ± 14 nm ((± 0.14×10^{-6}) × 0.1 m). In the I.C. wafer stage application, it is usually possible to have the beam axis in line (collinear) with the axis of the stage motion. Therefore, the Abbe offset is zero and there exists no Abbe error. The cosine error is assumed to be 0.05 ppm which is -10 nm ((-0.05×10^{-6}) × 0.2 m) at the maximum displacement in the worst case. The negative sign indicates that the measured displacement is always smaller than true displacement due to cosine error.

Laser wavelength stability errors for short-term and long-term measurements are given as ± 0.4 nm (± 0.002×10^{-6} × 0.2 m) and ± 4 nm (± 0.02×10^{-6} × 0.2 m), respectively, at maximum displacement. For the wafer stepper application, the process time for the wafer exposures is typically short (< 2 min) [14]. Therefore, the short-term error is used in this example. The electronics error is the measurement resolution for the system (without considering the amplifier nonlinearity). The measurement resolution in the phase measuring electronics used in this application is 0.15 nm. Finally, periodic error is measured to be 2.2 nm.

Table 2-1 lists the error contributors associated with the I.C. wafer stepper application including and excluding atmospheric compensation. The error levels when the measurement occurs in a vacuum chamber are also included. Although measurement in a vacuum environment is costly, it is added to show how much the system accuracy can be improved and what errors still limit the system performance. In vacuum, the errors related to environmental changes are

eliminated and only cosine error and system errors remain. Moreover, if the measured displacement is small (i.e. nanometer or micrometer displacement which can be realized using piezo stage positioners), cosine error and laser wavelength stability error become negligible compared to electronics error (measurement resolution). For example, if the maximum displacement of a target is 100 μm, the cosine error (0.05 ppm) and the laser wavelength stability error (± 0.002 ppm) become - 0.005 nm and ± 0.0002 nm at the maximum displacement. However, periodic error is unchanged because it is a fixed error term. Therefore, periodic error limits to achieve the maximum system accuracy in this situation. This provides the motivation to eliminate periodic error in heterodyne displacement measuring interferometers.

Table 2-1. Heterodyne displacement measuring interferometer system accuracy for the integrated circuit wafer stage application.

Error	With atmospheric compensation	Without atmospheric compensation	In vacuum
	± (nm)	± (nm)	± (nm)
Atmospheric error	28	1800	0
Material thermal expansion error	0	0	0
Optics thermal drift error	4	4	0
Deadpath error	14	900	0
Abbe error	0	0	0
Cosine error	-10*	-10	-10**
Laser wavelength stability error	0.4	0.4	0.4**
Electronics error	0.15	0.15	0.15
Periodic error	2.2	2.2	2.2

* The measured displacement is always smaller than true displacement for this single-sided error.
** At the maximum displacement of 100 μm, cosine error (0.05 ppm) becomes - 0.005 nm and the laser wavelength stability error (± 0.002 ppm) becomes ± 0.0002 nm.

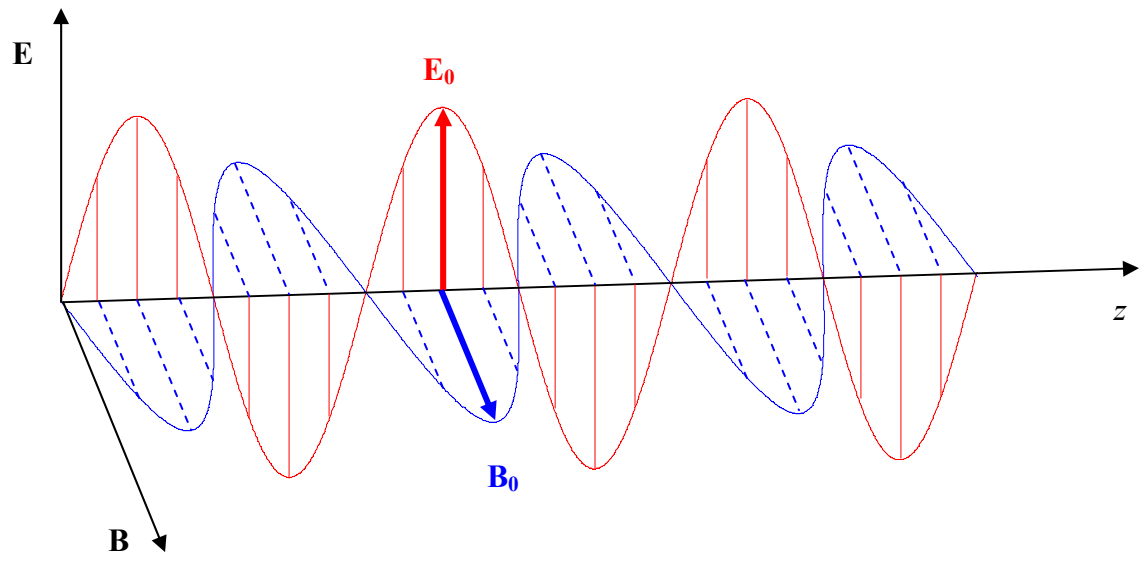

Figure 2-1. The electric (E) and magnetic (B) waves are orthogonal to each other and propagate in the same direction. A linearly polarized beam is shown.

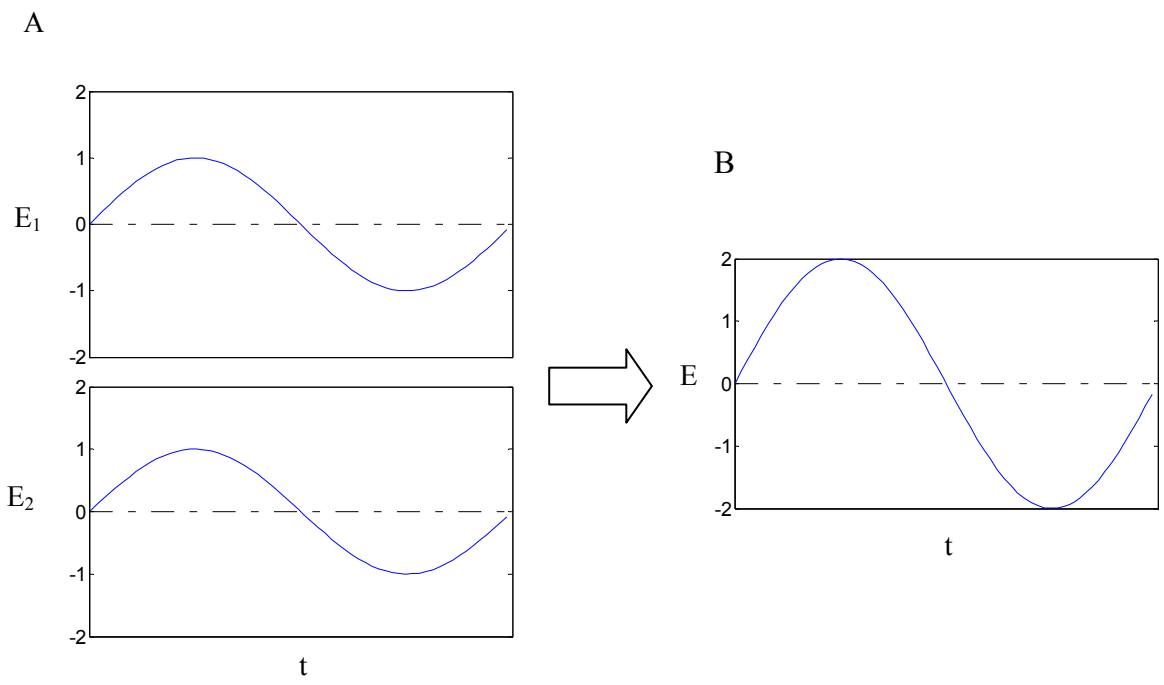

Figure 2-2. An example of constructive interference. A) Two waves with the same magnitude and phase (in phase). B) Constructive interference leads to a wave with double the magnitude.

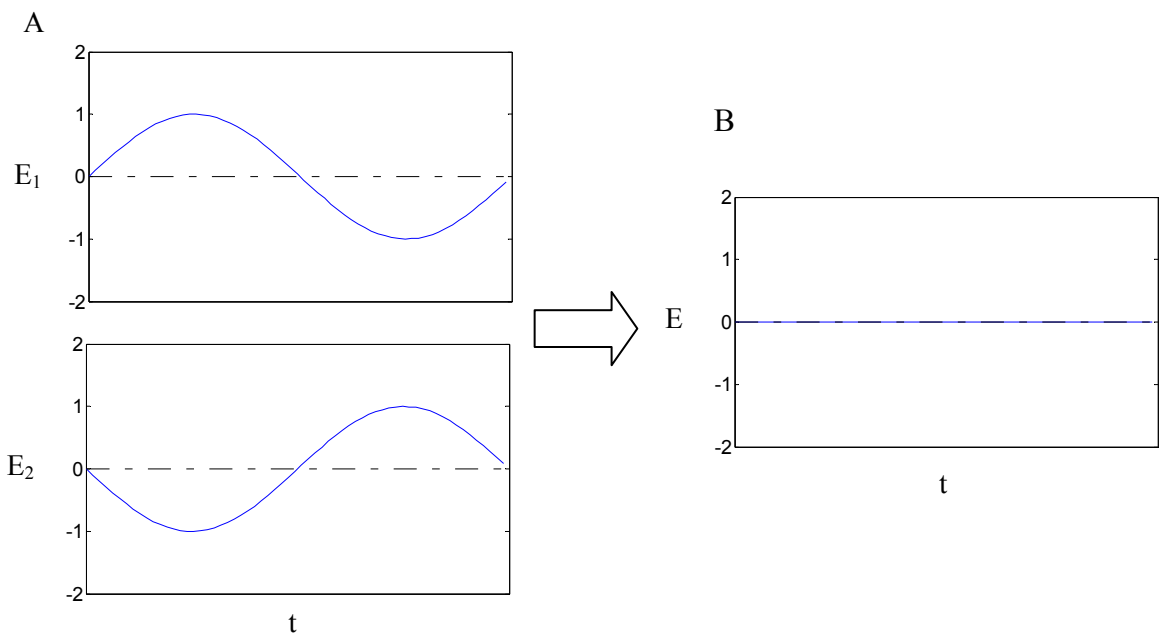

Figure 2-3. An example of destructive interference. A) Two waves with the same magnitude but 180 deg phase difference (out of phase). B) Destructive interference leads to a wave with zero magnitude.

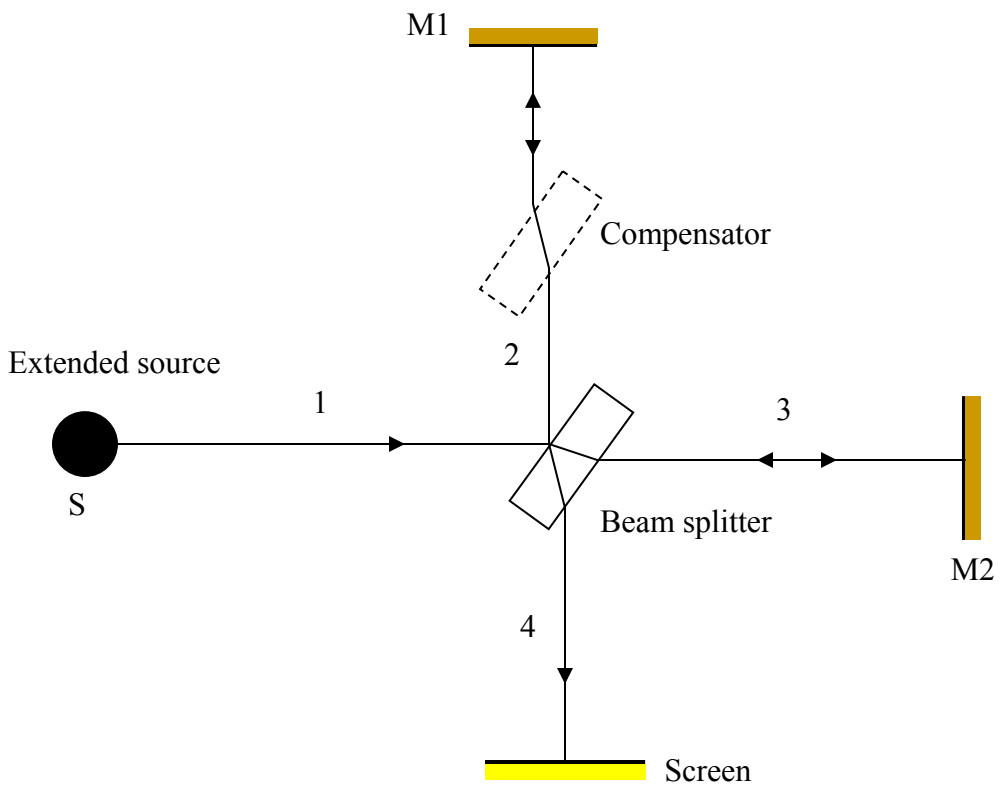

Figure 2-4. Schematic of the Michelson interferometer.

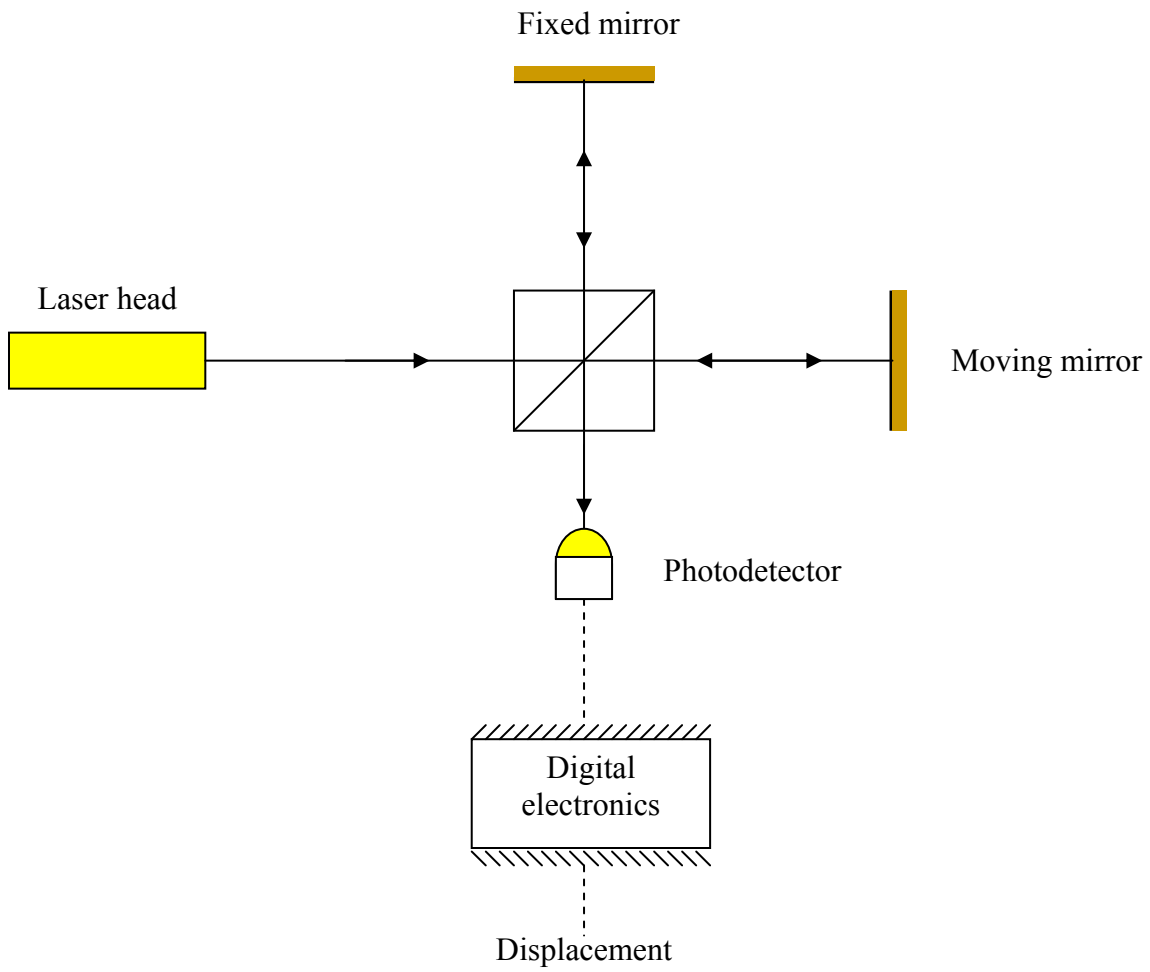

Figure 2-5. The Michelson interferometer with modern technology components.

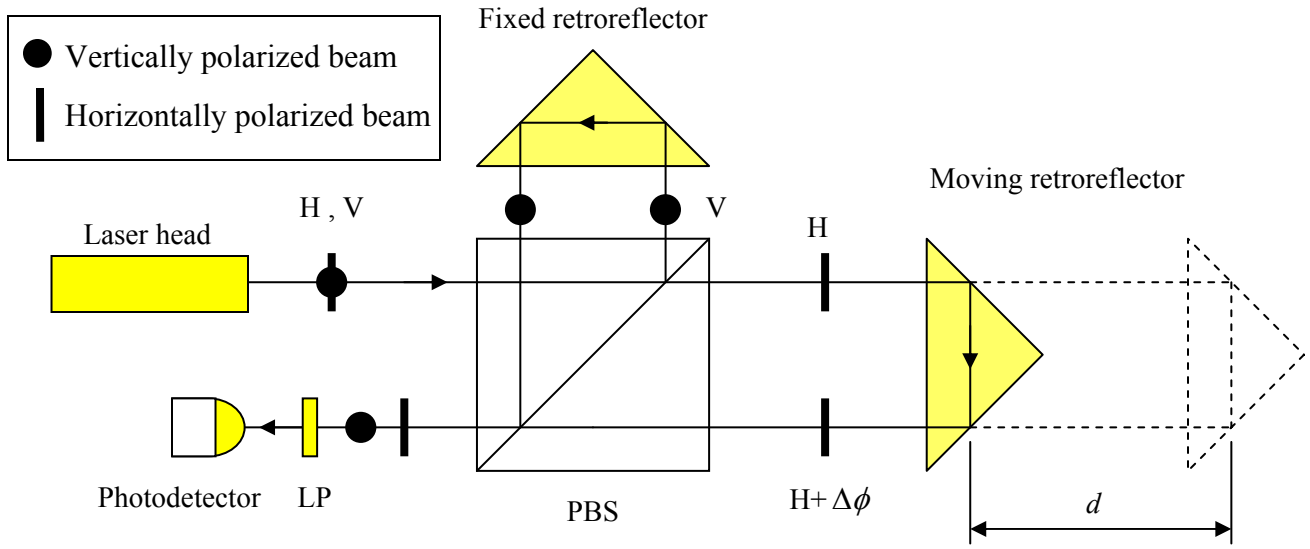

Figure 2-6. Schematic of a single pass interferometer.

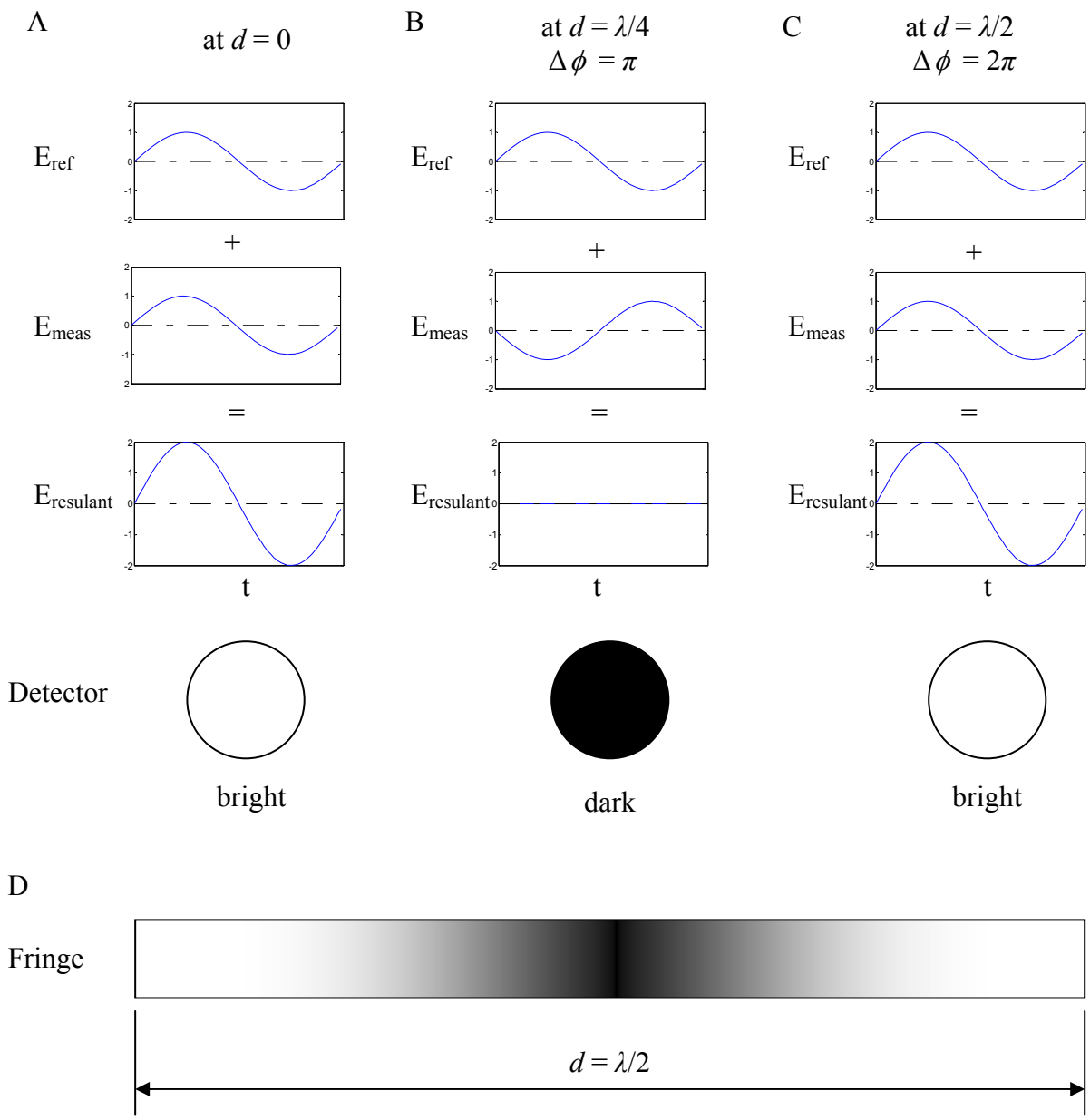

Figure 2-7. Interference according to the target displacement in a single pass configuration. A) Constructive interference at the no target motion ($d = 0$). Bright light is detected. B) Destructive interference at the target displacement of $d=\lambda/4$ where $\Delta\phi=\pi$. No light is detected C) Constructive interference at the target displacement of $d=\lambda/2$ where $\Delta\phi=2\pi$. Bright light is detected. D) A bright-dark-bright transition, one fringe or the optical resolution, corresponds to a half wavelength of the light source in the single pass configuration.

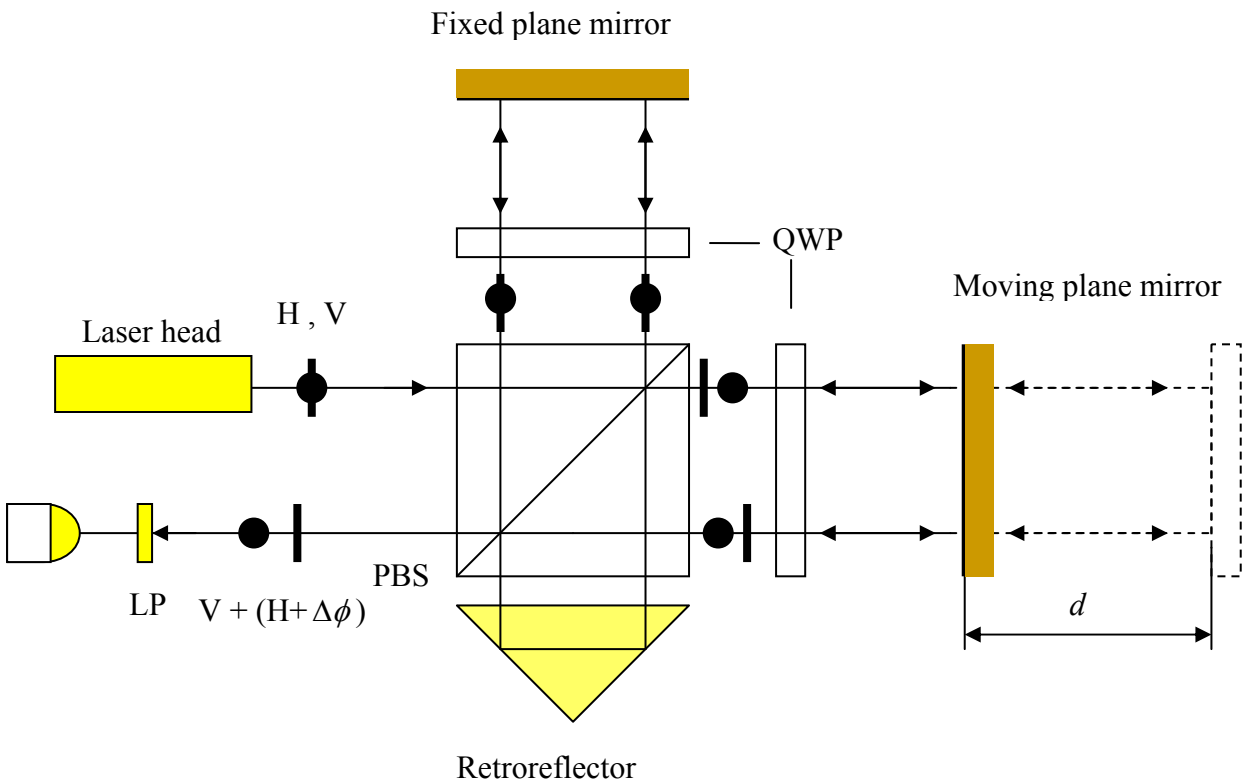

Figure 2-8. Schematic of a double pass interferometer.

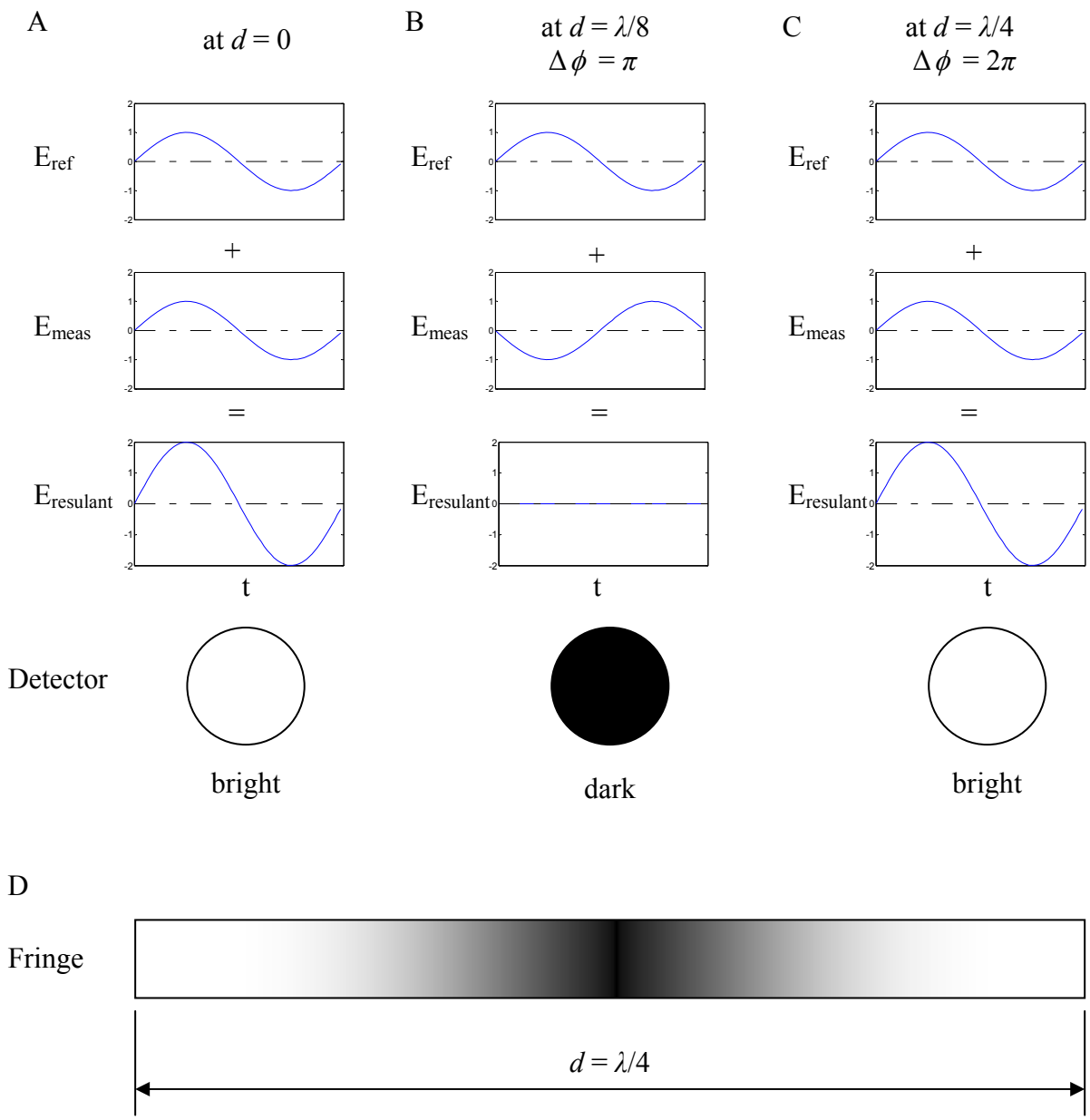

Figure 2-9. Interference according to the target displacement in a double pass configuration. A) Constructive interference at the no target motion ($d = 0$). Bright light is detected. B) Destructive interference at the target displacement of $d=\lambda/8$ where $\Delta\phi=\pi$. No light is detected. C) Constructive interference at the target displacement of $d=\lambda/4$ where $\Delta\phi=2\pi$. Bright light is detected. D) A bright-dark-bright transition, one fringe or the optical resolution, corresponds to a quarter wavelength of the light source in the double pass configuration.

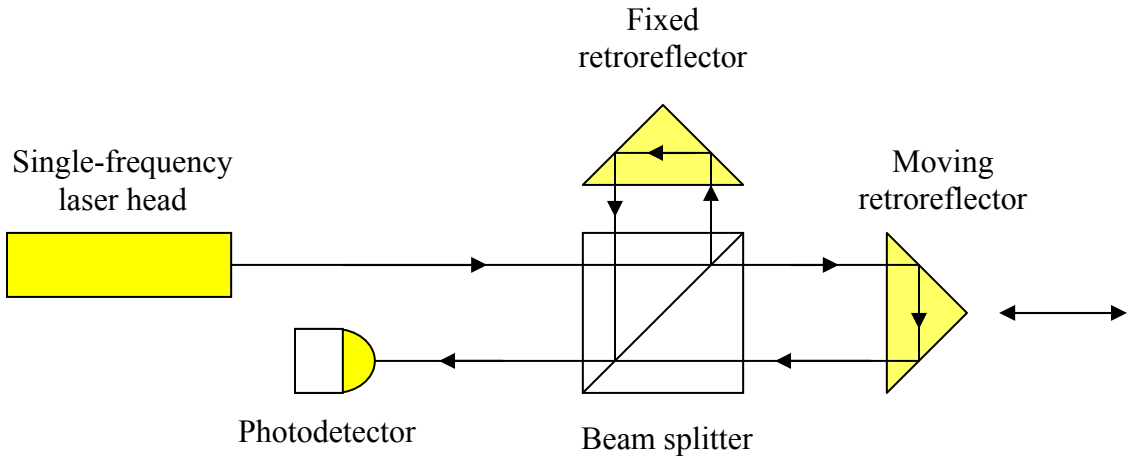

Figure 2-10. Schematic of a homodyne displacement measuring interferometer.

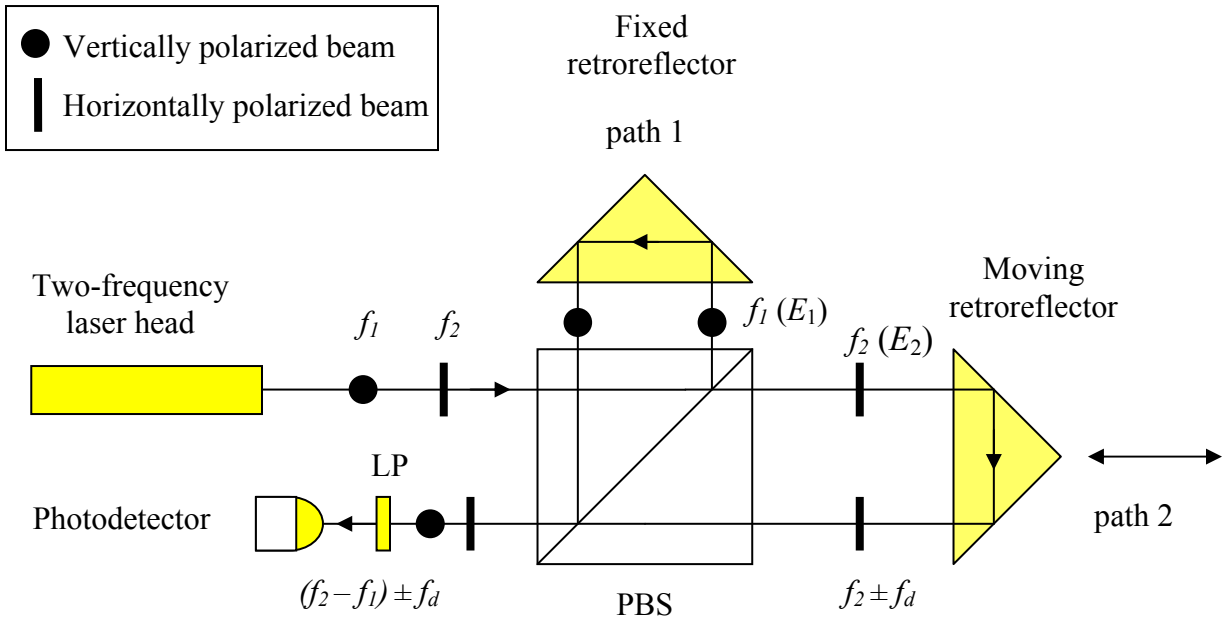

Figure 2-11. Schematic of a single pass heterodyne displacement measuring interferometer.

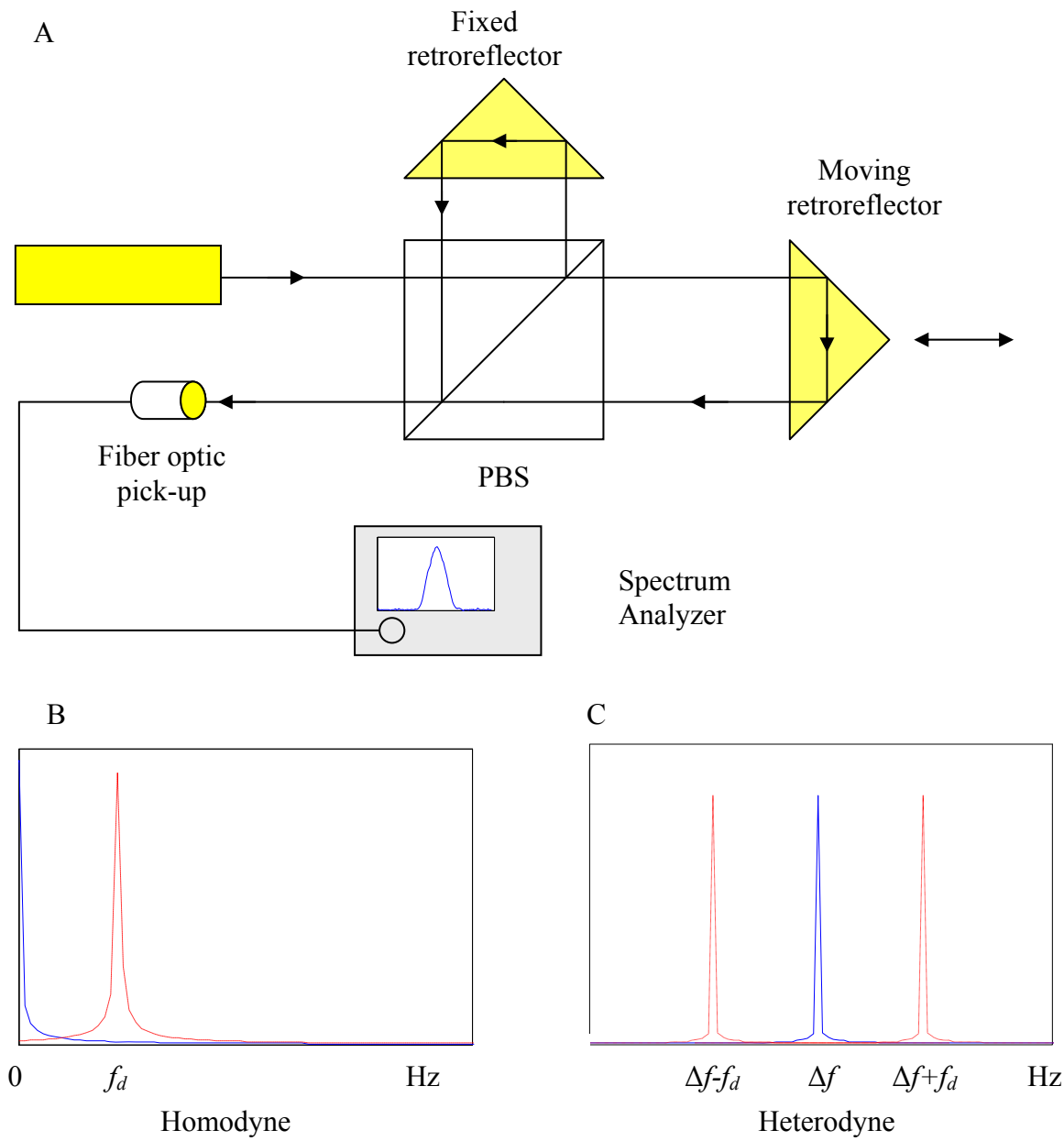

Figure 2-12. Spectrum analyzer outputs from two interferometers. A) A simple setup for homodyne and heterodyne systems showing the measurement signal output. B) Homodyne interferometer spectrum. C) Heterodyne interferometer spectrum.

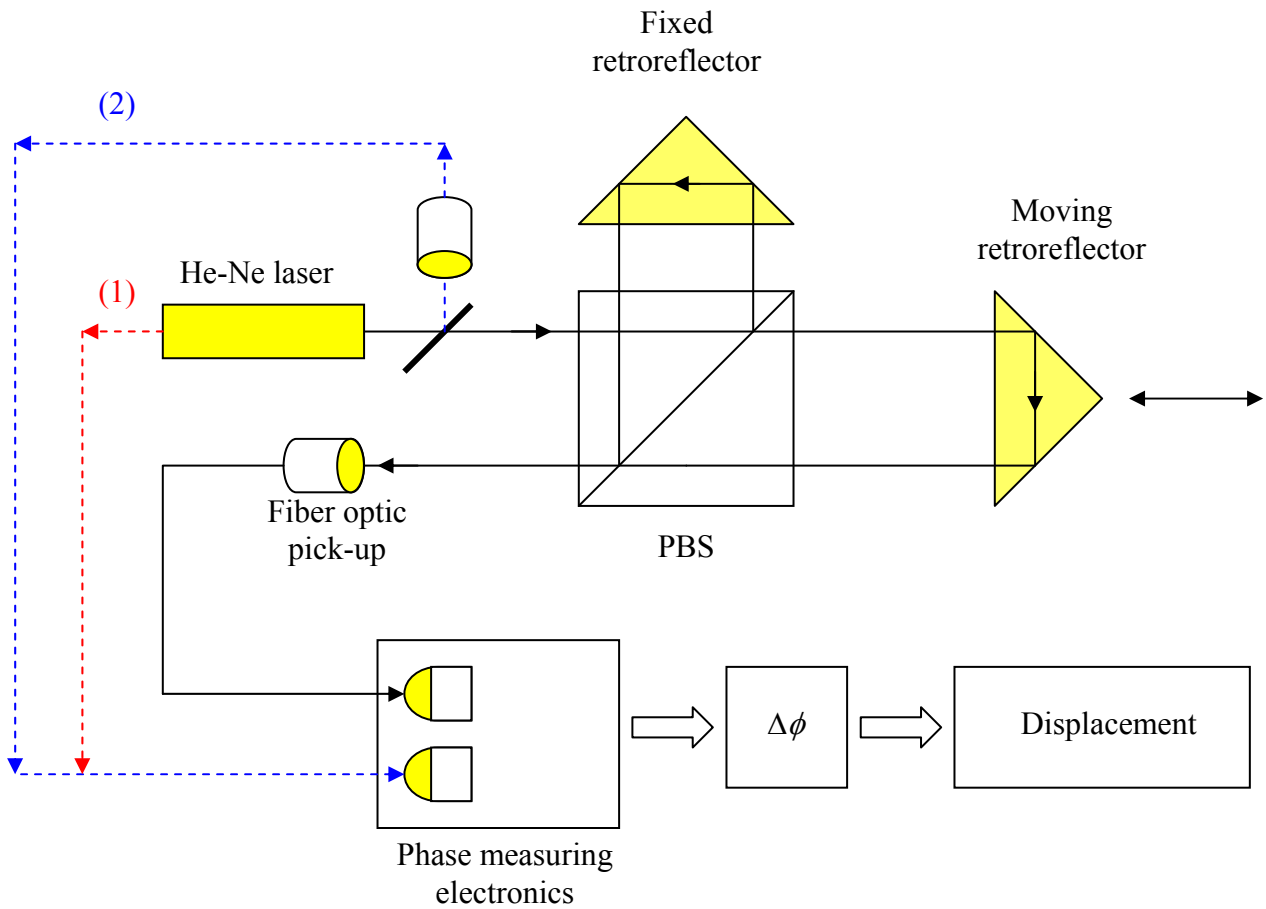

Figure 2-13. Schematic of heterodyne interferometer where displacement is determined by comparing the measurement and reference signals.

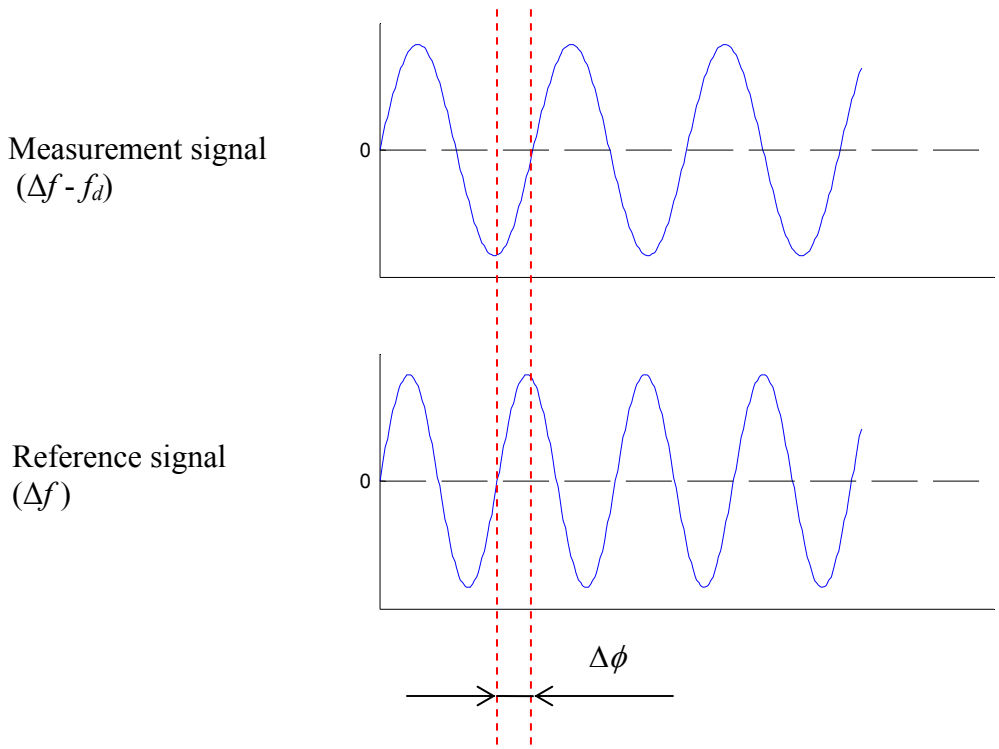

Figure 2-14. Phase difference between the measurement and reference signal.

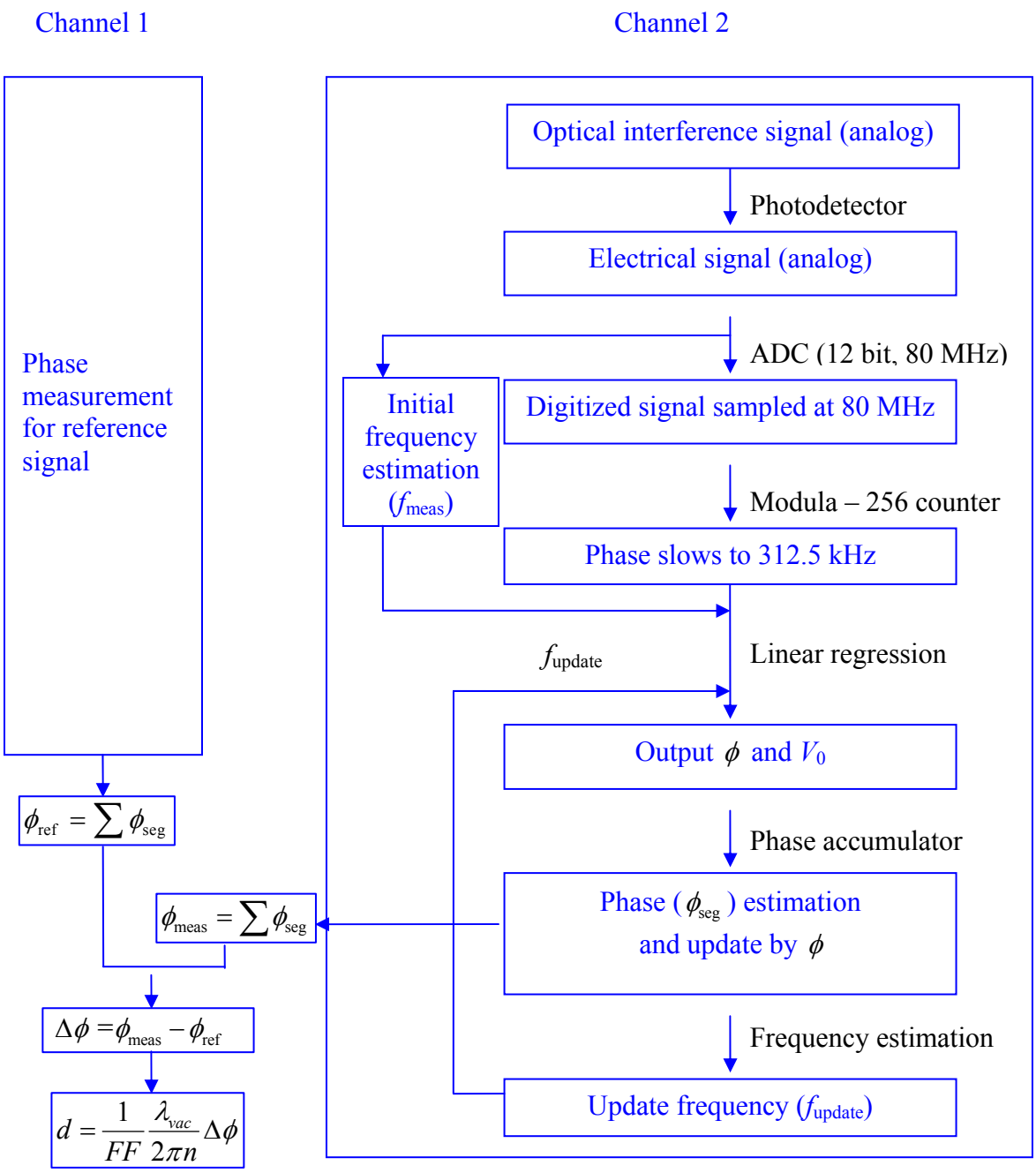

Figure 2-15. Flow chart for phase measurement.

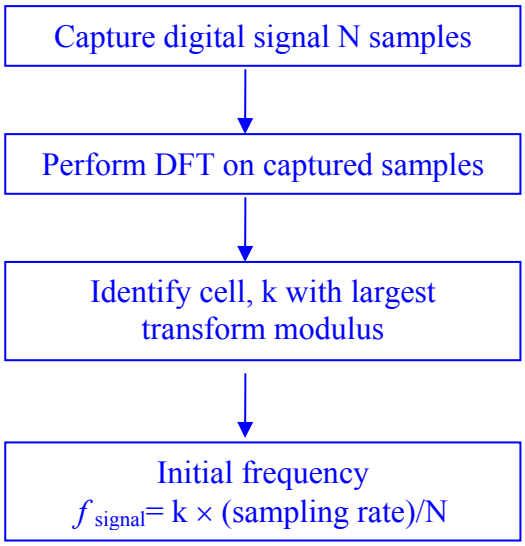

Figure 2-16. Flow chart for initial frequency estimation.

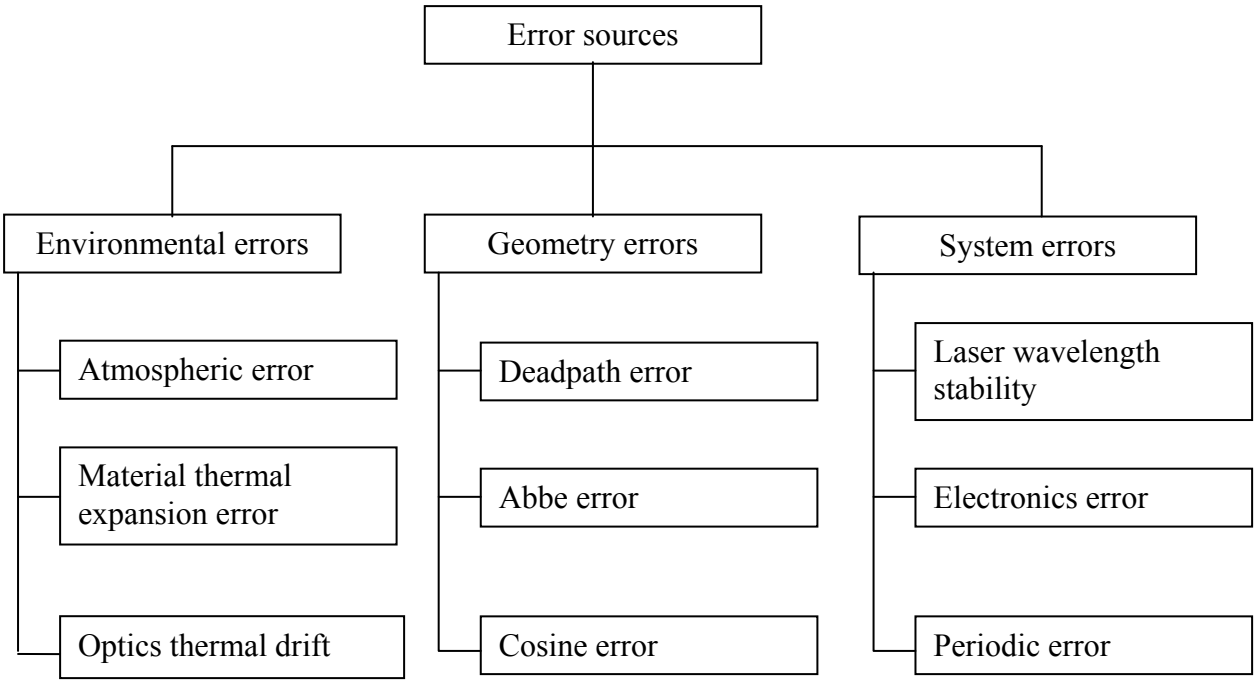

Figure 2-17. Error sources degrading the measurement accuracy in heterodyne interferometry.

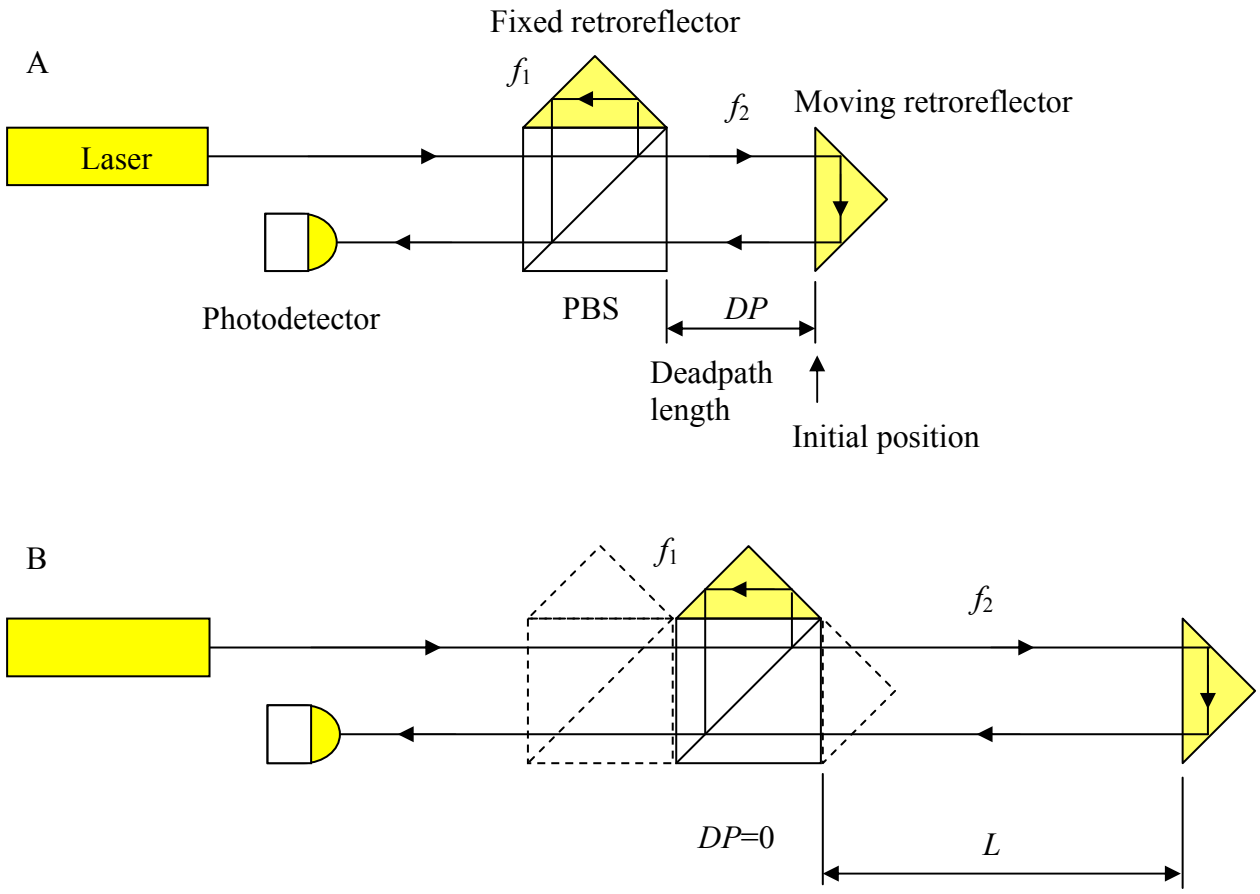

Figure 2-18. An example of deadpath error. A) Unequal path length between the fixed and moving arms gives the deadpath length. B) Deadpath error can be minimized by locating the interferometer at the initial position of the measurement.

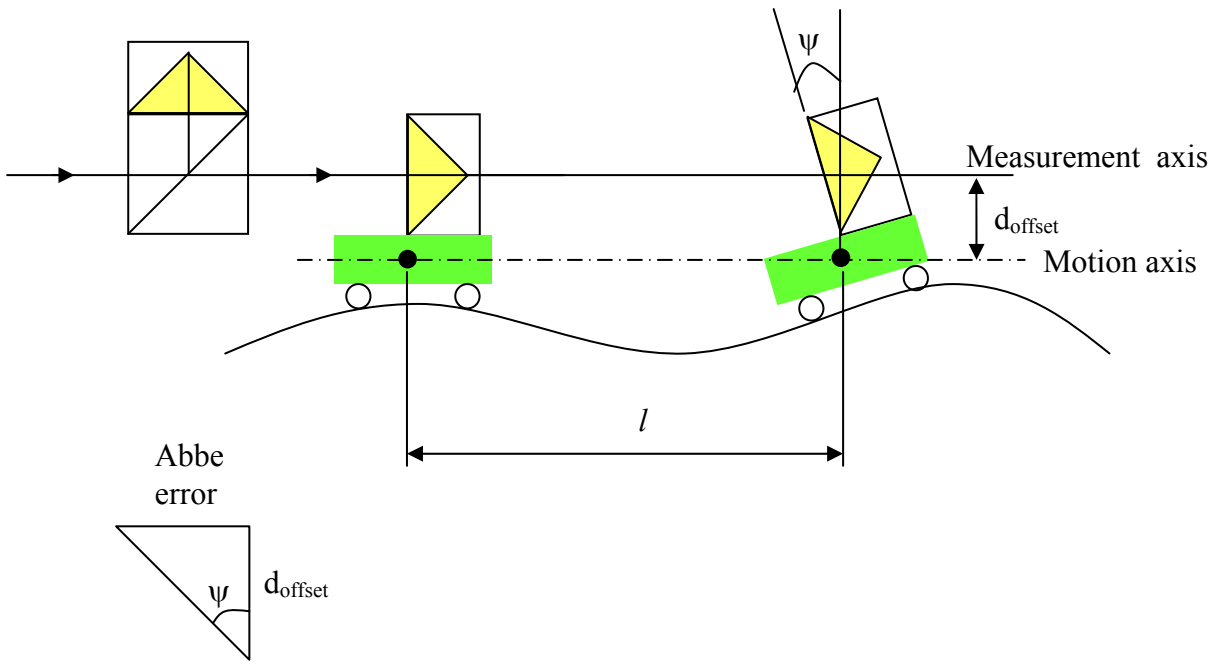

Figure 2-19. An example of Abbe error.

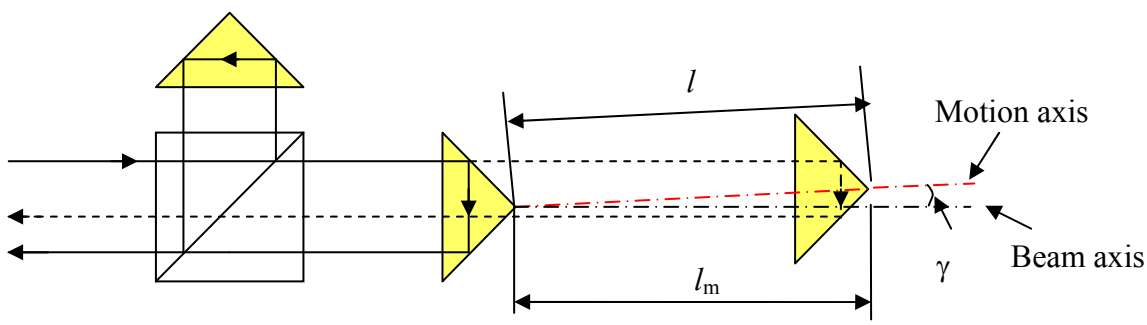

Figure 2-20. An example of cosine error.

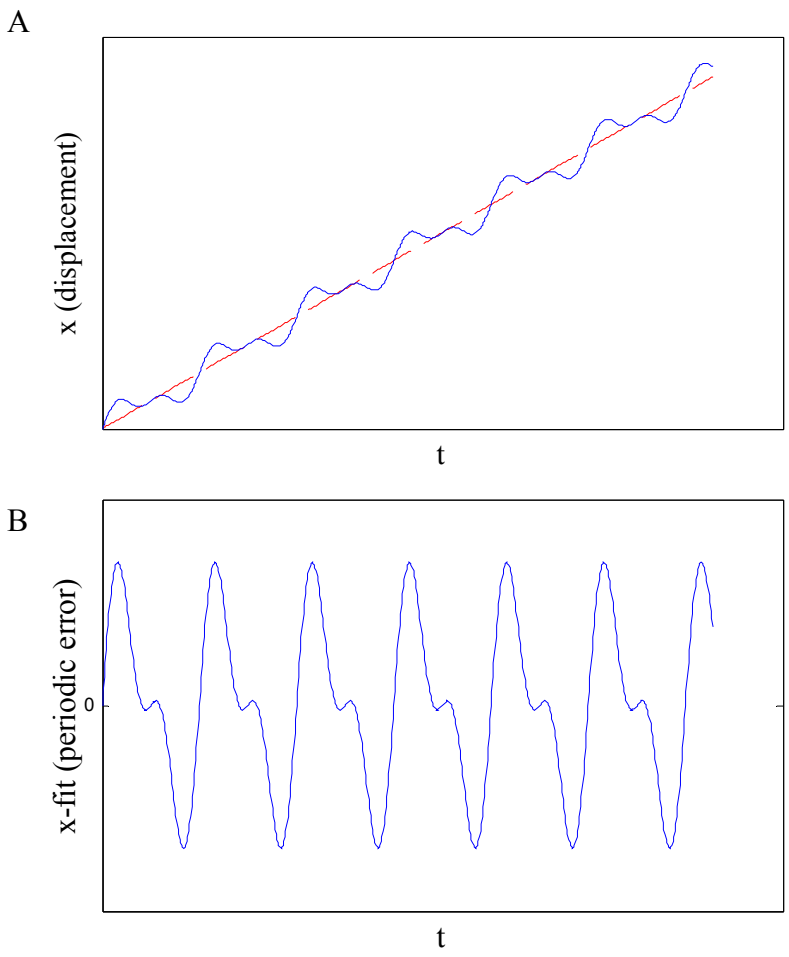

Figure 2-21. Visual description of periodic error. A) The constant velocity displacement, x, is not linear. B) First and second order periodic error is revealed after removing the least squares best fit line, fit.

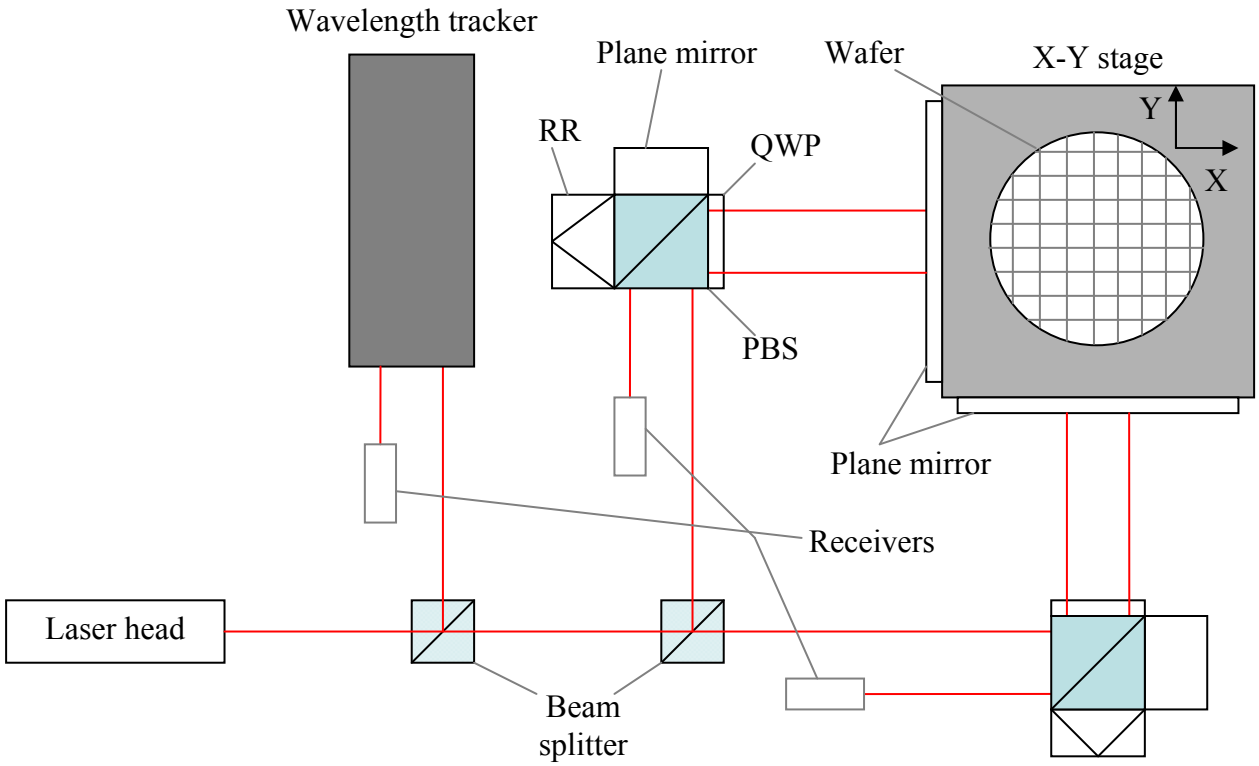

Figure 2-22. A heterodyne displacement measuring interferometer system configuration for position feedback in application of an integrated circuit wafer stepper. RR: retroreflector. QWP: quarter wave plate. PBS: polarizing beam splitter.

CHAPTER 3
PERIODIC ERROR REVIEW

One fundamental accuracy limitation for the commonly selected heterodyne (or two frequency) Michelson-type interferometer is periodic error. This non-cumulative error is inherent to the typical polarization coding approach, where the two (heterodyne) optical frequencies are carried on coincident/collinear, linearly polarized, mutually orthogonal laser beams and separated/recombined using polarization dependent optics. It is caused by frequency mixing/leakage between the fixed and moving paths and has been extensively explored in the literature.

Periodic Error Literature Review

Many studies of periodic error have been reported. Eighty-one journal publications with direct relevance to periodic error in displacement measuring interferometry are identified here[1]. They are subdivided into the following eight categories (see Table 3-1): 1) early work [18-21] – these papers describe early investigations of the existence of periodic error; 2) discussion of error sources [11, 16, 17, 22-25] – publications that provide descriptions of common error sources in displacement measuring interferometry; 3) index of refraction [15, 26-31] – papers that show the calculation/measurement of the refractive index of air, which is critical for measurements not completed in vacuum or another gaseous environment, such as helium due to its reduced index sensitivity to environmental conditions; 4) periodic error description and modeling [5, 12, 32-48] – these articles are focused on describing and modeling the physical sources of periodic error for various interferometer configurations; 5) error measurement methods [2, 49-55] – papers that

---

Reprinted with permission from Kim H, Schmitz T, Beckwith J. Periodic error in heterodyne interferometry: Examination and Elimination. In: Halsey D, Raynor W, ed. Handbook of Interferometers: Research, Technology and Applications. Hauppauge, NY: Nova Science; 2009.

[1] One conference proceedings [58] was included because it is the first reference that describes frequency domain evaluation of periodic error, which is applied in this research.

detail the measurement of periodic error and related parameters; 6) periodic error compensation and correction [9-10, 56-82] – texts that describe variations in optical/electrical configurations and/or data processing algorithms that yield reduced periodic error levels; 7) uncertainty evaluation [83-84] – descriptions of uncertainty analyses for heterodyne interferometry; and 8) measurement applications [85-89] – examples of displacement measuring interferometry applied in practice with consideration of periodic error.

Table 3-1. Summary of periodic error literature review.

Topic	References
Early work	18-21
Discussion of error sources	11, 16, 17, 22-25
Index of refraction	15, 26-31
Periodic error description and modeling	5, 12, 32-48
Error measurement methods	2, 49-55
Periodic error compensation and correction	9, 10, 56-82
Uncertainty evaluation	83-84
Measurement applications	85-89

Frequency-Path Model

As briefly described in Chapter 2, in heterodyne Michelson-type interferometers that rely on polarization coding, imperfect separation of the two light frequencies into the moving and fixed paths has been shown to produce first and second order periodic errors. Unwanted frequency leakage may occur due to a number of influences, including non-orthogonality between the ideally linear beam polarizations, elliptical polarization of the individual beams, imperfect optical components, parasitic reflections from individual optical surfaces, and/or mechanical misalignment between the interferometer elements (laser, polarizing optics, and targets). In a perfect system, a single frequency travels to a fixed target, while a second, single frequency travels to a moving target. Interference of the combined signals yields a perfectly sinusoidal trace with phase that varies, relative to a reference phase signal, in response to motion of the moving target. However, the inherent frequency leakage in actual implementations

produces an interference signal which is not purely sinusoidal (i.e., contains unintended spectral content) and leads to periodic error in the measured displacement. The ideal case is depicted in Figure 3-1A, where f_1 and f_2 represent the two frequencies and f_d indicates the Doppler frequency shift due to motion of the moving target (the right retroreflector in the schematics). Note that $f_d = FF\left(nv/\lambda_{vac}\right)$, Eq. 2-22, where FF is the fold factor (equal to 2 for the single pass heterodyne system in Figure 3-1), λ_{vac} is the vacuum wavelength, and v is the measurement target velocity. In Figure 3-1B, the frequency leakage is indicated by the dashed lines (leakage) superimposed on the solid (intended) paths. Schmitz and Beckwith [12] presented the Frequency-Path model that predicts the number of interference terms that may be expected at the photodetector output. The F-P model for a single pass heterodyne interferometer is described in the following paragraphs for both the ideal (no frequency leakage) and non-ideal (frequency leakage) cases.

In the ideal case, there are two source frequencies, f_1 and f_2, and only one possible path for each frequency from the source to the detector. This yields two F–P elements; one F–P element represents the propagation of the first frequency along its intended path to the fixed target, while the other F–P element represents the propagation of the second frequency along its intended path to the moving target. In the model notation, the electric field amplitude of each element is designated by the letter E appended with two subscripts, E_{ij}. The first subscript denotes the source frequency, while the second gives the path from the source to detector. For example, E_{11}, displayed as a line in Figure 3-2A, gives the electric field amplitude of frequency 1 that reaches the detector via path 1. For the ideal representation shown in Figure 3-2A, the two F–P elements give a total of $(m)(m + 1)/2 = (2)(2 + 1)/2 = 3$ interference terms: two *optical power* terms (due to the squaring action of the photodetector), which occur at zero frequency (*dc*), and the desired

ac interference term, which appears at the beat frequency ($\Delta f = f_2 - f_1$) with no motion and is Doppler shifted up or down in frequency during motion of the moving target (depending on the direction).

In the non-ideal case displayed in Figure 3-2B, there are two source frequencies and two possible paths for each frequency from the source to detector (assuming multiple extraneous reflections are neglected) due to imperfect frequency separation at the polarizing beam splitter. In other words, both frequencies can travel to either the fixed or moving target in a fully leaking system. This gives four F-P elements and (4)(4+1)/2 = 10 distinct interference terms.

The following paragraphs describe the origins of the 10 interference terms in a fully leaking interferometer. The fixed path, which ideally contains light of only frequency f_1 (expressed in Hz), propagates two signals due to frequency leakage,

$$E_{11}\cos\left(\omega_1 t - k_1\left(FF\right)x_1 + \phi_{11}\right) \tag{3-1}$$
$$E_{21}\cos\left(\omega_2 t - k_2\left(FF\right)x_1 + \phi_{21}\right)$$

where ϕ_{ij} are the initial phases of the signals E_{ij}, x_1 represents motion of the reference target, k_1 and k_2 are the propagation constants equal to $2\pi/\lambda_1$ and $2\pi/\lambda_2$, respectively, and $\omega_{1,2} = 2\pi f_{1,2}$ (rad/s). The two wavelengths λ_1 and λ_2 correspond to the two heterodyne frequencies. Recall that in the E_{ij} notation, the first subscript denotes frequency, while the second indicates the path (1 for fixed and 2 for moving) [12]. Similarly, the moving path ideally composed of only f_2 light, also contains two signals,

$$E_{22}\cos\left(\omega_2 t - k_2\left(FF\right)x_2 + \phi_{22}\right) \tag{3-2}$$
$$E_{12}\cos\left(\omega_1 t - k_1\left(FF\right)x_2 + \phi_{12}\right)$$

where the parameter definitions are analogous. The photodetector current is obtained by squaring the sum of the four E_{ij} terms (the two intended signals have equal subscripts while the two leakage induced signals have unequal subscripts). See Eq. 3-3.

$$
\begin{aligned}
I \propto E^2 = & \Big(E_{11}\cos\left(\omega_1 t - k_1(FF)x_1 + \phi_{11}\right) + E_{21}\cos\left(\omega_2 t - k_2(FF)x_1 + \phi_{21}\right) \\
& + E_{22}\cos\left(\omega_2 t - k_2(FF)x_2 + \phi_{22}\right) + E_{12}\cos\left(\omega_1 t - k_1(FF)x_2 + \phi_{12}\right)\Big)^2 \\
= & \frac{E_{11}^2}{2}\left[\cos\left(2\omega_1 t - 2k_1(FF)x_1 + 2\phi_{11}\right) + 1\right] \\
& + \frac{E_{21}^2}{2}\left[\cos\left(2\omega_2 t - 2k_2(FF)x_1 + 2\phi_{21}\right) + 1\right] \\
& + \frac{E_{22}^2}{2}\left[\cos\left(2\omega_2 t - 2k_2(FF)x_2 + 2\phi_{22}\right) + 1\right] \\
& + \frac{E_{12}^2}{2}\left[\cos\left(2\omega_1 t - 2k_1(FF)x_2 + 2\phi_{12}\right) + 1\right] \\
& + E_{22}E_{11}\begin{bmatrix} \cos\left(\omega_2 t + \omega_1 t - k_2(FF)x_2 - k_1(FF)x_1 + \phi_{22} + \phi_{11}\right) \\ + \cos\left(\Delta\omega t - k_2(FF)x_2 + k_1(FF)x_1 + \phi_{22} - \phi_{11}\right) \end{bmatrix} \\
& + E_{21}E_{12}\begin{bmatrix} \cos\left(\omega_2 t + \omega_1 t - k_1(FF)x_2 - k_2(FF)x_1 + \phi_{21} + \phi_{12}\right) \\ + \cos\left(\Delta\omega t + k_1(FF)x_2 - k_2(FF)x_1 + \phi_{21} - \phi_{12}\right) \end{bmatrix} \\
& + E_{22}E_{12}\begin{bmatrix} \cos\left(\omega_2 t + \omega_1 t - k_2(FF)x_2 - k_1(FF)x_2 + \phi_{22} + \phi_{12}\right) \\ + \cos\left(\Delta\omega t - k_2(FF)x_2 + k_1(FF)x_2 + \phi_{22} - \phi_{12}\right) \end{bmatrix} \\
& + E_{21}E_{11}\begin{bmatrix} \cos\left(\omega_2 t + \omega_1 t - k_2(FF)x_1 - k_1(FF)x_1 + \phi_{21} + \phi_{11}\right) \\ + \cos\left(\Delta\omega t - k_2(FF)x_1 + k_1(FF)x_1 + \phi_{21} - \phi_{11}\right) \end{bmatrix} \\
& + E_{11}E_{12}\begin{bmatrix} \cos\left(2\omega_1 t - k_1(FF)x_2 - k_1(FF)x_1 + \phi_{11} + \phi_{12}\right) \\ + \cos\left(k_1(FF)x_2 - k_1(FF)x_1 + \phi_{11} - \phi_{12}\right) \end{bmatrix} \\
& + E_{21}E_{22}\begin{bmatrix} \cos\left(2\omega_2 t - k_2(FF)x_2 - k_2(FF)x_1 + \phi_{21} + \phi_{22}\right) \\ + \cos\left(k_2(FF)x_2 - k_2(FF)x_1 + \phi_{21} - \phi_{22}\right) \end{bmatrix}
\end{aligned}
\tag{3-3}
$$

Several simplifications may be applied to Eq. 3-3. First, x_1 is ideally zero because there is no motion of the fixed target. Second, for a relatively small split frequency between the two heterodyne signals, $\Delta\omega = \omega_2 - \omega_1$ (on the order of MHz for commercial systems), the

propagation constants, k_1 and k_2, are nearly equal and a single value, k, may be substituted for each. Third, due to detector bandwidth limitations, terms that oscillate at twice the optical frequency (i.e., $2\omega_1 t$, $2\omega_2 t$, or $\omega_1 t + \omega_2 t$) may be neglected. See Eq. 3-4.

$$
\begin{aligned}
I \propto E^2 = & \left(\frac{E_{11}^2}{2} + \frac{E_{21}^2}{2} + \frac{E_{22}^2}{2} + \frac{E_{12}^2}{2} \right) && \textit{optical power} \\
& + E_{22} E_{11} \cos\left(\Delta\omega t - k\left(FF\right) x_2 + \phi_{22} - \phi_{11} \right) && \textit{ac interference (intended)} \\
& + E_{21} E_{12} \cos\left(\Delta\omega t + k\left(FF\right) x_2 + \phi_{21} - \phi_{12} \right) && \textit{ac interference (leakage induced)} \\
& + E_{22} E_{12} \cos\left(\Delta\omega t + \phi_{22} - \phi_{12} \right) && \textit{ac reference (due to measurement path)} \\
& + E_{21} E_{11} \cos\left(\Delta\omega t + \phi_{21} - \phi_{11} \right) && \textit{ac reference (due to reference path)} \\
& + E_{11} E_{12} \cos\left(k\left(FF\right) x_2 + \phi_{11} - \phi_{12} \right) && \textit{dc interference (frequency 1)} \\
& + E_{21} E_{22} \cos\left(k\left(FF\right) x_2 + \phi_{21} - \phi_{22} \right) && \textit{dc interference (frequency 2)}
\end{aligned}
\tag{3-4}
$$

Equation 3-4 lists all 10 interference terms in a fully leaking two frequency interferometer. These 10 terms are summarized in Table 3-2. The intended *ac interference* term is defined by the interference of E_{22} and E_{11}. It represents the signal of choice in heterodyne systems. Under constant velocity target motion, this term appears at a frequency[2] of $\Delta f - f_d$ in the spectrum analyzer display. A second *ac interference* term is obtained due to interference between the leakage terms E_{21} and E_{12}. This term represents second order periodic error and includes a Doppler phase shift, $k(FF)x_2$, of equal value but opposite sign relative to the intended *ac interference* term. Therefore, at constant velocity this term is seen at a frequency of $\Delta f + f_d$. The *ac reference* terms represent first order periodic error and occur due to interference between the intended and leakage terms of different frequencies that exist in either the fixed or moving paths. They appear at the split frequency Δf.

[2] The intended *ac interference* signal may also be up-shifted depending on the target motion direction. In this case, the leakage induced *ac interference* will be downshifted.

Two *dc interference* terms also exist because f_1 and f_2 appear in both the moving and fixed paths. For a single frequency, or homodyne system, the corresponding *dc interference* term is the selected measurement signal (e.g., $E_{11}E_{12}$ for frequency f_1). These terms exhibit a positive Doppler phase shift of equal value to the *ac interference* terms regardless of target motion direction and exist at zero frequency when the measurement target is at rest. Finally, the *optical power* terms contribute a zero frequency offset to the photodetector current regardless of optical path changes.

Due to their frequency dependence, a spectrum analyzer provides a powerful tool for visualizing the contributions of the various terms [2, 55]. Figures 3-3 through 3-6 depict each interference term and their appearance in a spectrum analyzer display. A representation of a typical frequency spectrum for the fully leaking interferometer is provided in Figure 3-7.

Table 3-2. Interference terms in fully leaking single pass heterodyne interferometer.

Type	Active F-P elements
optical power	$E_{11}E_{11}$
optical power	$E_{21}E_{21}$
optical power	$E_{22}E_{22}$
optical power	$E_{12}E_{12}$
ac interference (intended)	$E_{22}E_{11}$
ac interference (leakage induced)	$E_{21}E_{12}$
ac reference (path 2)	$E_{22}E_{12}$
ac reference (path 1)	$E_{21}E_{11}$
dc interference (frequency 1)	$E_{11}E_{12}$
dc interference (frequency 2)	$E_{21}E_{22}$

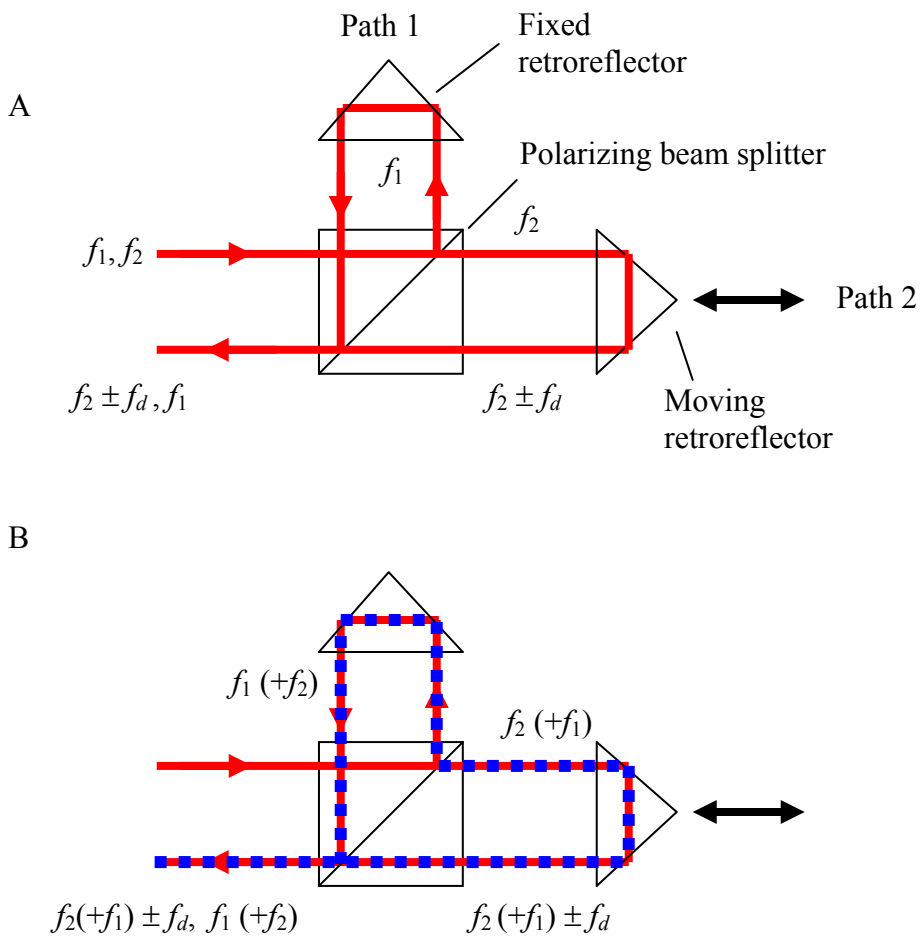

Figure 3-1. Schematics for ideal and fully frequency leaking interferometer. A) Ideal heterodyne interferometer behavior. B) The leakage terms are shown in parentheses. The two frequencies, f_1 and f_2, are ideally linearly polarized and orthogonal. This enables the polarizing beam splitter to separate them based on their polarization states.

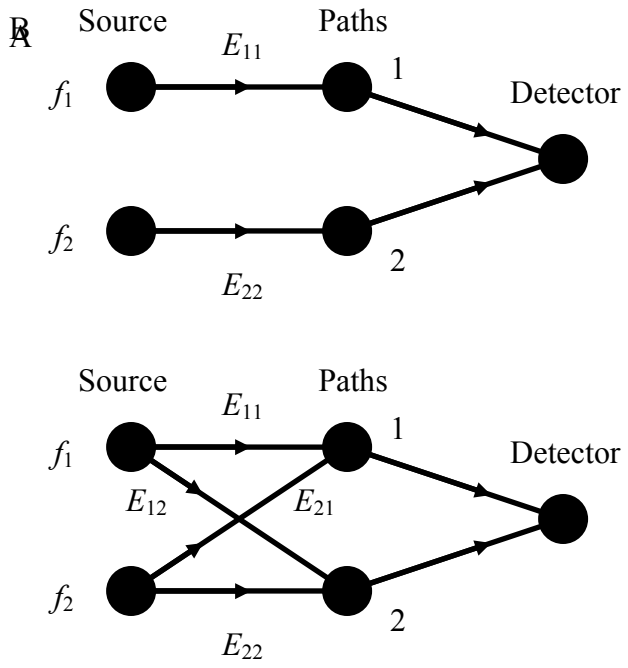

Figure 3-2. Frequency-path models. A) For ideal behavior. B) For fully leaking case.

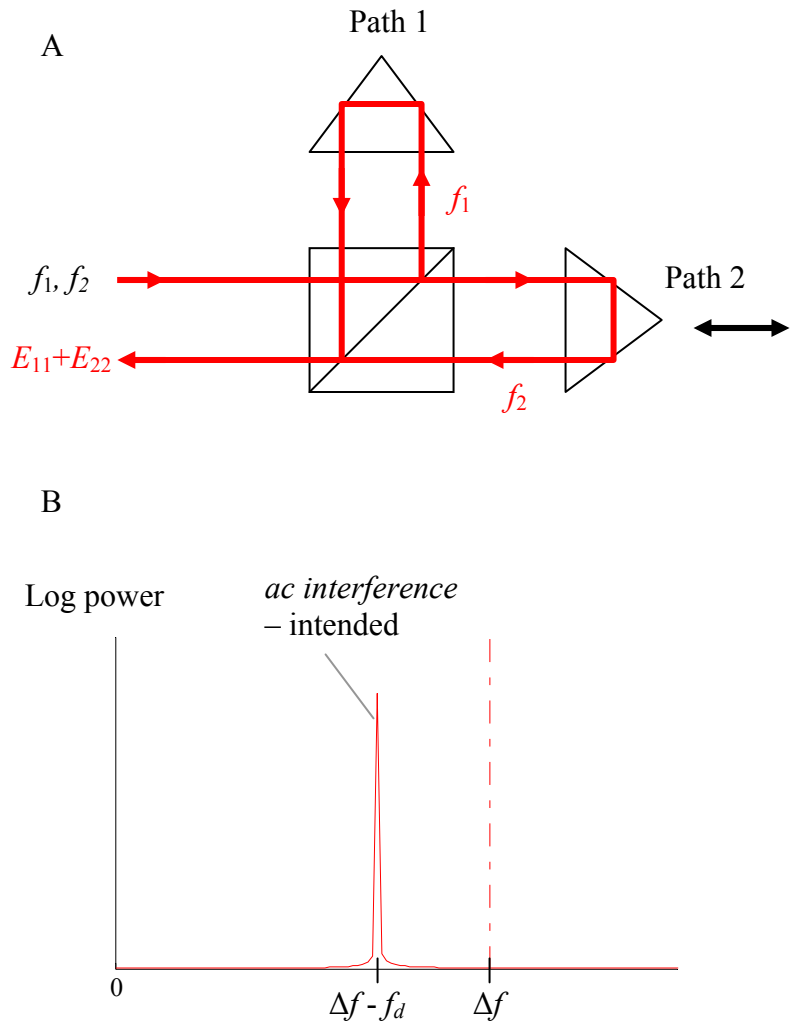

Figure 3-3. Intended *ac interference* signal. A) Interference between ideally separated beams (no frequency leakage). B) Power spectrum for the *ac interference* term.

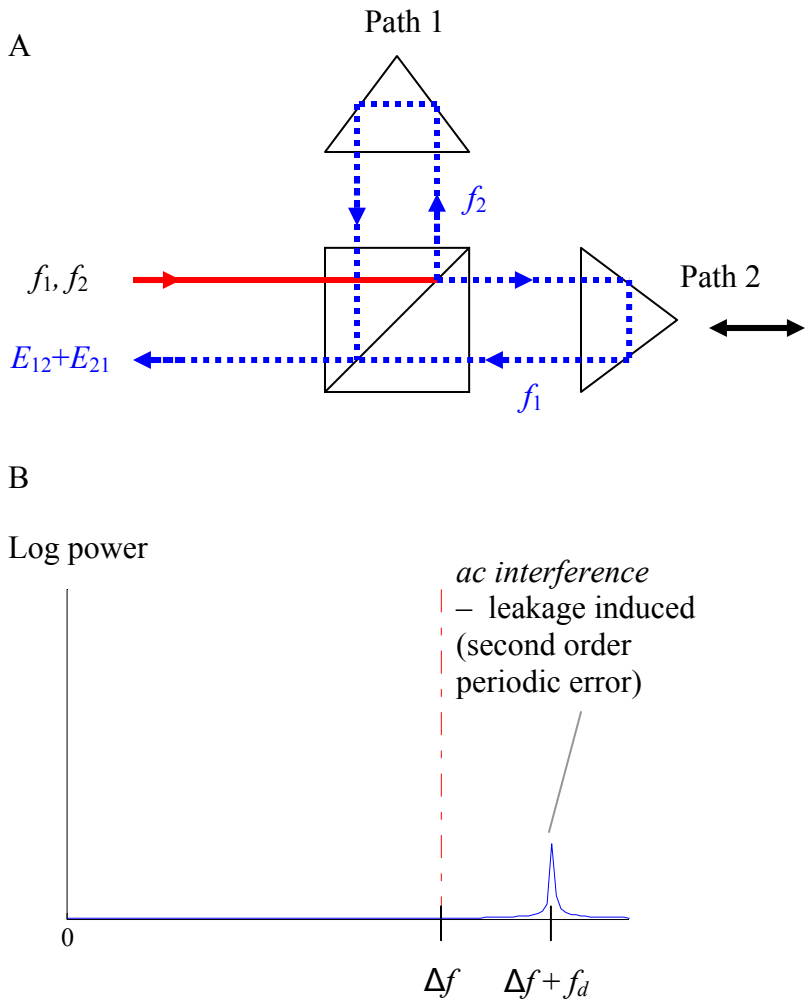

Figure 3-4. Leakage induced *ac interference*. A) Interference between leaking frequencies. B) Power spectrum for the leakage induced *ac interference* term.

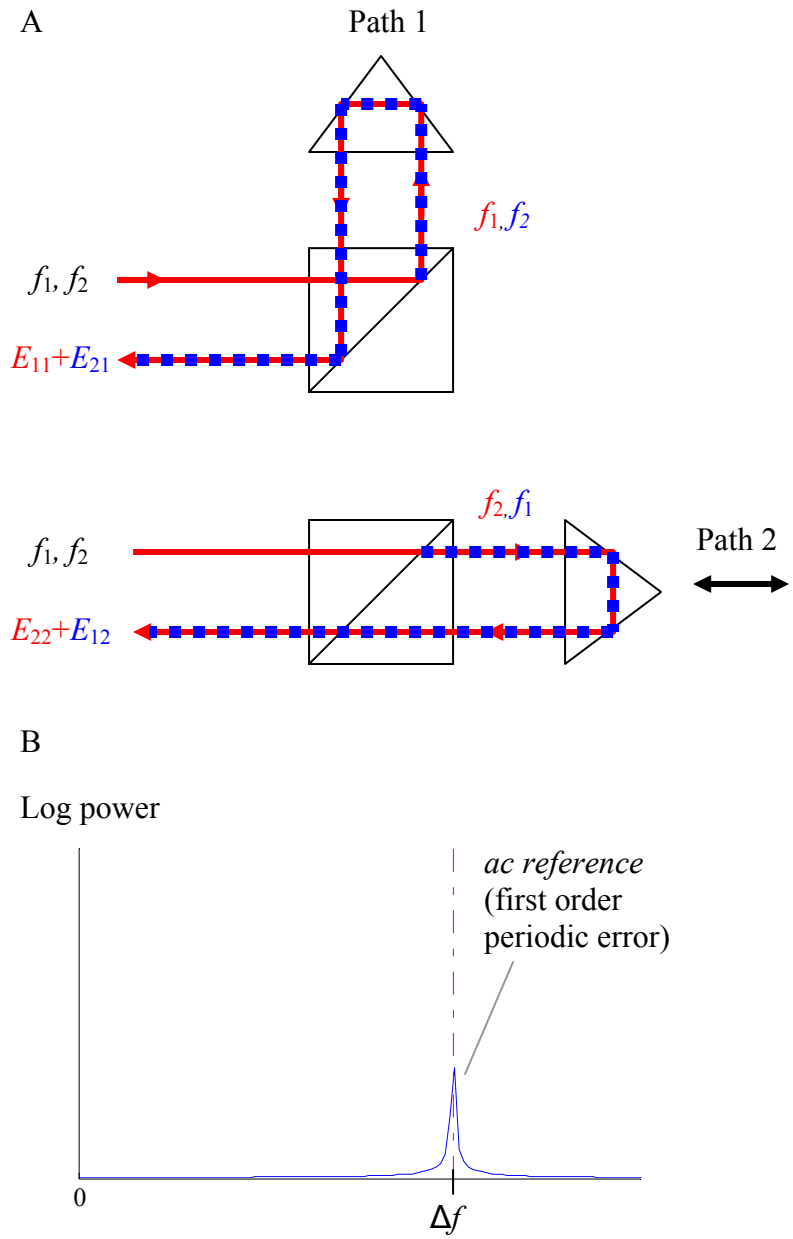

Figure 3-5. Description of *ac reference* terms. A) Interference between intended and leaking frequencies on the same path. B) Power spectrum for *ac reference* terms.

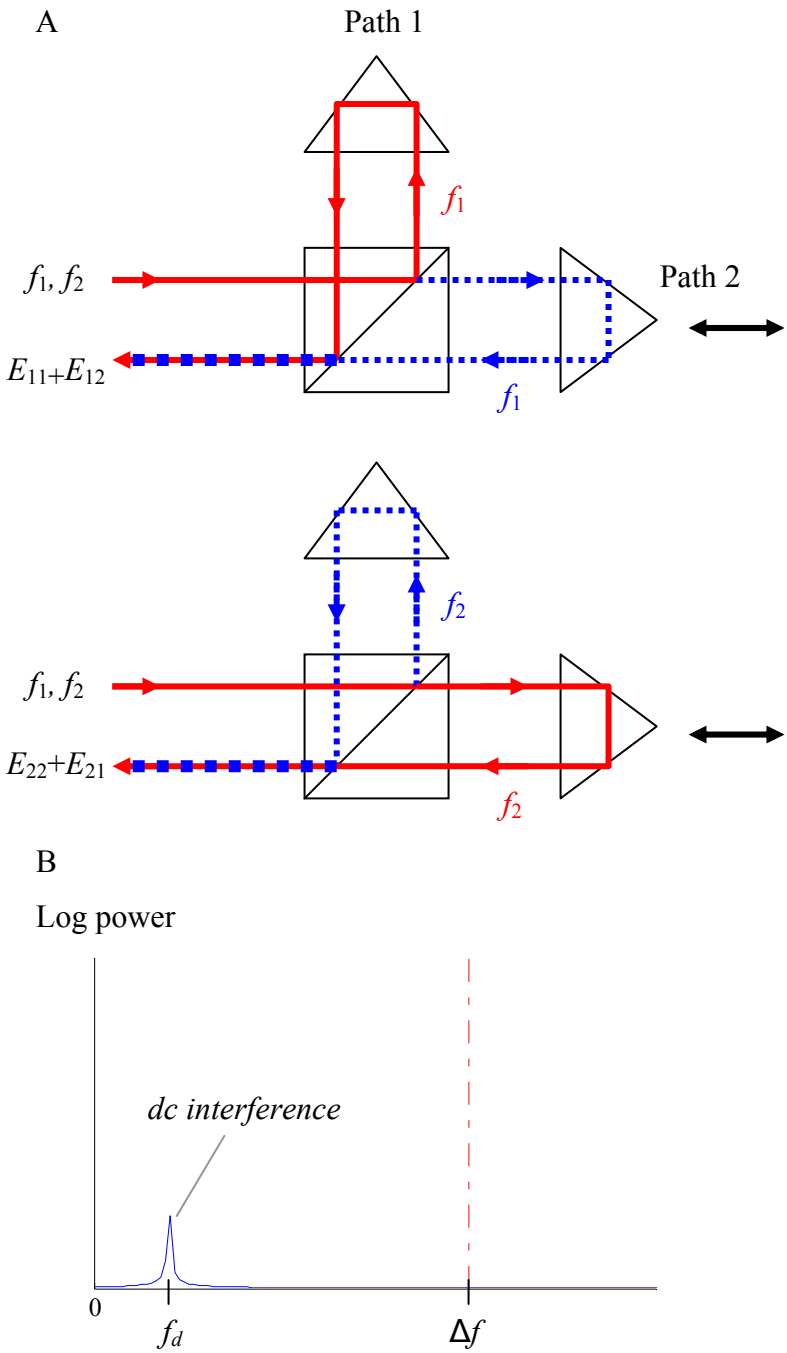

Figure 3-6. Description of *dc interference* terms. A) Interference between the same frequency in both paths. B) Power spectrum for the *dc interference* terms.

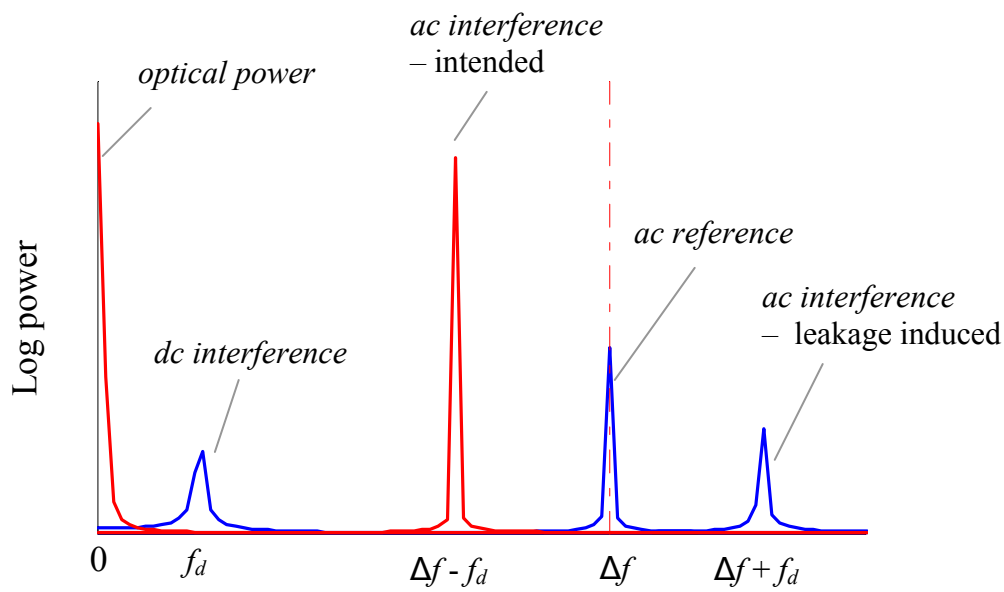

Figure 3-7. Power spectrum for constant velocity motion in fully leaking heterodyne interferometer.

CHAPTER 4
POLARIZATION CODED INTERFEROMETER

As described in the previous chapter, a polarization coded heterodyne interferometer system is a common choice for measuring displacement. In this chapter, a setup for a traditional single pass heterodyne interferometer and periodic error measurement results are presented. The setup is specifically designed to isolate periodic error by minimizing the other error sources described in Chapter 2. It can also vary the magnitude of periodic error by using a phase retarder (half wave plate) which rotates the orientation of linear polarized light. Test results from both phase measurement (for displacement calculation) and spectrum analyzer data are provided. Time domain periodic error is obtained using the measured displacement. It is then converted into the frequency domain (using the Fourier transform) to identify the first and second error orders. Periodic error magnitudes from the spectrum analyzer, the displacement data, and a model developed by Cosijns *et al*. [5] are compared for various setup conditions.

Setup Description

A photograph and schematic of a traditional heterodyne displacement measuring interferometer setup are provided in Figure 4-1. The orthogonal, linearly polarized beams with a frequency difference of approximately 3.65 MHz (Helium-Neon laser source with a Zeeman split) first pass through a half wave plate. Rotation of the half wave plate enables variation in the apparent angular alignment (about the beam axis) between the polarization axes and polarizing beam splitter; deviations in this alignment lead to frequency mixing in the interferometer. The light is then incident on a non-polarizing beam splitter (80% transmission) that directs a portion of the beam to a fiber optic pickup after passing through a fixed angle sheet polarizer (oriented at

---

Reprinted with permission from Kim H, Schmitz T, Beckwith J. Periodic error in heterodyne interferometry: Examination and Elimination. In: Halsey D, Raynor W, ed. Handbook of Interferometers: Research, Technology and Applications. Hauppauge, NY: Nova Science; 2009.

45 deg to the nominal laser orthogonal polarizations). The pickup is mounted on a two rotational degree-of-freedom flexure which enables efficient coupling of the light into the multi-mode fiber optic. This signal is used as the phase reference in the measurement electronics.

The remainder of the light continues to the polarizing beam splitter where it is (ideally) separated into its two frequency components that travel separately to the moving and fixed retroreflectors. Motion of the moving retroreflector is achieved using an air bearing stage. After the beams are recombined in the polarizing beam splitter, they are directed by a 90 deg prism through a polarizer (or analyzer) with a variable rotation angle. Finally, the light is launched into a fiber optic pickup. This serves as the measurement signal in the measurement electronics (0.3 nm resolution for the single pass configuration).

The intent of this setup was to minimize other well-known error contributors and set various first and second order periodic error magnitudes. To isolate periodic error, the setup was constructed with zero dead path difference (i.e., the distance between the polarization beam splitter and the moving retroreflector was equal to the distance between the polarization beam splitter and the fixed retroreflector at initialization) and small Abbe offset (25 mm). The measurement time (~100 ms) and motion excursions were kept small to minimize the contribution of air refractive index variations due to the environmental changes. Additionally, careful alignment of the air bearing stage axis with the optical axis resulted in small beam shear.

Traditional Setup Experimental Results

In this section, results obtained from the traditional polarization coded design are presented. These results, which exhibit various periodic error levels, were collected using both a spectrum analyzer and typical phase measuring electronics. The experimental data is also compared to predictions from the model developed by Cosijns *et al*. [5].

Displacement Data

First and second order periodic error magnitudes can be extracted from the displacement data obtained from the interference signal. Displacement was determined using standard phase measuring electronics (312.5 kHz sampling frequency) during constant velocity motion of the moving target retroreflector. Figure 4-2A shows the displacement data for a misaligned system (5 deg difference from the nominal orientation for both the half wave plate and linear polarizer). In Figure 4-2B the least squares best fit line is removed to reveal the periodic error. To identify the first and second order error magnitudes, the discrete Fourier transform of the error was computed and the spatial frequency axis was normalized to the periodic error order; see Figure 4-2C. For the selected misalignments, both first and second order periodic error is present. Figure 4-3 shows the displacement obtained for nominal angular alignment of both the linear polarizer and half wave plate. The second order error dominates in the well aligned system, which agrees with the spectrum analyzer data shown later in Figure 4-6.

Spectrum Analyzer Data

Figure 4-4 shows a schematic diagram of an analog spectrum analyzer setup to collect measurement signals from the interferometer. The measurement signal was carried via the multi-mode optical fiber to a battery operated photodetector (to minimize noise), which converted the optical signal to an electrical signal. The electrical signal was carried to the spectrum analyzer (Model: HP1850A) by a (shielded) BNC cable and the corresponding spectrum was recorded. The spectrum analyzer consists of three modules: 1) display section to control the signal display, 2) RF section to control frequency, and 3) IF section to control magnitude. Figure 4-5 shows the frequency content from the fully leaking interferometer pictured in Figure 4-1. The spectrum in Figure 4-5 was measured with a 5 deg misalignment of the half wave plate and 10 deg misalignment of the linear polarizer from their nominal orientations. The velocity, v, of the

moving target retroreflector was 5,000 mm/min. The constant velocity motion of the target produces a Doppler frequency shift which is proportional to the velocity, $f_d = \frac{2nv}{\lambda_{vac}}$, for the single pass setup where $n \approx 1$ is the air refractive index and λ_{vac} = 633 nm is the laser source vacuum wavelength. In this case, the Doppler frequency is positive when the stage moves in the $+x$ direction (as identified Figure 4-1A) and its magnitude is 0.26 MHz. The intended *ac interference* signal is up-shifted by the Doppler frequency, $\Delta f + f_d$. The *ac reference* (first order periodic error) and leakage induced *ac interference* (second order periodic error) signals appear at the beat frequency, Δf = 3.65 MHz, and the beat frequency downshifted by the Doppler frequency, $\Delta f - f_d$, respectively.

Figure 4-6 demonstrates the spectral content for a well aligned system. In this case, the second order periodic error dominates, which agrees with the result in [2]. The Doppler frequency shift is now 0.53 MHz (v = 10,000 mm/min). Figure 4-7 shows that the periodic error magnitudes are independent of target velocity. Measurements were performed at {5,000, 10,000, and 15,000} mm/min. The interferometer configuration was not changed: the misalignments were 10 deg (from nominal) for both the half wave plate and linear polarizer. Although the peak magnitudes are constant, the Doppler frequency shift changes with velocity, as expected.

Comparison between Measurements and Model

Several tests were completed to compare the periodic error magnitudes obtained from the spectrum analyzer and phase measuring electronics (position data) for various frequency mixing levels. Periodic error calculation from the spectrum analyzer is described in Chapter 5. Data were collected for variation of the half wave plate orientation of ± 10 deg from nominal (fast axis vertical in Figure 4-1) and linear polarizer variation of ± 17 deg from the nominal angle (45 deg

from vertical). Note that a 10 deg rotation of the half wave plate yields a 20 deg rotation of the polarization vector. The results are also compared with the mean periodic error values from a Monte Carlo evaluation [84] of the Cosijns *et al*. model [5]. The parameters used to calculate the periodic error in this model is described in detail in Chapter 6 when analyzing the uncertainty of periodic error.

Figures 4-8 through 4-10 show the error magnitudes of first and second order periodic error resulting from multiple measurements. The variables α and θ are the orientation of the linear polarization vectors with respect to the polarizing beam splitter axes and the angular deviation of the linear polarizer transmission axis from 45 deg, respectively. They can be varied by rotating the half wave plate (α variation) and linear polarizer (θ variation). The discrete Fourier transform magnitudes of periodic error for the position data (phase measuring electronics) is shown in Figure 4-8, the spectrum analyzer data is provided in Figure 4-9, and the mean values from the Monte Carlo evaluation of the model for each combination is plotted in Figure 4-10. Good agreement is seen for both periodic error orders in all cases.

The preceding analyses were completed to: 1) demonstrate the spectral content of displacement measuring interferometer position data that includes periodic error; and 2) show that spectrum analyzer evaluation of periodic error is comparable to both discrete Fourier transform calculations of error magnitudes from position data and an established model. The spectrum analyzer evaluation approach is used in the experimental validation of the new acousto-optic modulator-based displacement measuring interferometer (AOM DMI) design. The configuration and test results for the AOM DMI are presented in Chapter 7.

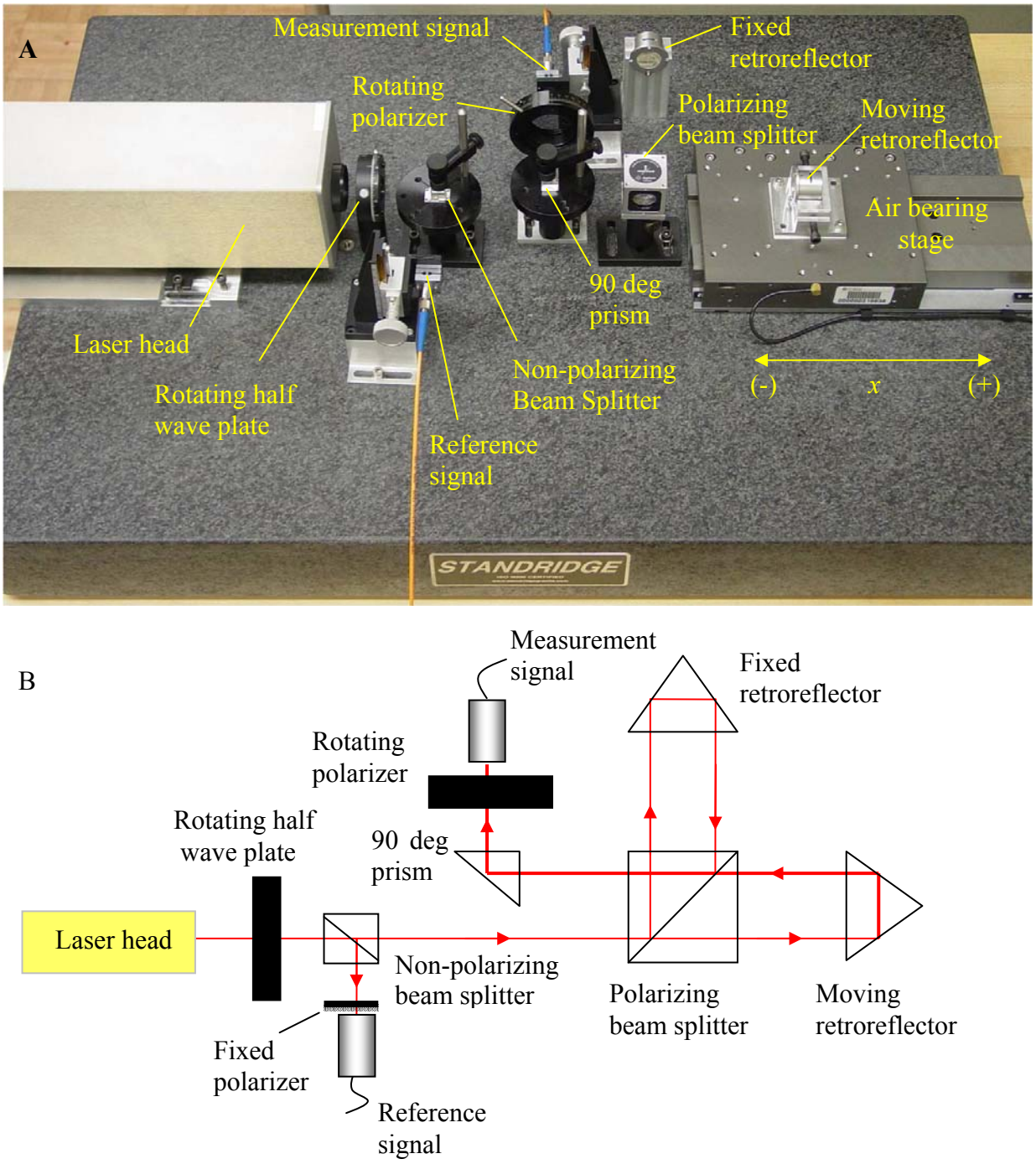

Figure 4-1. Setup for a single pass heterodyne interferometer. A) Photograph of single pass heterodyne interferometer experimental setup. B) Schematic of setup where the beam paths are shown.

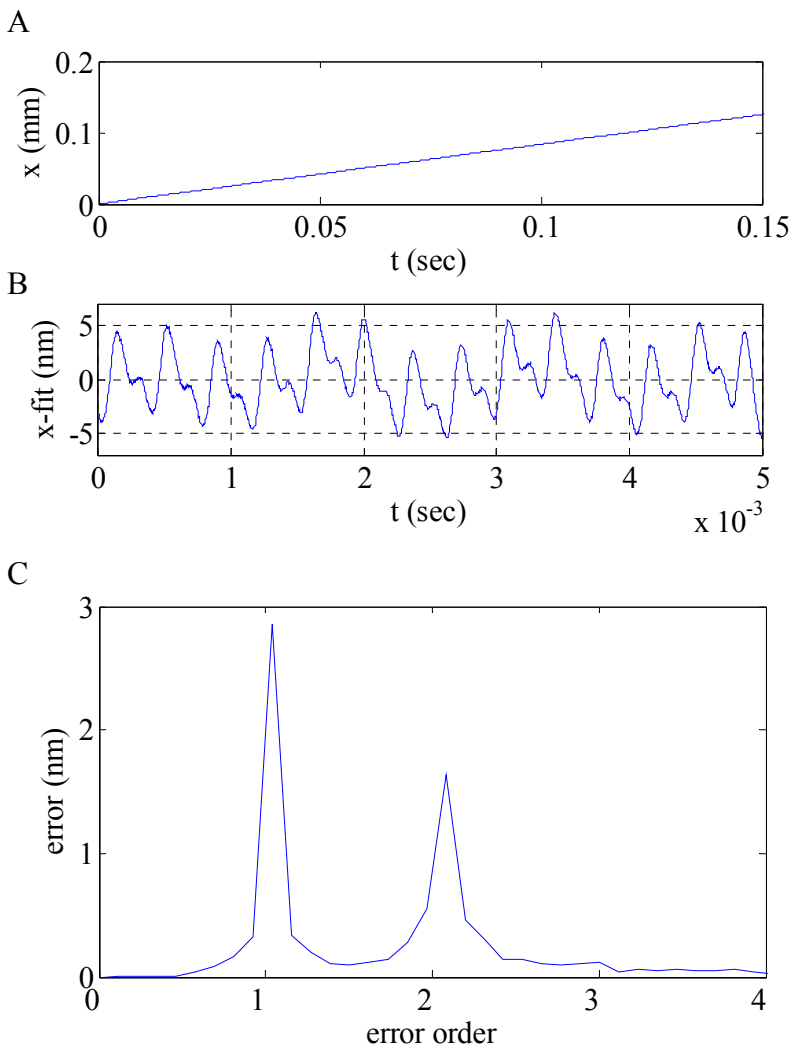

Figure 4-2. Displacement data for misaligned system. A) Measured displacement from typical phase measuring electronics. B) Periodic error revealed by subtracting the least squares best fit line from the measured displacement data. C) Magnitudes of the first and second order periodic errors in the frequency domain where the frequency axis is normalized by error order.

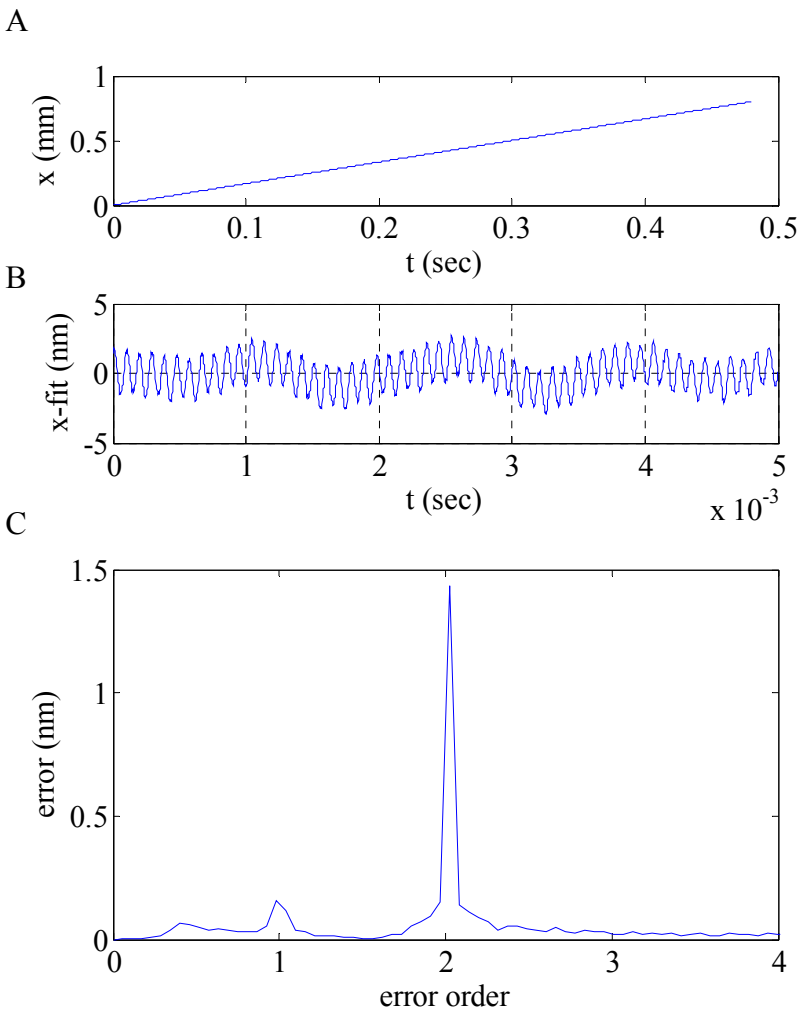

Figure 4-3. Displacement data for well aligned system. A) Measured displacement from typical phase measuring electronics. B) Periodic error is revealed by subtracting the least squares best fit line from the measured displacement data. C) Magnitudes of first and second order periodic error in the frequency domain where the frequency axis is normalized by error order.

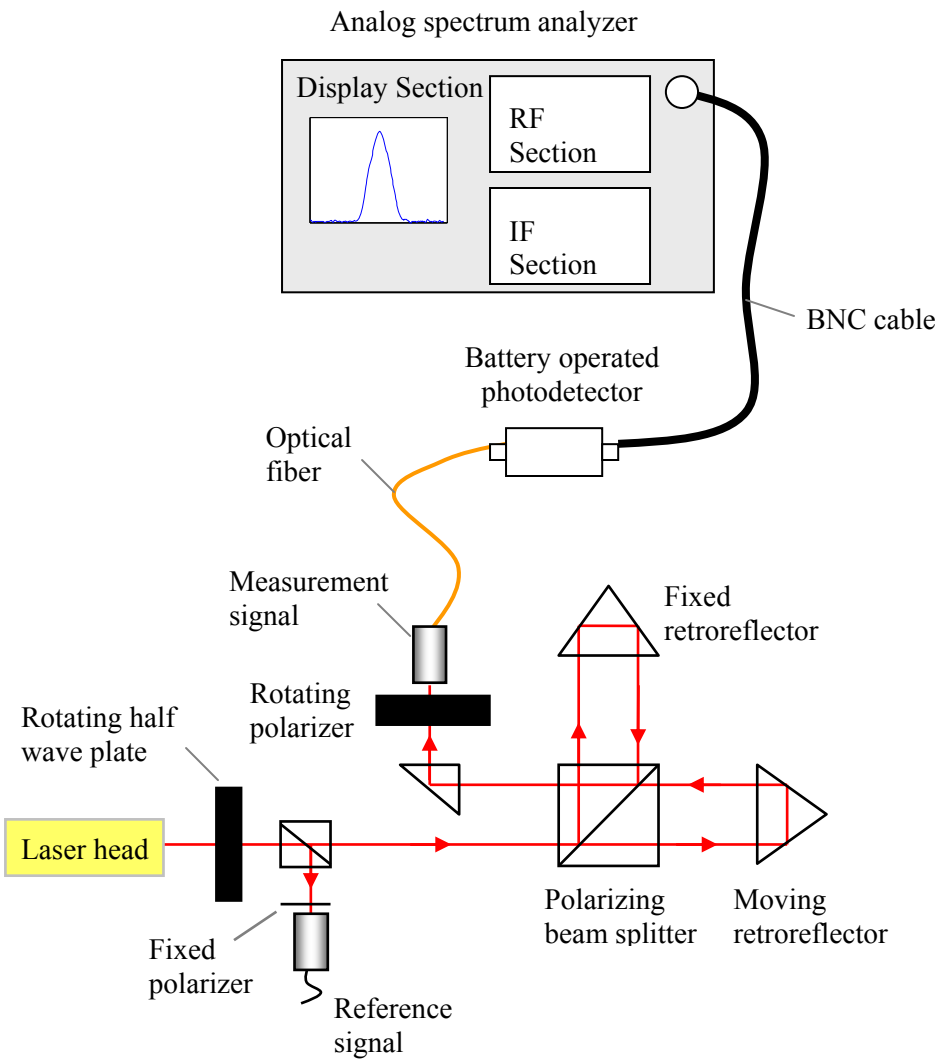

Figure 4-4. Schematic of an analog spectrum analyzer setup to collect measurement signals from the interferometer.

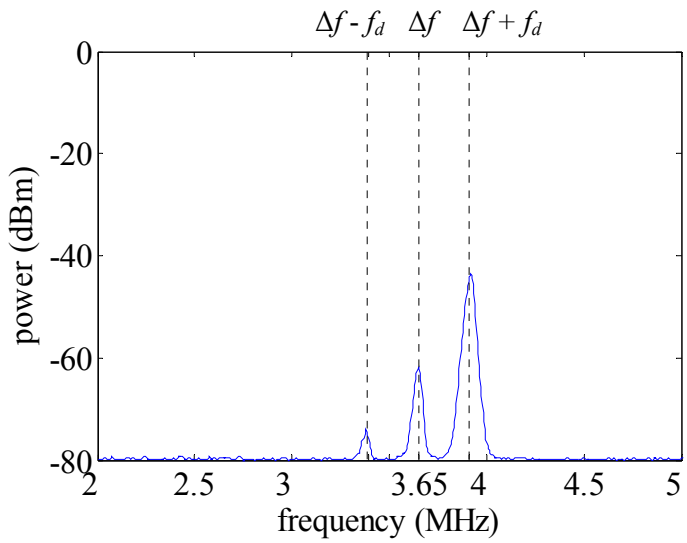

Figure 4-5. Example of frequency content for fully leaking interferometer. The intended *ac interference*, $\Delta f + f_d$, *ac reference* (first order periodic error), Δf, and leakage induced *ac interference* (second order periodic error), $\Delta f - f_d$, signals are observed during $+x$ direction motion (see Fig. 4-1A) at 5,000 mm/min.

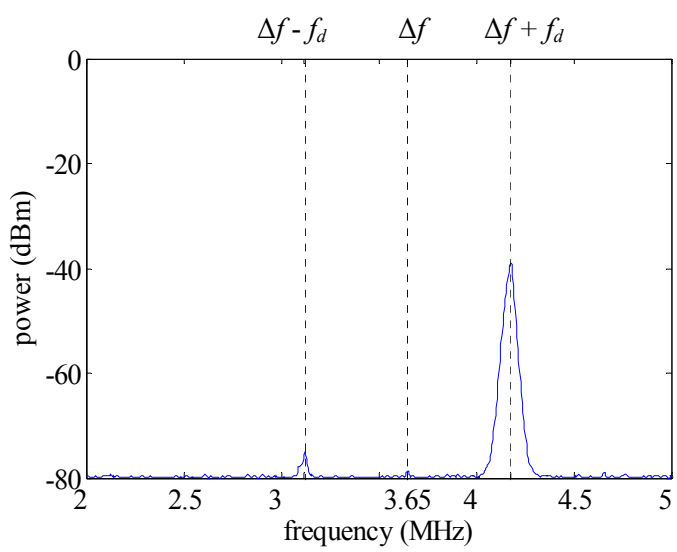

Figure 4-6. Spectral content for nominal angular alignment of the half wave plate and linear polarizer. The target velocity is 10,000 mm/min.

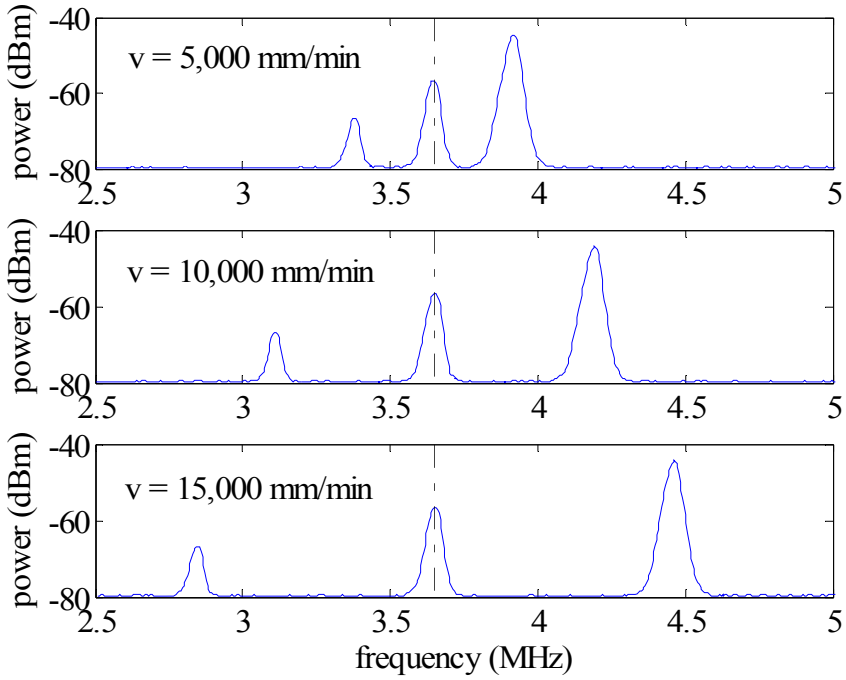

Figure 4-7. Periodic error frequency content at three different velocities. The magnitude is independent of target velocity. The data was collected with 10 deg half wave plate and linear polarizer angular misalignments.

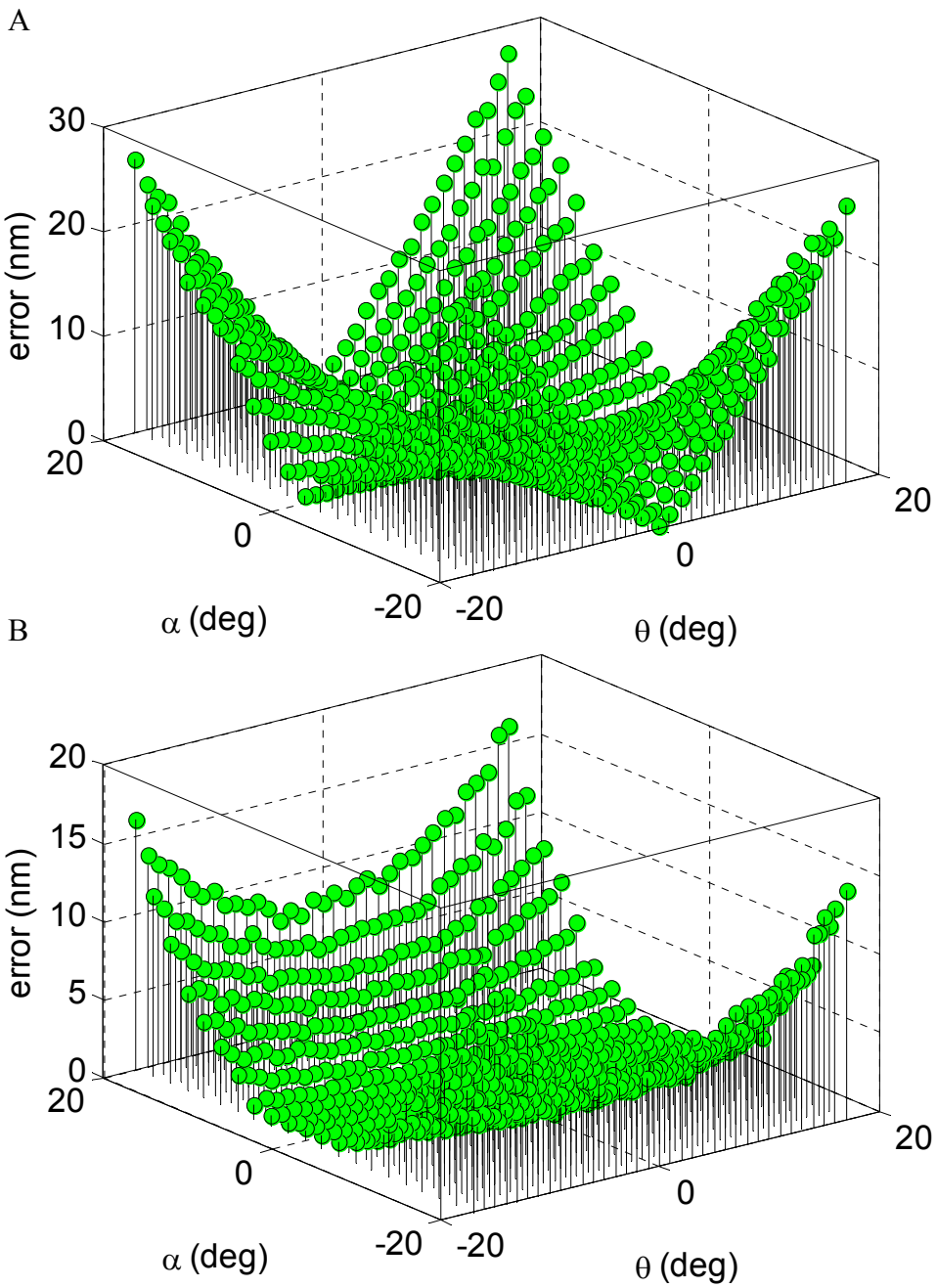

Figure 4-8. Periodic errors for half wave plate/linear polarizer parameter study. The errors were obtained from the discrete Fourier transform of position data. The variables α and θ are the angles of the half wave plate and linear polarizer from their nominal orientations. A) First order periodic error. B) Second order periodic error.

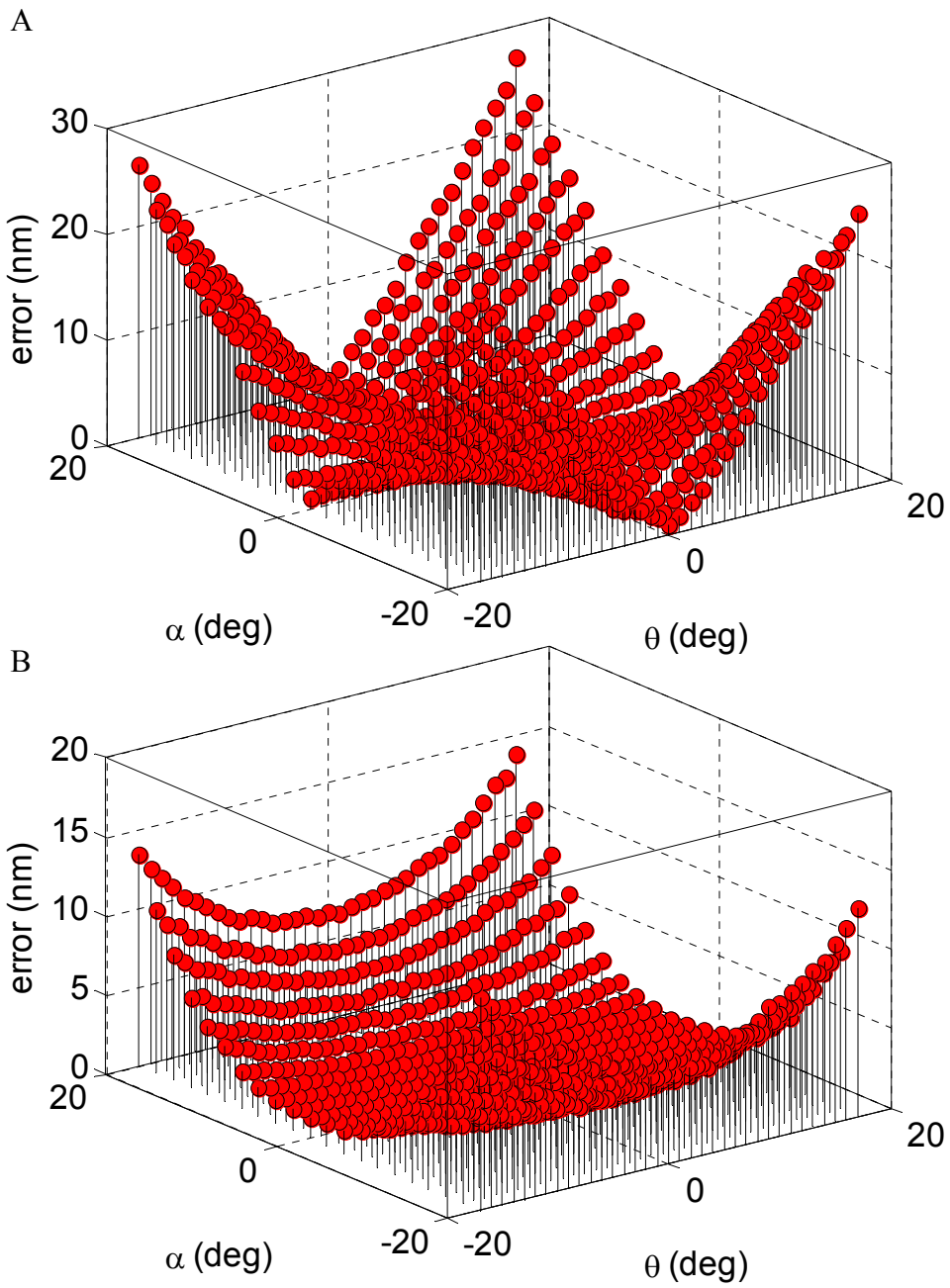

Figure 4-9. Periodic errors for half wave plate/linear polarizer parameter study. The errors were obtained from the spectrum analyzer data. A) First order periodic error. B) Second order periodic error.

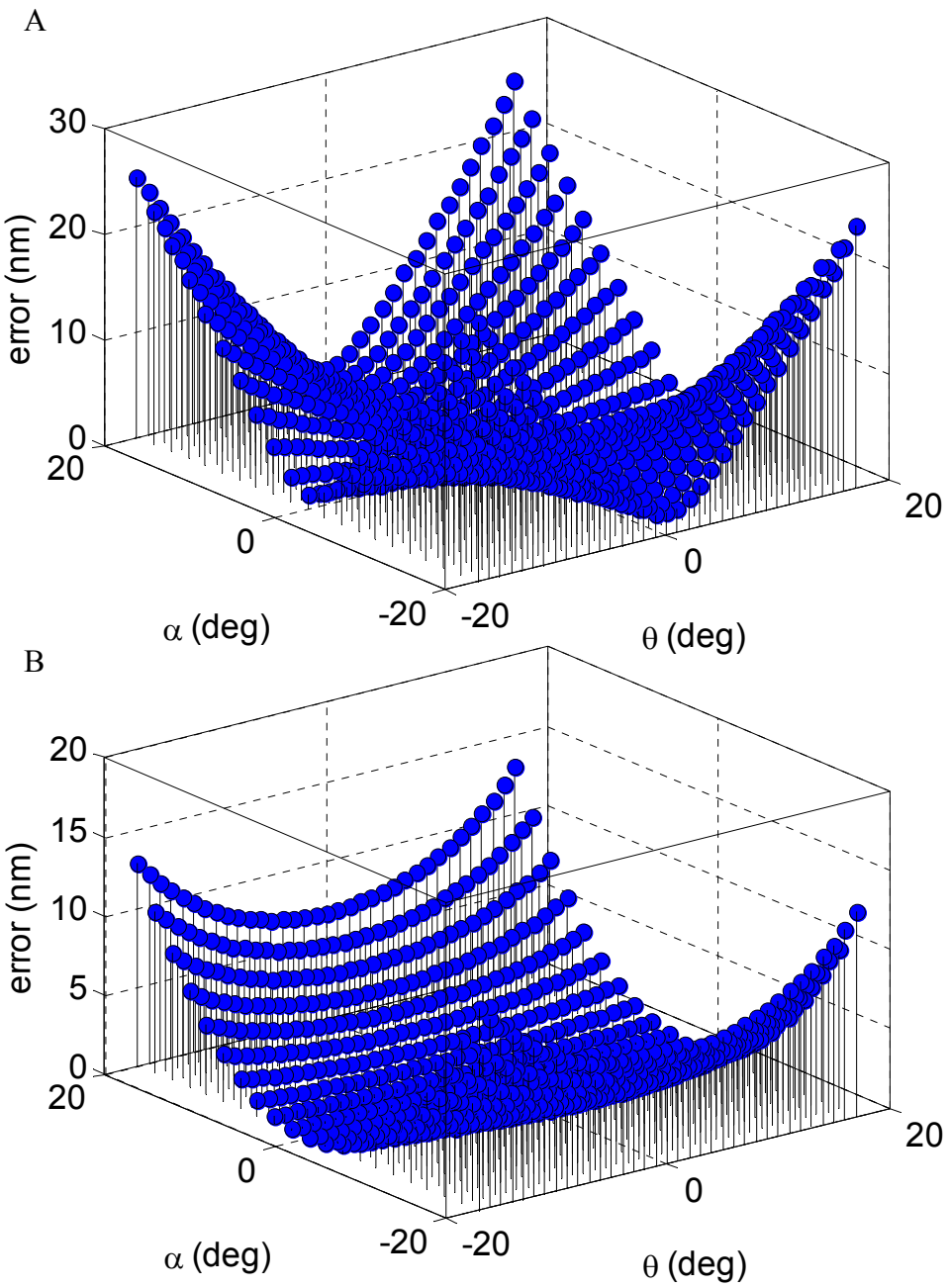

Figure 4-10. Periodic errors for half wave plate/linear polarizer parameter study. The errors were obtained from mean values of the Cosijns *et al.* model Monte Carlo evaluation. A) First order periodic error. B) Second order periodic error.

CHAPTER 5
PERIODIC ERROR CALCULATION FROM SPECTRUM ANALYZER DATA

This chapter describes the Monte Carlo evaluation of a single equation that can be used to determine periodic error magnitudes from spectrum analyzer data. In this approach, the optical interference signal is recorded during constant velocity target motion using a spectrum analyzer and the magnitudes of spectral peaks are used to calculate periodic error magnitudes. This approach builds on prior work [2] by treating the general case where both first and second order error components exist and arbitrary initial phase values are considered. Significant experimental results are presented which verify the new approach.

Error Calculation

Phasor diagrams present a revealing graphical approach to analyzing periodic error. As described in the Chapter 3 (Frequency-Path model), the photodetector current contains not only the desired *ac interference* term, $E_{22}E_{11}\cos\left(\Delta\omega t - k\left(FF\right)x_2 + \phi_{22} - \phi_{11}\right)$, but also the leakage induced *ac interference* term, $E_{21}E_{12}\cos\left(\Delta\omega t + k\left(FF\right)x_2 + \phi_{21} - \phi_{12}\right)$, and two *ac reference* terms, $E_{22}E_{12}\cos\left(\Delta\omega t + \phi_{22} - \phi_{12}\right)$ and $E_{21}E_{11}\cos\left(\Delta\omega t + \phi_{21} - \phi_{11}\right)$. Because the frequency offset is the same (or nearly so) for the two *ac reference* terms, they cannot generally be individually distinguished in the spectrum analyzer display. Therefore, they are considered as a single term with identical frequency and phase in this analysis. These three terms (intended and leakage induced *ac interference* and *ac reference* signals), depicted in the Figure 3-7 spectrum in Chapter 3, may be described using three separate phasors in the complex plane.

Reprinted with permission from Kim, H.S. and Schmitz, T., 2009, Periodic Error Calculation from Spectrum Analyzer Data, Precision Engineering, doi:10.1016/j.precisioneng.2009.06.001.

First, consider the intended *ac interference* term. It can be described as the phasor $\vec{\Gamma}_0 = \Gamma_0 e^{i\left(\Delta\omega t - k\left(FF\right)x_2 + \phi_{22} - \phi_{11}\right)} = \Gamma_0 e^{i\left(\phi + \phi_0\right)}$, where Γ_0 is the magnitude (photodetector current units of Amperes), $\phi = \Delta\omega t - k\left(FF\right)x_2$ (rad) is the nominal phase change due to the measurement target motion and $\phi_0 = \phi_{22} - \phi_{11}$ (rad) is the (arbitrary) initial phase. This phasor rotates at Δf in the complex plane with no motion, due to the split frequency difference, and $\Delta f \pm f_d$ depending on the direction while the moving target is in motion. Alternately, the exponential notation may be replaced by the rectangular coordinate representation shown in Eq. 5-1,

$$\vec{\Gamma}_0 = \Gamma_0 e^{i\left(\phi + \phi_0\right)} = \Gamma_0 \cos\left(\phi + \phi_0\right)\vec{j} + \Gamma_0 \sin\left(\phi + \phi_0\right)\vec{k} \tag{5-1}$$

which specifically identifies the real ($\vec{j}$ axis) and imaginary ($\vec{k}$ axis) components. The moving target position is ideally determined from the instantaneous phase of $\vec{\Gamma}_0$. Under constant velocity conditions, for example, the instantaneous phase grows linearly with time, as does the target position. In practice, the phase measuring electronics frequency shift this term back to zero for no motion, or near zero during target motion, by subtracting the reference (split) frequency. For this analysis, it is convenient to consider this frequency shifted condition so that the $\vec{\Gamma}_0$ phasor is rotating at f_d for constant velocity motion; a counter-clockwise rotation for the selected target direction is assumed here. Note that after the frequency translation, $\phi = -k\left(FF\right)x_2$. See Figure. 5-1A.

Similarly, the *ac reference* term can be expressed in rectangular coordinates as shown in Eq. 5-2.

$$\vec{\Gamma}_1 = \Gamma_1 \cos\left(\phi_1\right)\vec{j} + \Gamma_1 \sin\left(\phi_1\right)\vec{k} \tag{5-2}$$

The orientation of this phasor (see Figure 5-1B) does not vary with time (recall that the phasor after the frequency translation step is considered); its direction is fixed by the arbitrary initial phase ϕ_1 which, in general, differs from ϕ_0.

Finally, the leakage induced *ac interference* term can be expressed in rectangular coordinates as shown in Eq. 5-3.

$$\vec{\Gamma}_2 = \Gamma_2 \cos(\phi - \phi_2)\vec{j} - \Gamma_2 \sin(\phi - \phi_2)\vec{k} \tag{5-3}$$

This phasor (see Figure 5-1C) rotates in the clockwise direction (for counter-clockwise $\vec{\Gamma}_0$ rotation) due to the opposite sign of the Doppler shift. (Again, the frequency translated version of the signals is considered for convenience of explanation.) Its arbitrary initial phase ϕ_2 differs, in general, from both ϕ_0 and ϕ_1.

Prior to determining the periodic error in the general case, consider the presence of only $\vec{\Gamma}_0$ and $\vec{\Gamma}_1$, and then only $\vec{\Gamma}_0$ and $\vec{\Gamma}_2$, individually. It is assumed that the initial phases are zero for now to enable direct comparison to reference [2]. Figure 5-2 depicts the vector sum of the intended *ac interference* and *ac reference* phasors ($\vec{\Gamma}_0$ and $\vec{\Gamma}_1$, respectively) at progressing times during constant velocity motion. In Figure 5-2A, an arbitrary time is selected where the nominal phase (from the intended *ac interference* term) is zero. For zero initial phases, ϕ_0 and ϕ_1, both phasors are directed along the positive real axis. At a later time in Figure 5-2B, the nominal phase is $\phi = \frac{\pi}{2}$ rad, but the actual phase, ϕ', is less than the nominal due to the vector addition of $\vec{\Gamma}_0$ and $\vec{\Gamma}_1$. Recall that the orientation of $\vec{\Gamma}_1$ does not change for the frequency translated condition. The phase error, $\Delta\phi = \phi - \phi'$, is therefore positive and depends on the magnitude of $\vec{\Gamma}_1$. Similar to Figure 5-2A, the phase error in Figure 5-2C is again zero. In Figure 5-2D, the

error is negative, but equal in magnitude to the situation depicted in Figure 5-2B. Figure 5-2E demonstrates the corresponding single cycle of phase error variation per 2π rad of nominal phase change for first order periodic error. By vector addition, the phase error is,

$$\Delta\phi = \phi - \phi' = \phi - \tan^{-1}\left(\frac{\Gamma_0 \sin(\phi)}{\Gamma_0 \cos(\phi) + \Gamma_1}\right) \text{ (rad)} \tag{5-4}$$

and the corresponding first order periodic error is,

$$\varepsilon_1 = \frac{1}{FF}\frac{\lambda}{2\pi}\left(\phi - \tan^{-1}\left(\frac{\Gamma_0 \sin(\phi)}{\Gamma_0 \cos(\phi) + \Gamma_1}\right)\right) \text{ (nm).} \tag{5-5}$$

If the maximum first order periodic error, $\varepsilon_{\max,1}$, is assumed to occur when $\phi = \frac{\pi}{2}$ (see Figure 5-2B), then it can be expressed as,

$$\varepsilon_{\max,1} = \frac{1}{FF}\frac{\lambda}{2\pi}\left(\frac{\pi}{2} - \tan^{-1}\left(\frac{\Gamma_0}{\Gamma_1}\right)\right) \text{ (nm)} \tag{5-5A}$$

which is equivalent to Eq. 5 in reference [2] for the small angle approximation. Equation 5 in reference [2] identifies the maximum phase error magnitude as $\frac{\Gamma_1}{\Gamma_0}$.

Figure 5-3 shows the situation when only $\vec{\Gamma}_0$ (intended *ac interference* signal) and $\vec{\Gamma}_2$ (leakage induced *ac interference* signal) are considered. Again zero initial phases are assumed and an arbitrary time is selected when both phasors are directed along the positive real axis; see Figure 5-3A. Because the vectors are counter-rotating, the geometries shown in Figures 5-3B through 5-3H are obtained for nominal phase values of $\{\frac{\pi}{4}, \frac{\pi}{2}, \frac{3\pi}{4}, \pi, \frac{5\pi}{4}, \frac{3\pi}{2}, \text{and } \frac{7\pi}{4}\}$ rad. The characteristic two cycle phase error variation per 2π rad of nominal phase change (second order periodic error) is depicted in Figure 5-3I. The phase error is calculated according

to: $\Delta\phi = \phi - \phi' = \phi - \tan^{-1}\left(\frac{(\Gamma_0 - \Gamma_2)\sin(\phi)}{(\Gamma_0 + \Gamma_2)\cos(\phi)}\right)$ (rad) and the corresponding second order periodic error is,

$$\varepsilon_2 = \frac{1}{FF}\frac{\lambda}{2\pi}\left(\phi - \tan^{-1}\left(\frac{(\Gamma_0 - \Gamma_2)\sin(\phi)}{(\Gamma_0 + \Gamma_2)\cos(\phi)}\right)\right) \text{ (nm).} \tag{5-6}$$

If the corresponding maximum periodic error is assumed to be obtained when $\phi = \frac{\pi}{4}$ rad (see Figure 5-3B), so that $\sin(\phi) = \cos(\phi) = \frac{\sqrt{2}}{2}$, then the maximum second order periodic error, $\varepsilon_{\max,2}$, is,

$$\varepsilon_{\max,2} = \frac{1}{FF}\frac{\lambda}{2\pi}\left(\frac{\pi}{4} - \tan^{-1}\left(\frac{\Gamma_0 - \Gamma_2}{\Gamma_0 + \Gamma_2}\right)\right) \text{ (nm)} \tag{5-6A}$$

which agrees with Eq. 6 from reference [2] for the small angle approximation. Equation 6 in reference [2] identifies the maximum phase error magnitude as $\frac{\Gamma_2}{\Gamma_0}$.

In general, however, all three phasors, $\vec{\Gamma}_0$, $\vec{\Gamma}_1$, and $\vec{\Gamma}_2$, are present and the initial phases, ϕ_0, ϕ_1,and ϕ_2, are nonzero and unequal. In this case, Eqs. 5-5 and 5-6 may not accurately describe the first and second order periodic error magnitudes in the measured phase/position for all combinations of input parameters. To treat the general case, an expression for the phase error must first be determined. Figures 5-1A, 5-1B, and 5-1C show the individual (frequency translated) phasors with arbitrary phases. They are superimposed in Figure 5-4. Based on this geometry, the phase error can be calculated as,

$$\Delta\phi = \phi + \phi_0 - \phi' = \phi + \phi_0 - \tan^{-1}\left(\frac{\Gamma_0 \sin(\phi + \phi_0) + \Gamma_1 \sin(\phi_1) - \Gamma_2 \sin(\phi - \phi_2)}{\Gamma_0 \cos(\phi + \phi_0) + \Gamma_1 \cos(\phi_1) + \Gamma_2 \cos(\phi - \phi_2)}\right) \text{ (rad)} \tag{5-7}$$

and the corresponding periodic error is,

$$\varepsilon = \frac{1}{FF}\frac{\lambda}{2\pi}\Delta\phi \text{ (nm).} \tag{5-8}$$

Note that the error is dependent on the nominal phase (of the intended *ac interference* signal), the three phasor magnitudes, and the initial phases of the three phasors. To evaluate Eq. 5-8, and identify the periodic error order magnitudes, Monte Carlo simulation is applied. This enables the unknown (uniformly distributed), uncorrelated initial phases to be incorporated. The required steps are:

1. define the values for FF, λ, Γ_0, Γ_1, and Γ_2;
2. select random, uniformly distributed values of ϕ0, ϕ1,and ϕ2 from the range $-\pi \le \phi_i \le \pi$, where i = 0, 1, 2;
3. compute $\Delta\phi$ from Eq. 5-7;
4. compute ε from Eq. 5-8;
5. calculate the discrete Fourier transform of the result from step 4 and normalize the frequency axis to error order (multiply by λ/FF) to identify the individual periodic error contributions from each order; and return to step 2; and
6. after many iterations, the periodic error magnitude for each order is determined from the resulting distributions.

As a first comparison between Eqs. 5-5 and 5-6 (equivalent to Eqs. 5 and 6 from reference [2]) and Eq. 5-8, zero initial phase values are selected. This removes the requirement for Monte Carlo simulation; the periodic error magnitudes are computed directly from the relevant equations, which depend on the phasor magnitudes. Additionally, because spectrum analyzers typically display power data using a logarithmic (dBm) scale, signal amplitudes in this format are applied. To convert from magnitudes, γ_i, in dBm to the (linear) Ampere units for Γ_i included in the previous descriptions, the conversion shown in Eq. 5-9 is applied, where i = 0, 1, 2.

$$\Gamma_i = 10^{\frac{\gamma_i}{20}} \tag{5-9}$$

Figure 5-5 displays first and second order error magnitudes for $\gamma_0 = -15$ dBm, $\gamma_1 = -50$ dBm, and values of γ_2 from {-50 to -20} dBm. In a qualitative sense, the 35 dBm difference between γ_0 and γ_1 corresponds to the attenuation for a well aligned system. While γ_1 and γ_2 do not necessarily vary independently with changes in the optical setup, this approach provides an initial numerical comparison of the different equations. Numerical results for a conventional setup are provided in Figures 5-5 through 5-10. Figure 5-5 shows picometer (pm) level agreement between Eq. 5-8 and Eqs. 5-5 and 5-6 for the case where the γ_1 magnitude is negligible. The expected strong variation in second order error with changes in γ_2 is also observed.

In Figure 5-6, the attenuation between γ_0 and γ_1 is reduced to 15 dBm, $\gamma_0 = -15$ dBm and $\gamma_1 = -30$ dBm. This is characteristic of a misaligned system; note that the first order periodic error is now 10 times larger. The values of γ_2 are varied over the same range. In this case, there is an approximately constant offset in the second order periodic error of 0.8 nm. The residual differences (beyond the second order offset) are at the pm level.

The results for a significantly misaligned system, $\gamma_0 = -15$ dBm and $\gamma_1 = -25$ dBm, are provided in Figure 5-7. It is seen that the second order error for Eq. 5-8 does not increase monotonically with decreased attenuation between γ_0 and γ_2. Rather, a local minimum is seen at $\gamma_2 = -41$ dBm. Figure 5-8 is included to show the differences between Eq. 5-8 and Eqs. 5-5 and 5-6 (the Eq. 5-5 and 5-6 results are subtracted from the Eq. 5-8 results).

Next, the γ_0 and γ_2 magnitudes are fixed, and γ_1 is varied. Figure 5-9 displays the results for $\gamma_0 = -15$ dBm and $\gamma_2 = -50$ dBm (well aligned setup), while γ_1 is varied from {-50 to -20} dBm. As expected the first order periodic error grows with γ_1; the agreement between Eq. 5-8

and Eq. 5-5 is at the pm level. For Eq. 5-8, however, the second order error is strongly influenced by the presence of significant γ_1 spectral content. The difference between the Eq. 5-8 and Eq. 5-6 results exceeds 6 nm for the largest misalignment ($\gamma_1 = -20$ dBm). Also, the second order error behavior is again non-monotonic and reaches a local minimum at $\gamma_1 = -30$ dBm when Eq. 5-8 is applied.

Interesting second order error behavior is also observed for $\gamma_0 = -15$ dBm and $\gamma_2 = -35$ dBm (misaligned setup) and the same variation in γ_1. Figure 5-10 shows that the second order error for Eq. 5-8 is again influenced by γ_1. However, the error now decreases with increasing γ_1 magnitude until a local minimum at – 22 dBm is reached, when the error begins increasing again.

Before comparing the equations with experimental results, the effect of arbitrary initial phase on the periodic error calculations is demonstrated. First, a nonzero initial phase of ϕ_0 = 10 deg = 0.17 rad is considered with $\gamma_0 = -15$ dBm, $\gamma_1 = -30$ dBm, $\gamma_2 = -45$ dBm, and $\phi_1 = \phi_2 =$ 0. The resulting periodic error over 2π of nominal phase change is shown in Figure 5-11. The corresponding discrete Fourier transform magnitude (with frequency normalized to error order) is provided in Figure 5-12. The first order periodic error dominates with a magnitude of 8.96 nm. The second order magnitude is 0.82 nm. Small third order content (0.19 nm) is also observed, although this is not typically considered in most analyses. However, if ϕ_0 is changed to 170 deg = 2.97 rad, for example, the associated error waveform differs; see Figure 5-13. The second order error magnitude now increases to 2.38 nm as shown in Figure 5-14. The third order magnitude also increases to 0.38 nm. Using the previously described Monte Carlo simulation, the variation in periodic error magnitudes with ϕ_0 variation between $\pm\pi$ (uniformly distributed) is determined. See Figure 5-15, where 1000 iterations were completed. The first order error changes very little,

while the second order error varies between 0.80 nm and 2.39 nm. Analogous results are obtained if the other initial phase values are varied, but are not included here for brevity.

Experimental Results

In this section, spectrum analyzer data (γ_0, γ_1, and γ_2 spectral peaks measured in dBm) are used to calculate first and second order periodic error magnitudes via Eqs. 5-5, 5-6, and 5-8. These results are compared with periodic error magnitude values determined from the discrete Fourier transform of position data obtained from traditional phase measuring electronics.

Data were collected for different levels of frequency mixing by varying the linear polarizer and half wave plate angles from their nominal orientations. Figure 4-1A in Chapter 4 shows the test setup that was used to collect data. As noted, Eqs. 5-5, 5-6, and 5-8 were applied to compute the corresponding periodic error. Note that Monte Carlo simulation was used to evaluate Eq. 5-8, which enabled the uniformly distributed, uncorrelated initial phases to be randomly selected over many iterations. In the following analyses, the maximum values from the simulation distributions are presented.

Figure 5-16 displays the case where the linear polarizer angle was varied about its nominal orientation (indicated as zero), while the half wave plate angle was fixed at 10 deg from its nominal angle. A strong variation for γ_1, the *ac reference* term, is observed while γ_0 and γ_2, the intended *ac interference* and leakage induced *ac interference* terms, respectively, are nearly constant. The first order errors calculated by Eqs. 5-5 and 5-8 increase with larger misalignment angles and agrees with the magnitudes calculated from the position data using the discrete Fourier transform. See Figure 5-17A. However, the second order errors computed using Eqs. 5-6 and 5-8 do not agree. As shown in the Figure 5-17B, the Eq. 5-8 results more closely follows the second order error calculated from the position data.

Figure 5-18 shows the difference between the Eq. 5-5, 5-6 and 5-8 calculations and position data (discrete Fourier transform) magnitudes for first and second error order errors; the data from Figure 5-17 was analyzed. It is seen that the Eq. 5-5, 5-6 and 5-8 results agree with the position data for small linear polarizer angular misalignments. For large misalignments, however, Eqs. 5-5 and 5-6 provide less accurate estimates (2.6 nm differences for first order error and 9.5 nm differences for second order error at the largest misalignment). Equation 5-8, on the other hand, agrees to within 1.2 nm for first and 3.0 nm for second order error. These results show that Eq. 5-8, which considers all three spectral peaks, provides a more accurate estimate of the first and second order periodic errors than Eqs. 5-5 and 5-6, respectively, which consider only two periodic error components - either γ_0 and γ_1 (first order, Eq. 5-5) or γ_0 and γ_2 (second order, Eq. 5-6) - especially for significant misalignments from nominal.

Results for a medium misalignment case (5 deg half wave plate angular misalignment) are provided in Figures 5-19 and 5-20. Trends in γ_0, γ_1 and γ_2 variation similar to those identified in Figure 5-16 are observed. This yields the same first and second order periodic error behavior shown in Figures 5-17 and 5-18. Again, Eq. 5-8 more closely agrees with the position data periodic error magnitudes.

When the half wave plate is oriented at its nominal angle, the axes of the two polarized light frequencies emitted from the laser head are well aligned with the axes of the polarization dependent optics. This naturally leads to significantly reduced frequency leakage. Figure 5-21 shows the power level of the three interference terms as a function of the linear polarizer angle. Very little change in the individual power levels is observed and the attenuation between the intended *ac interference* signal, γ_0, and *ac reference*, γ_1, and leakage induced *ac interference*, γ_2, signals is on the order of 33 dBm. Because the signal power levels are constant with the linear

polarizer angle, the first and second order errors calculated by Eqs. 5-5, 5-6, 5-8 are also constant and agree with the periodic error magnitudes determined from the position data; see Figure 5-22.

Next, variation of the half wave plate angle is considered. Figure 5-23 displays results for a 17 deg angular misalignment of the linear polarizer. This figure shows that, while both the *ac reference*, γ_1, and leakage induced *ac interference*, γ_2, terms vary, γ_1 exhibits higher sensitivity to the half wave plate angle. Figure 5-24 shows the corresponding first and second order periodic error comparisons. As seen previously, the Eq. 5-8 results agree more closely with the position data error magnitudes, particularly for second order error under significant misalignments. Figure 5-25 shows the associated error magnitude differences.

In Figure 5-26, the linear polarizer was set at its nominal orientation and the half wave plate angle was varied. It is seen that only the leakage induced *ac interference* term, γ_2 varies. The first order error is therefore constant and the Eq. 5-5 and 5-8 results agree with the position data first order error magnitudes. See the top panel of Figure 5-27. Similarly, both the Eq. 5-6 and 5-8 results agree with the position data second order error magnitudes as seen in the bottom panel of Figure 5-27. The Eq. 5-6 agreement occurs because γ_1 does not change with the half wave plate angle.

As a final example, Figure 5-28 shows the discrete Fourier transform of position data collected using a significantly misaligned system (half wave plate angle is 5 deg from nominal and the linear polarizer is 10 deg from nominal). The existence of third order error is observed. The magnitudes are: 6.3 nm (first order), 2.1 nm (second order), and 0.3 nm (third order). The power levels of the three interference terms using the same configuration were also measured using the spectrum analyzer; the values were: $\gamma_0 = -45.5$ dBm, $\gamma_1 = -62.8$ dBm, and

$\gamma_2 = -74.5$ dBm. The corresponding maximum error magnitudes calculated using a Monte Carlo evaluation of Eq. 5-8 are: 6.1 nm (first order), 2.0 nm (second order), and 0.2 nm (third order).

Discussion

The data shown in Figure 5-29 were collected with a 10 deg linear polarizer misalignment, while the half wave plate angle was varied. Maximum, minimum, and mean values of the first and second order error magnitudes determined from a Monte Carlo evaluation of Eq. 5-8 are presented, together with the Eq. 5-5 and 5-6 results and position data magnitudes. It is seen that the spread in first order error values obtained from Eq. 5-8 (Figure 5-29A) is small. This suggests that the calculation is not particularly sensitive to the initial phases of the three interference terms. For the second order error calculations (Figure 5-29B), however, the spread is significant. As reported in the previous figures, the maximum errors (the upper bound of the band) from simulation agree well with the position data error magnitudes. The mean values, however, track more closely with the Eq. 5-6 results. This outcome suggests that the assumption of uncorrelated arbitrary phases may be incorrect. However, in a practical sense, Eq. 5-8 still provides accurate estimates for both first and second periodic error magnitudes (under arbitrary misalignments) provided the maximum value from the Monte Carlo evaluation is applied.

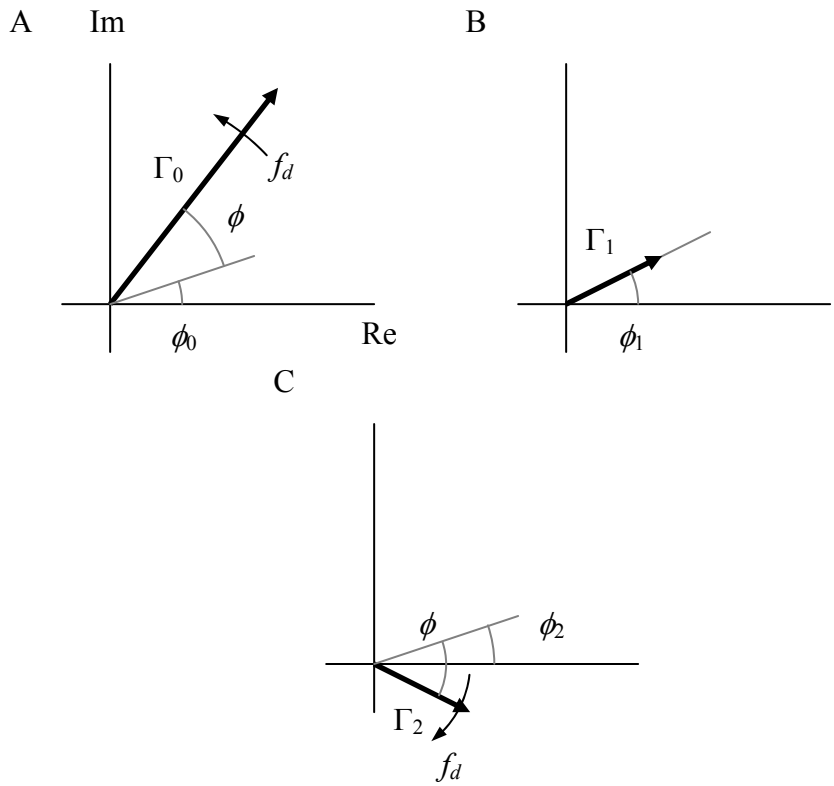

Figure 5-1. Phasor diagrams. A) Intended *ac interference* signal. B) The *ac reference* signal. C) Leakage induced *ac interference* signal.

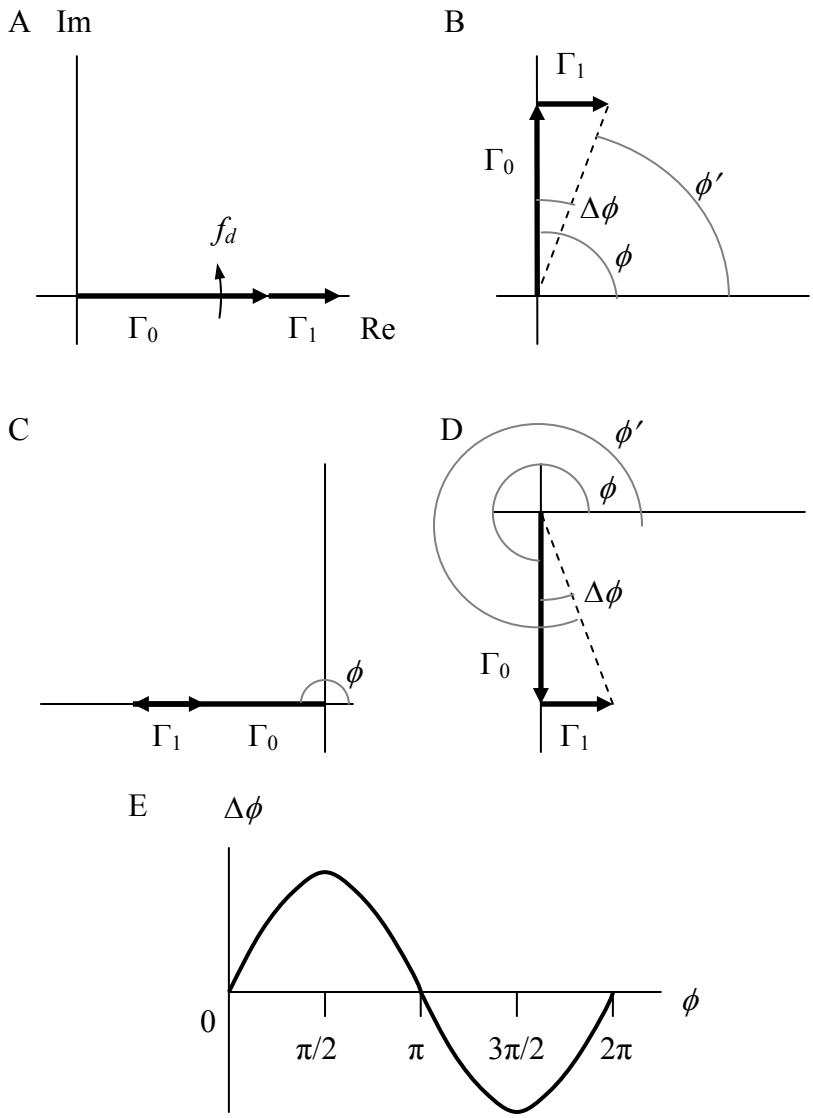

Figure 5-2. Periodic error in the presence of $\vec{\Gamma}_0$ and $\vec{\Gamma}_1$ only for various nominal phase angles (rad). A) 0. B) $\frac{\pi}{2}$. C) π. D) $\frac{3\pi}{2}$. E) The single cycle of phase error variation per 2π rad of nominal phase change.

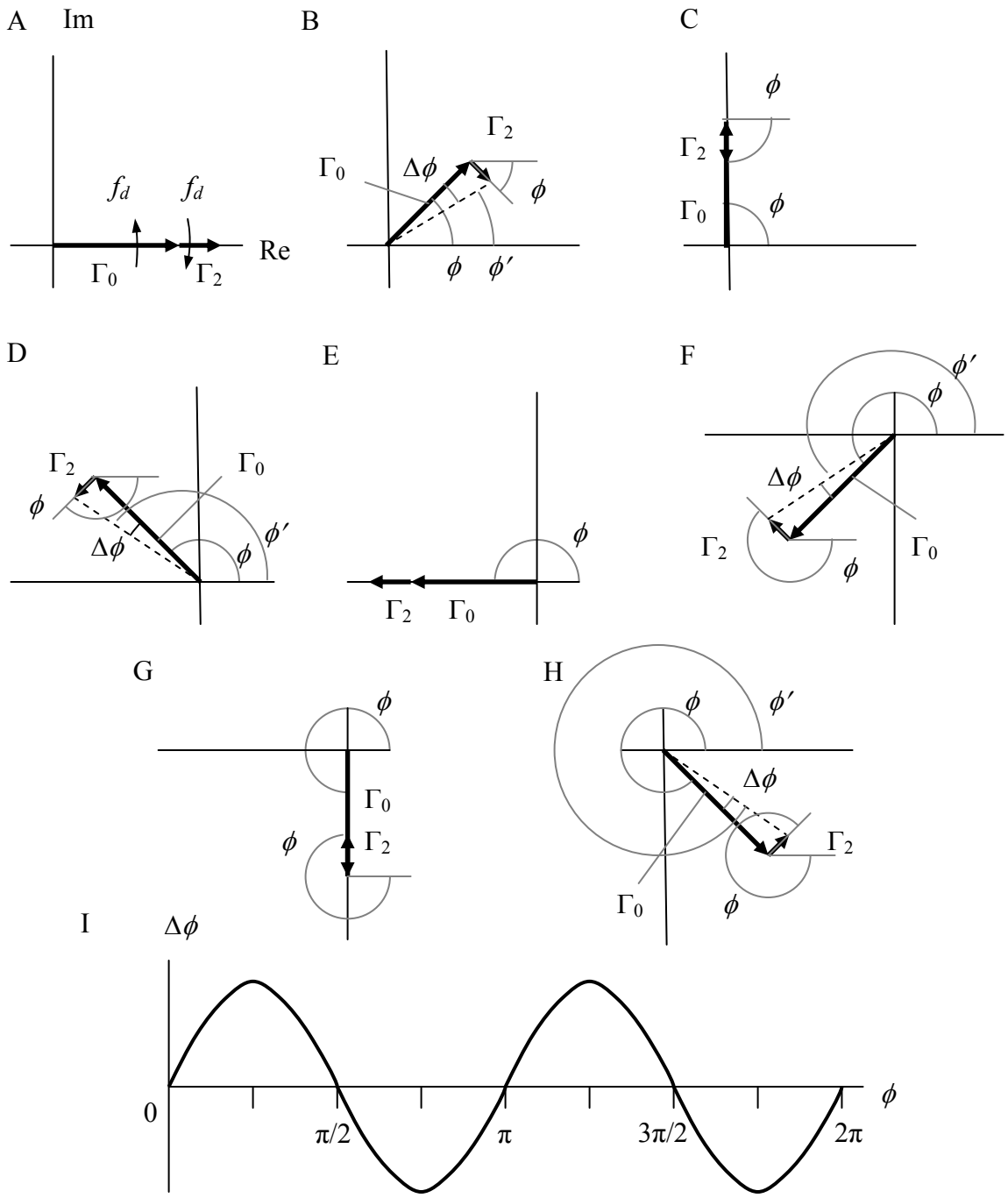

Figure 5-3. Periodic error in the presence of $\vec{\Gamma}_0$ and $\vec{\Gamma}_2$ only for various nominal phase angles (rad). A) 0. B) $\frac{\pi}{4}$. C) $\frac{\pi}{2}$. D) $\frac{3\pi}{4}$. E) π. F) $\frac{5\pi}{4}$. G) $\frac{3\pi}{2}$. H) $\frac{7\pi}{4}$. I) The two cycles of phase error variation per 2π rad of nominal phase change are shown.

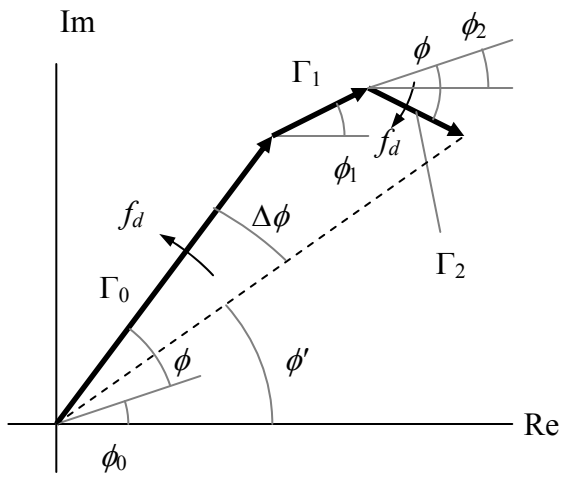

Figure 5-4. Phasor diagram for general case where the intended and leakage induced *ac interference* and *ac reference* signals are present with arbitrary initial phases.

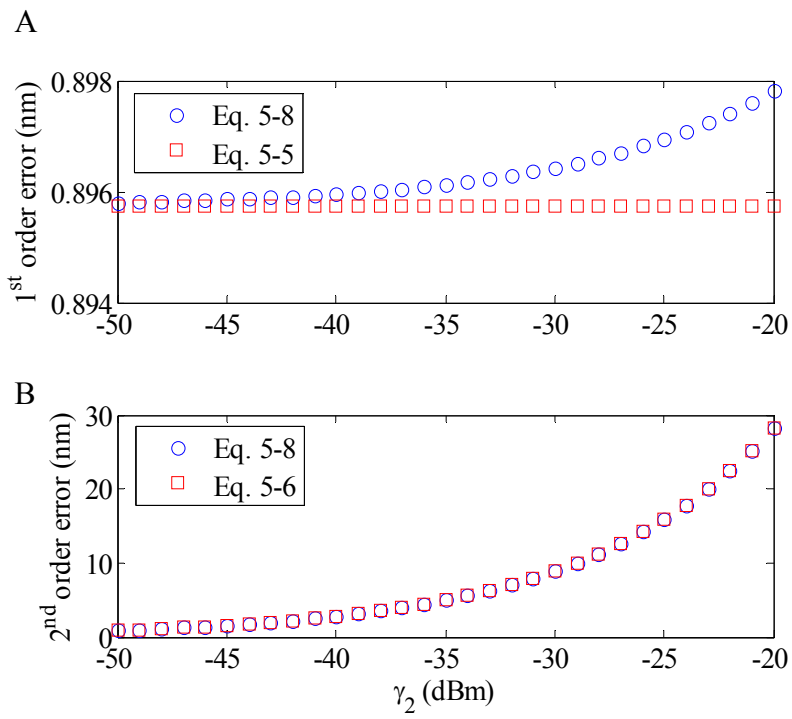

Figure 5-5. Comparison between periodic error magnitudes obtained from Eq. 5-8 and Eqs. 5-5 and 5-6 for $\gamma_0 = -15$ dBm, $\gamma_1 = -50$ dBm, and variable γ_2. The agreement is at the picometer level. A) The magnitude of first order periodic error variation. B) The magnitude of second order periodic error variation.

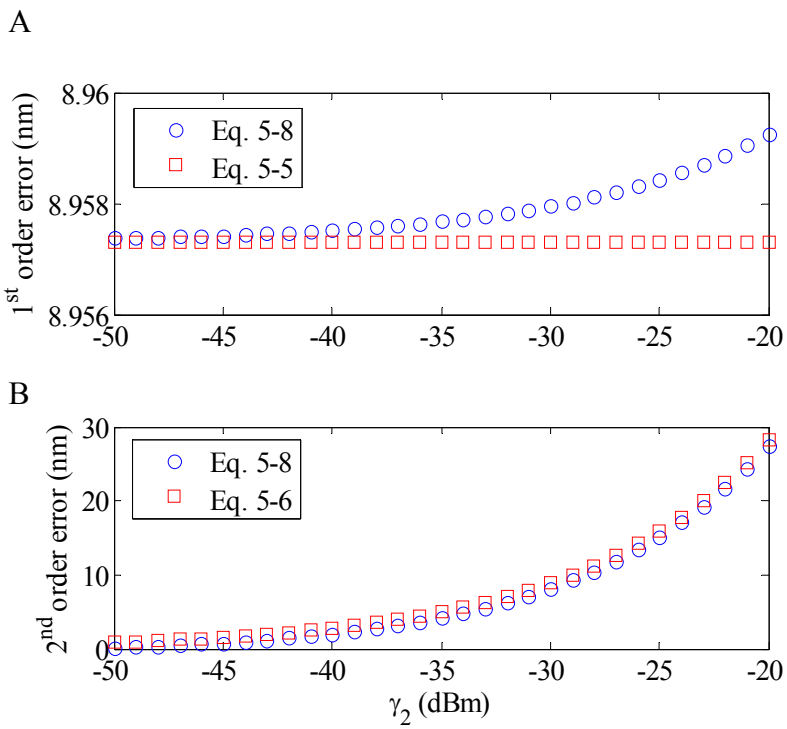

Figure 5-6. Comparison between periodic error magnitudes obtained from Eq. 5-8 and Eqs. 5-5 and 5-6 for $\gamma_0 = -15$ dBm, $\gamma_1 = -30$ dBm, and variable γ_2. There is approximately a 0.8 nm offset in the second order periodic error. A) The magnitude of first order periodic error variation. B) The magnitude of second order periodic error variation.

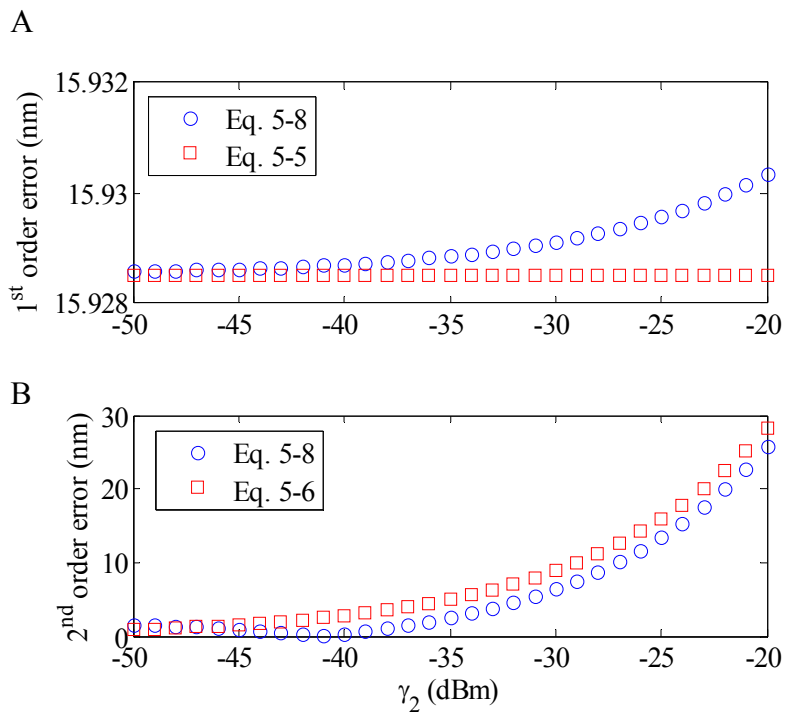

Figure 5-7. Comparison between periodic error magnitudes obtained from Eq. 5-8 and Eqs. 5-5 and 5-6 for $\gamma_0 = -15$ dBm, $\gamma_1 = -25$ dBm, and variable γ_2. The second order error no longer increases monotonically for the Eq. 5-8 calculations. A) The magnitude of first order periodic error variation. B) The magnitude of second order periodic error variation.

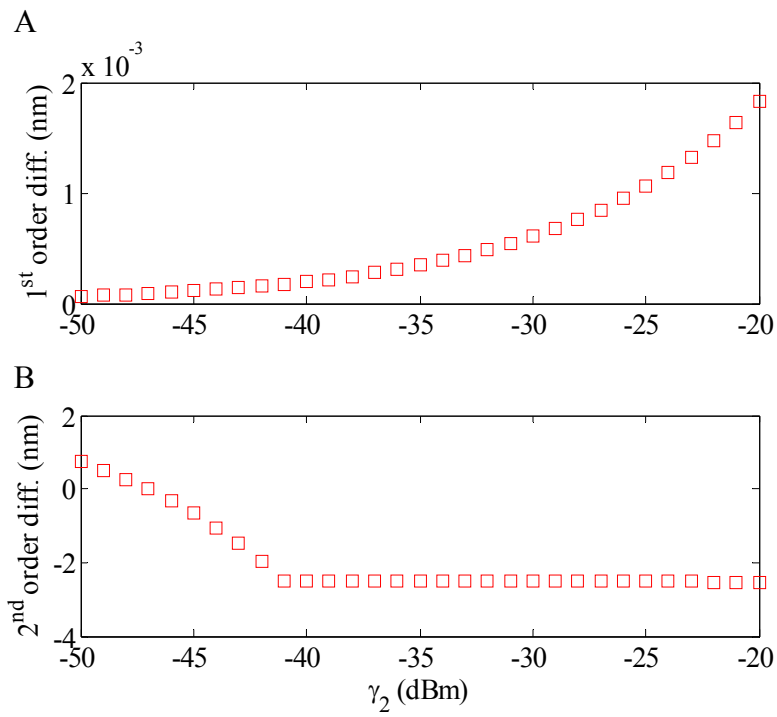

Figure 5-8. Difference between periodic error magnitudes obtained from Eq. 5-8 and Eqs. 5-5 and 5-6 for $\gamma_0 = -15$ dBm, $\gamma_1 = -25$ dBm, and variable γ_2. A) The first order periodic error variation with respect to various γ_2. B) The second order periodic error variation with respect to various γ_2.

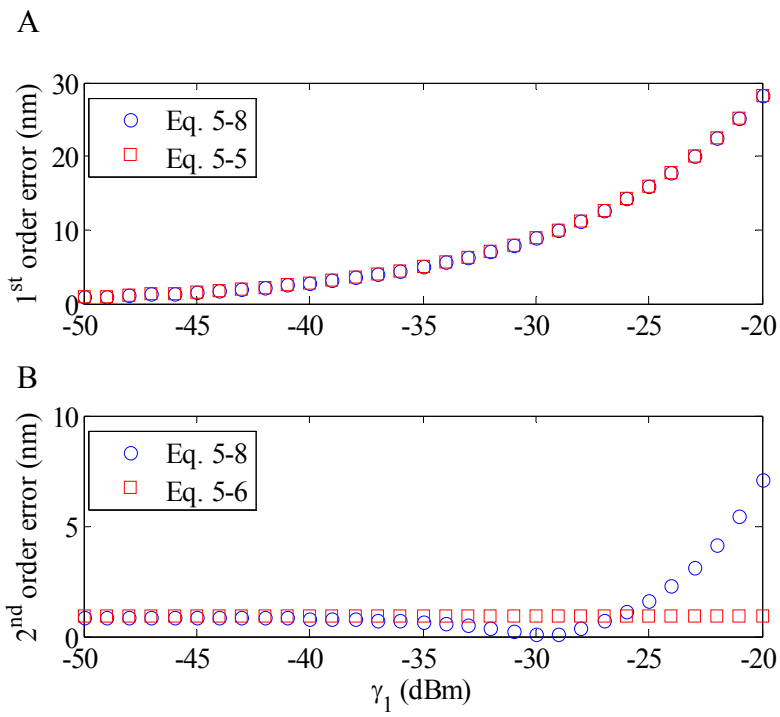

Figure 5-9. Comparison between periodic error magnitudes obtained from Eq. 5-8 and Eqs. 5-5 and 5-6 for $\gamma_0 = -15$ dBm, $\gamma_2 = -50$ dBm, and variable γ_1. The second order error is influenced by the variable γ_1 magnitude when using Eq. 5-8. A) The magnitude of first order periodic error variation. B) The magnitude of second order periodic error variation.

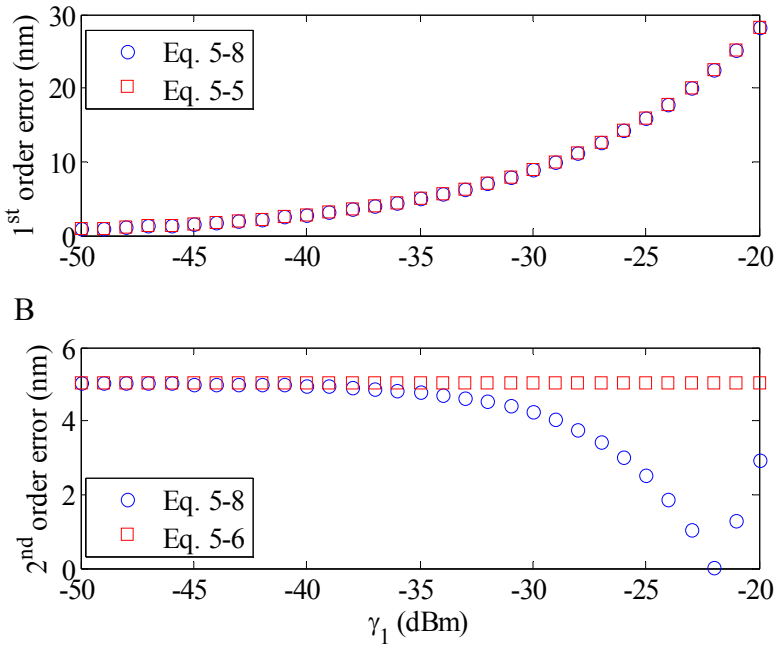

Figure 5-10. Comparison between periodic error magnitudes obtained from Eq. 5-8 and Eqs. 5-5 and 5-6 for $\gamma_0 = -15$ dBm, $\gamma_2 = -35$ dBm, and variable γ_1. The second order error from Eq. 5-8 is again influenced by the variable γ_1 magnitude; it reaches a local minimum at –22 dBm. A) The magnitude of first order periodic error variation. B) The magnitude of second order periodic error variation.

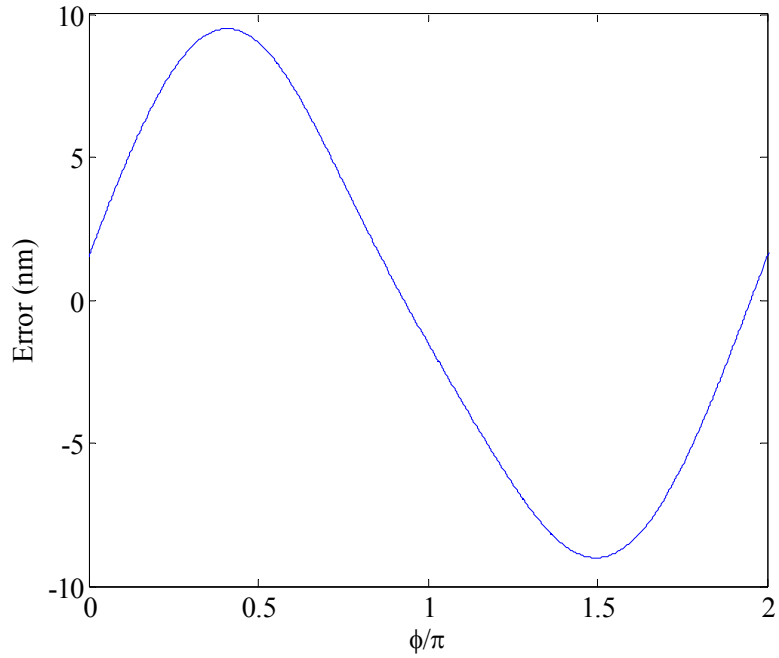

Figure 5-11. Periodic error for ϕ_0 = 10 deg = 0.17 rad with $\gamma_0 = -15$ dBm, $\gamma_1 = -30$ dBm, $\gamma_2 = -45$ dBm, and $\phi_1 = \phi_2 = 0$.

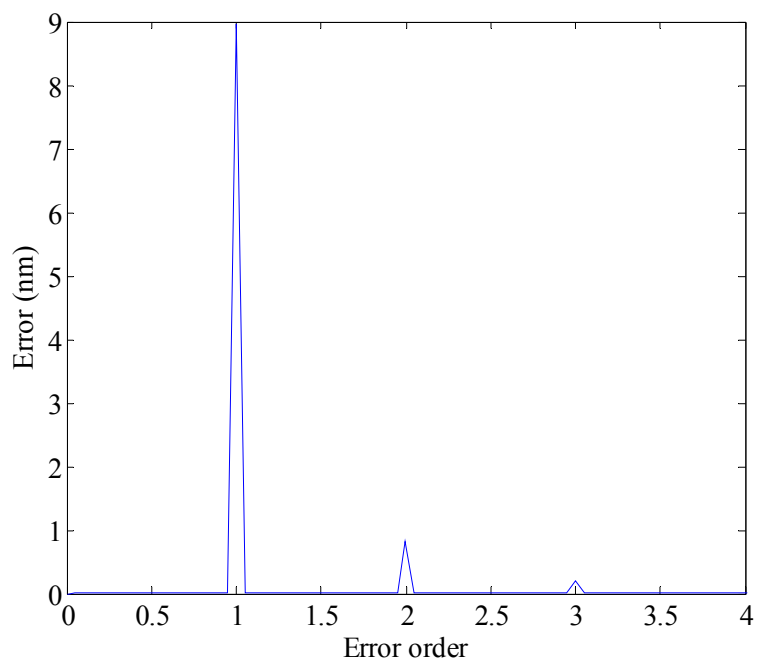

Figure 5-12. Periodic error magnitudes for ϕ_0 = 10 deg = 0.17 rad with $\gamma_0 = -15$ dBm, $\gamma_1 = -30$ dBm, $\gamma_2 = -45$ dBm, and $\phi_1 = \phi_2 = 0$.

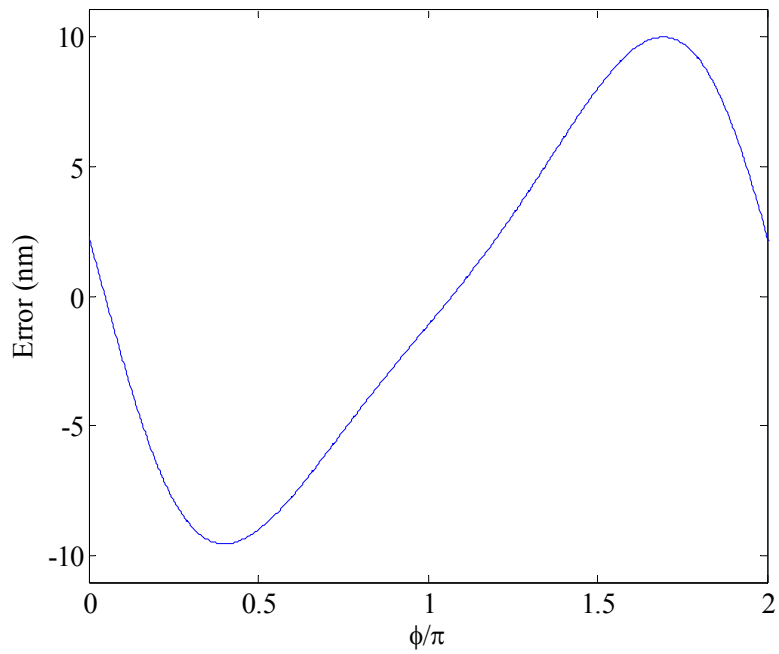

Figure 5-13. Periodic error for ϕ_0 = 170 deg = 2.97 rad with $\gamma_0 = -15$ dBm, $\gamma_1 = -30$ dBm, $\gamma_2 = -45$ dBm, and $\phi_1 = \phi_2 = 0$.

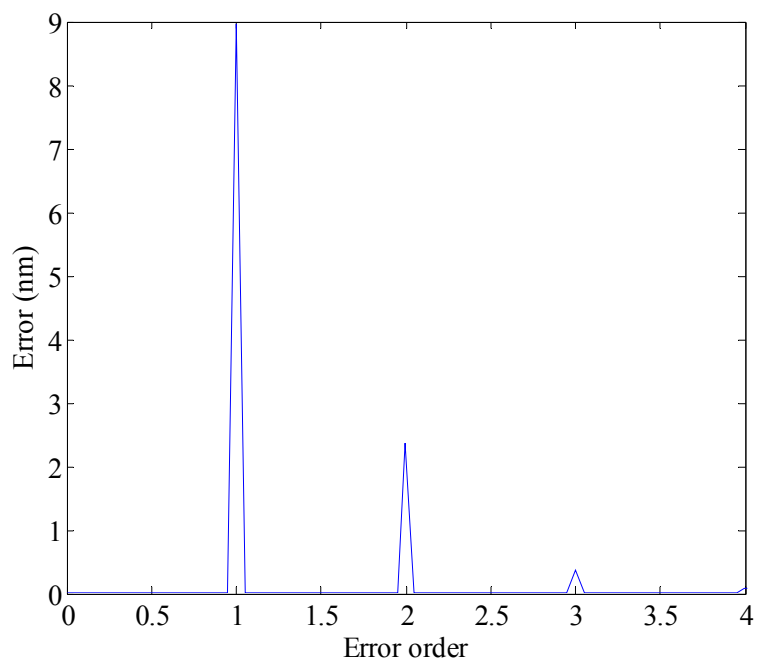

Figure 5-14. Periodic error magnitudes for ϕ_0 = 170 deg = 2.97 rad with $\gamma_0 = -15$ dBm, $\gamma_1 = -30$ dBm, $\gamma_2 = -45$ dBm, and $\phi_1 = \phi_2 = 0$.

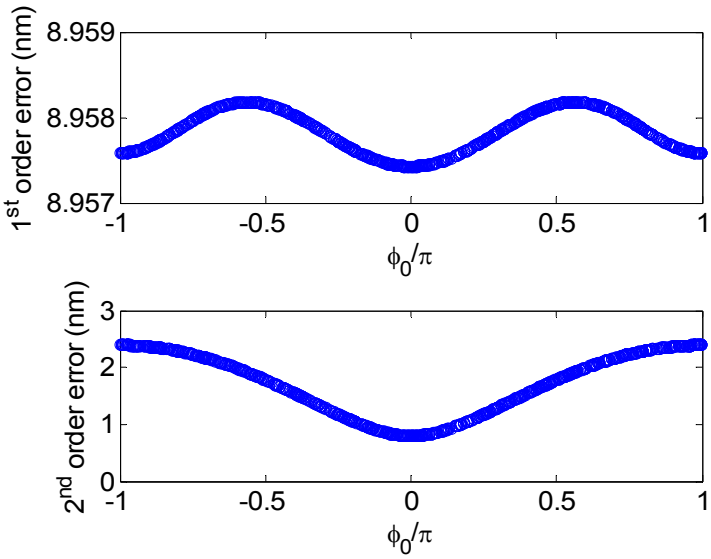

Figure 5-15. Variation in periodic error magnitudes for random ϕ_0 values ($\pm\pi$ range) with $\gamma_0 = -15$ dBm, $\gamma_1 = -30$ dBm, $\gamma_2 = -45$ dBm, and $\phi_1 = \phi_2 = 0$.

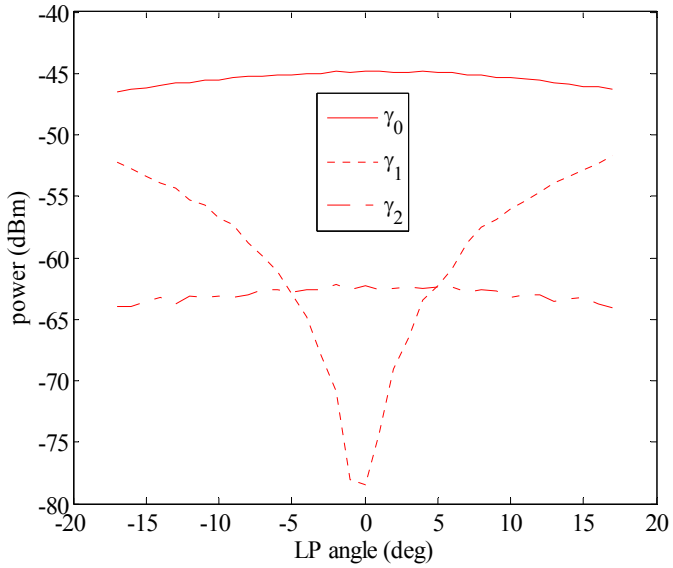

Figure 5-16. Variation of γ_0, γ_1, and γ_2 with linear polarizer (LP) angle. The half wave plate (HWP) was fixed at 10 deg from its nominal orientation (a large misalignment configuration). Strong variation of γ_1 is observed.

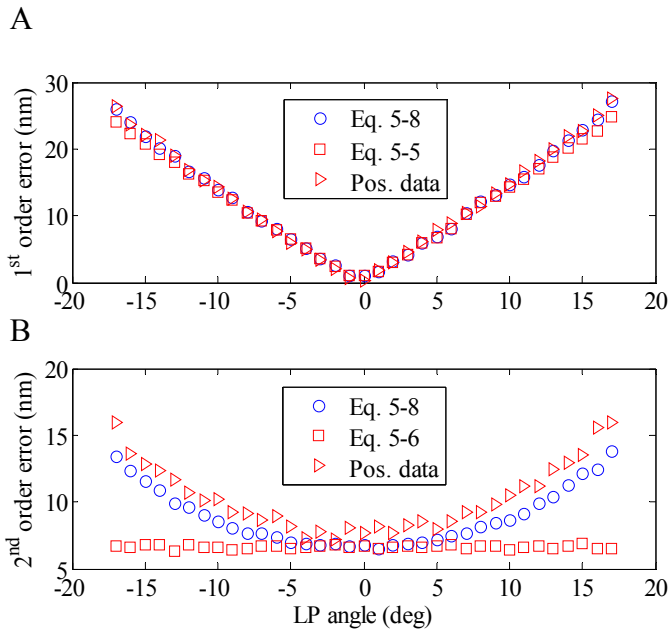

Figure 5-17. Periodic errors calculated by Eqs. 5-5, 5-6, and 5-8 are compared to magnitudes computed using the discrete Fourier transform of position data. The agreement is good for first order error, but only Eq. 5-8 reproduces the second order error. A) The magnitude of first order periodic error. B) The magnitude of second order periodic error.

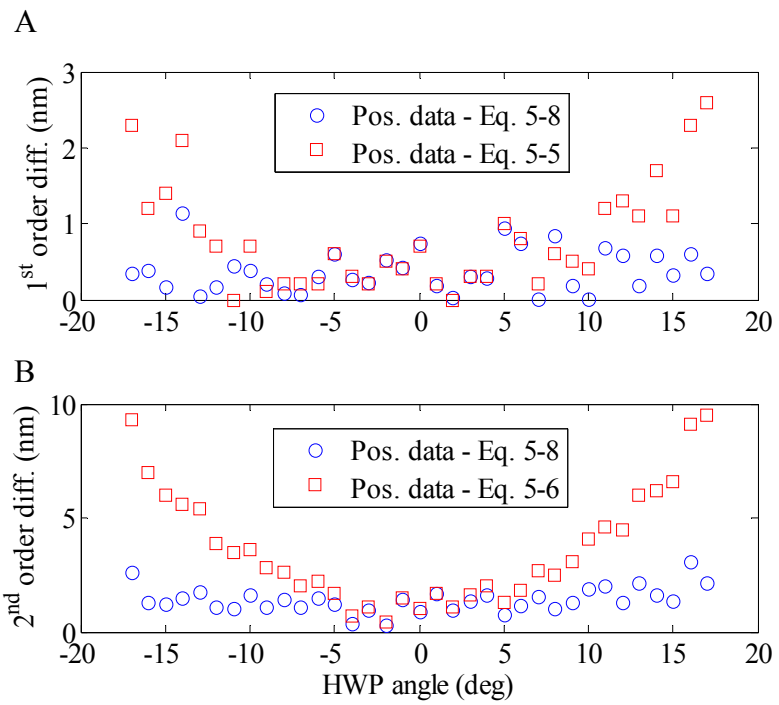

Figure 5-18. Differences between magnitudes from Eqs. 5-5, 5-6, and 5-8 and discrete Fourier transform of position data. A) The first order error. B) The second order error. The differences were calculated from the errors displayed in Figure 5-17.

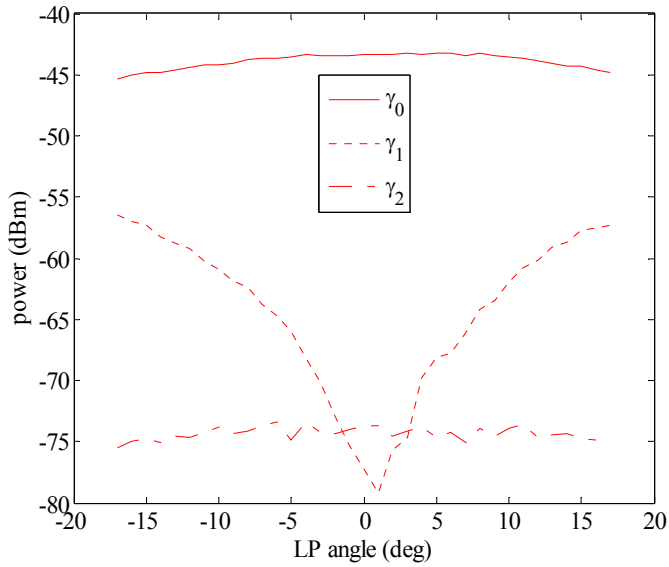

Figure 5-19. Variation of γ_0, γ_1, and γ_2 with linear polarizer (LP) angle. The half wave plate was fixed at 5 deg from its nominal orientation (a medium misalignment configuration). Strong variation of γ_1 is again observed.

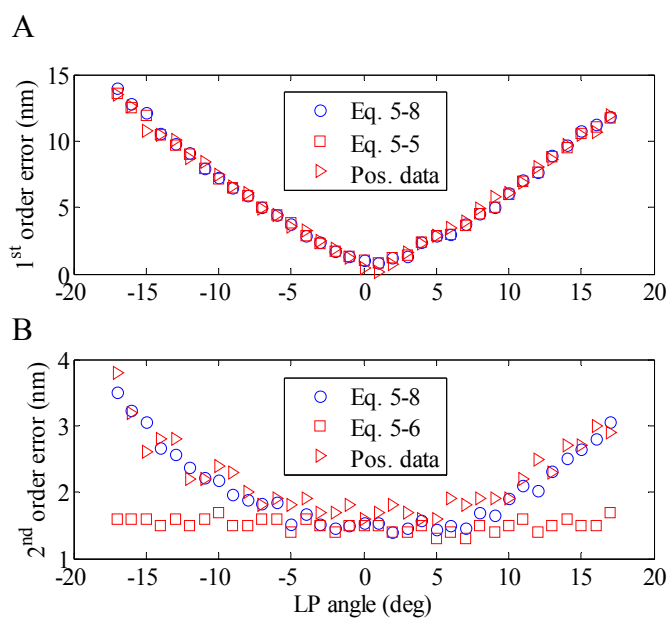

Figure 5-20. Periodic errors calculated by Eqs. 5-5, 5-6, and 5-8 are compared to magnitudes computed using the discrete Fourier transform of position data. The agreement is good for first order error, but only Eq. 5-8 reproduces the second order error. A) The magnitude of first order periodic error. B) The magnitude of second order periodic error.

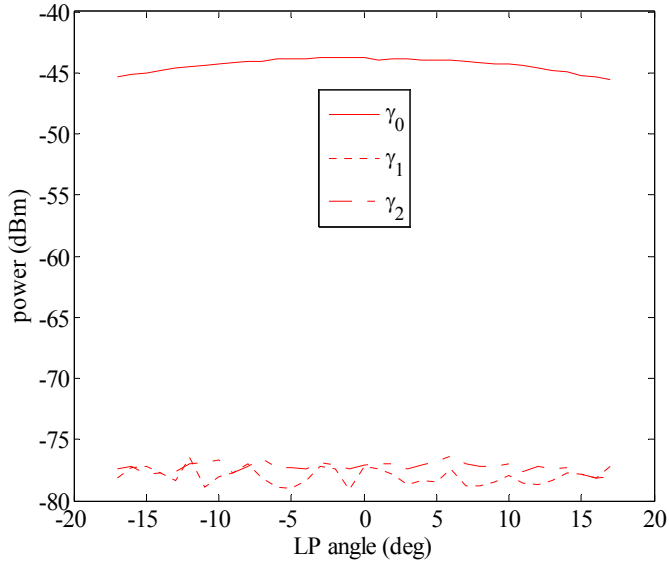

Figure 5-21. Variation of γ_0, γ_1, and γ_2 with linear polarizer (LP) angle. The half wave plate was fixed at its nominal orientation (a well aligned configuration). All three signals are nearly constant.

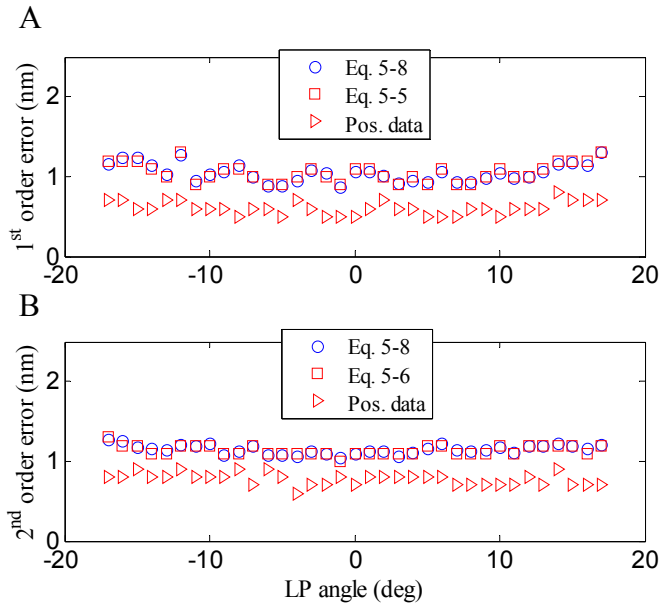

Figure 5-22. Periodic error calculated by Eqs. 5-5, 5-6, and 5-8 agree with the position data results because γ_1 and γ_2 do not vary with linear polarizer angle for the well aligned system. A) The magnitude of first order periodic error. B) The magnitude of second order periodic error.

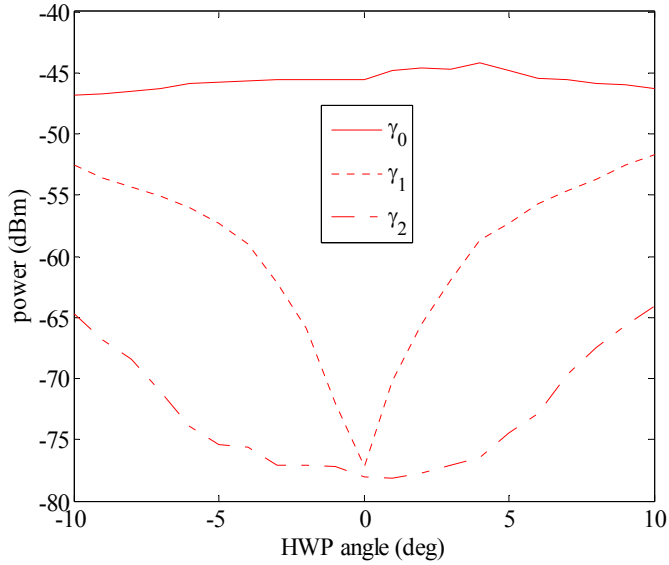

Figure 5-23. Variation of γ_0, γ_1, and γ_2 with half wave plate (HWP) angle. The linear polarizer was misaligned by 17 deg from nominal. Both γ_1 and γ_2 vary.

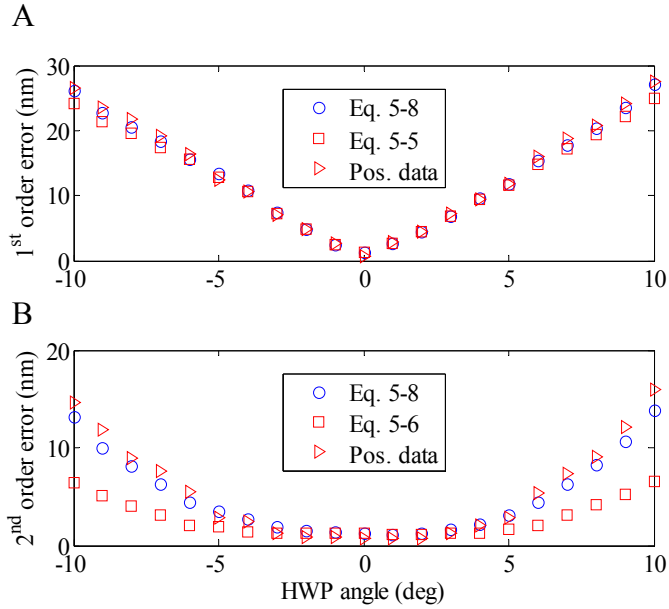

Figure 5-24. Periodic error calculated by Eqs. 5-5, 5-6, and 5-8 are compared to position data error magnitudes (the linear polarizer misalignment angle was 17 deg from nominal). Improved agreement is observed for the Eq. 5-8 results, particularly in the second order error case at large misalignments. A) The magnitude of first order periodic error. B) The magnitude of second order periodic error.

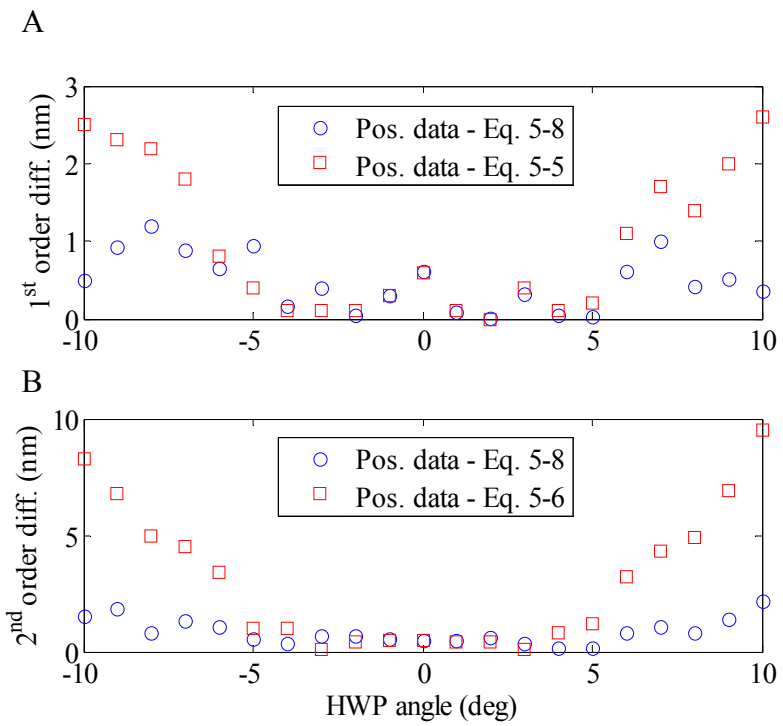

Figure 5-25. Differences between magnitudes from Eqs. 5-5, 5-6, and 5-8 and discrete Fourier transform of position data. A) The first order error. B) The second order error. The differences were calculated from the errors displayed in Figure 5-24.

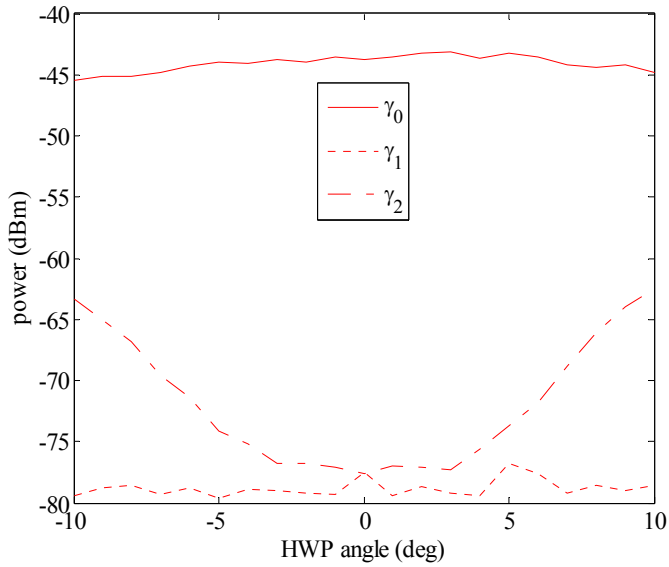

Figure 5-26. Variation of γ_0, γ_1, and γ_2 with half wave plate (HWP) angle. The linear polarizer was fixed at its nominal orientation. Only γ_2 varies.

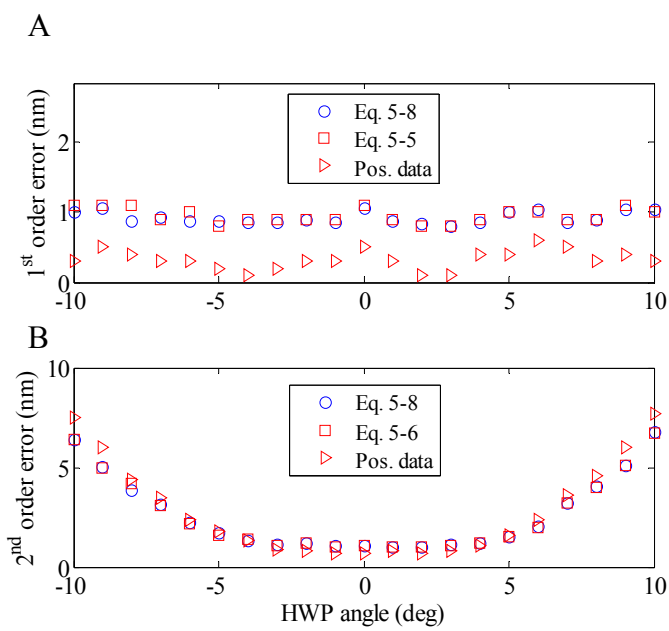

Figure 5-27. Periodic error calculated by Eqs. 5-5, 5-6, and 5-8 agree with the position data error magnitudes (the linear polarizer angle was fixed at its nominal orientation). Note that only γ_2 varies, while γ_1 remains constant. A) The magnitude of first order periodic error. B) The magnitude of second order periodic error.

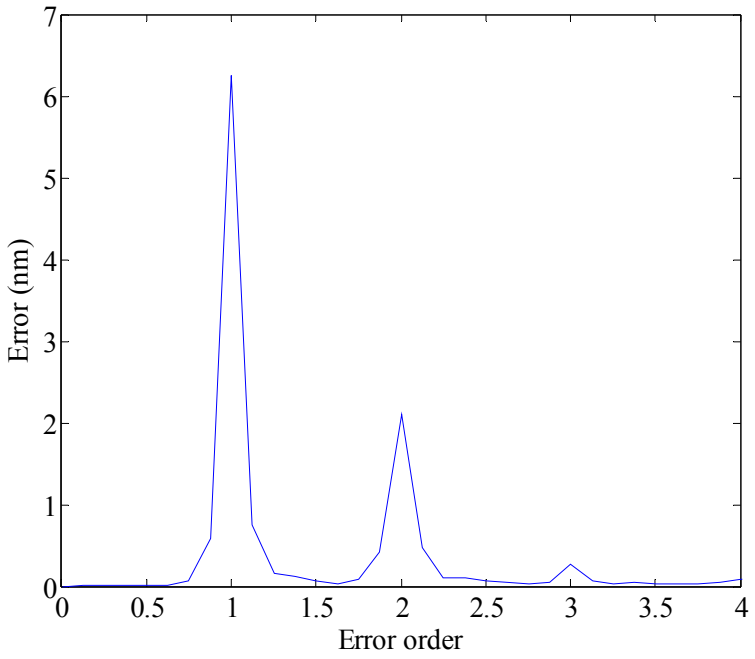

Figure 5-28. The spectrum of position data (normalized to error order) contains first, second, and third order periodic error. The data was obtained for 5 deg half wave plate and 10 deg linear polarizer misalignments from their nominal angles.

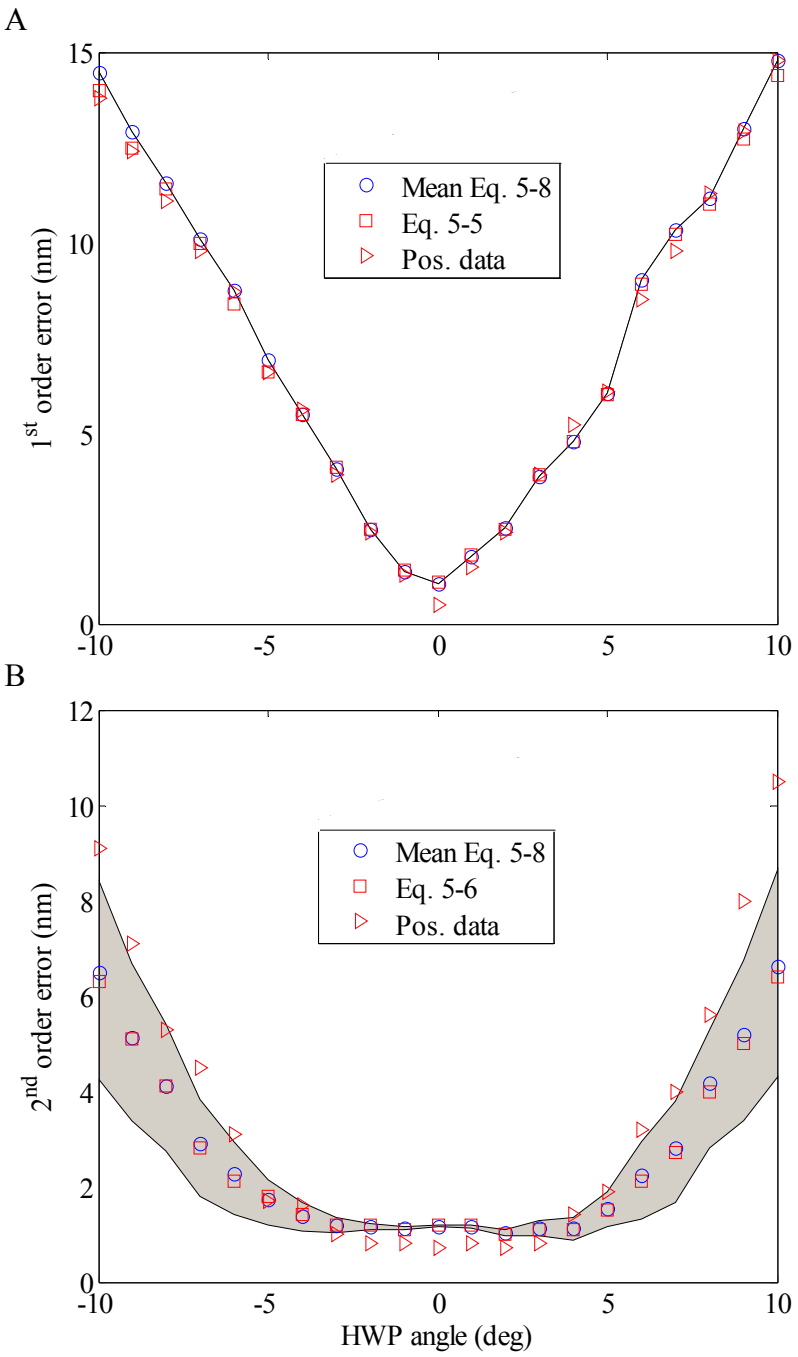

Figure 5-29. Periodic errors calculated by Eqs. 5-5, 5-6, and 5-8 are compared to the position data error magnitudes. The Eq. 5-8 Monte Carlo simulation results include the full distribution of values (indicated by the gray band). A) The magnitude of first order periodic error. B) The magnitude of second order periodic error.

CHAPTER 6
PERIODIC ERROR UNCERTAINTY

Evaluation of the overall uncertainty in displacement measuring interferometry has traditionally followed the "error budget" technique where the individual error contributors are individually determined (either through statistical or other analyses) and then combined, often using a root sum squares, or RSS, approach [3,4]. These contributors, which may include Abbe error, cosine error, deadpath error, environmental error, air (or other medium) turbulence, beam shear, thermal effects, electronics linearity, laser wavelength stability, and periodic error, are tabulated so that primary offenders may be identified and compensated or corrected [83]. This is an effective and time-proven method. However, a single analytical expression that describes displacement, l, in terms of the multiple inputs that determine its value has not been presented. This precludes the use of a Taylor series expansion of the measurand [90, 91] and/or Monte Carlo simulation to evaluate the combined standard uncertainty, $u_c(l)$, for the measurement result.

In this chapter, the analytical periodic error expression presented by Cosijns *et al*. [5] with terms that describe the other error sources listed previously (Chapter 2) is modified to arrive at a single expression for displacement. Uncertainty contributors are then propagated through this equation to determine the combined standard uncertainty, u_c, in the measurement result. The chapter is organized as follows: first, the Cosijns *et al*. expression is presented and example error distributions are shown for various periodic error conditions; second, a single pass, heterodyne interferometer setup, as described in Chapter 4 (the polarization coded interferometer), is used here again and measurement results are provided; and, third, the additional uncertainty

---

Reprinted with permission from Schmitz T, Kim HS. Monte Carlo evaluation of periodic error uncertainty. Precision Engineering 2007; 31(3):251–259.

contributors are appended to the displacement equation and the uncertainty is evaluated using Monte Carlo simulation.

Periodic Error Formulation

As noted, this chapter focuses on traditional heterodyne Michelson-type interferometers with a two frequency laser source. As previously described, this system produces first and second order periodic error by imperfect separation of the two light frequencies into the moving and fixed paths. The two frequencies are typically carried on collinear, mutually orthogonal, linear polarizations, i.e., polarization coded. As described in Chapter 3, unwanted leakage of the reference frequency into the moving path, and vice versa, may occur due to a number of influences, including non-orthogonality between the ideally linear beam polarizations, elliptical polarization of the individual beams, non-ideal performance of the optical components, and/or mechanical misalignment between the interferometer elements (laser, polarizing optics, and targets). The inherent frequency leakage in actual implementations produces an interference signal which leads to periodic error in the measured displacement.

The Cosijns *et al.* [5] analysis propagates: ellipticity of the two (nominally linear) polarizations; non-orthogonality between the two polarizations; rotation of the polarization axes relative to the polarizing beam splitter (which ideally separates the collinear frequencies into the measurement and reference paths); transmission coefficient variations for the polarizing beam splitter; and rotation of the measurement polarizer, which causes interference of the measurement and reference beams, relative to its nominal 45 deg orientation (for vertical and horizontal source polarizations), through the interference equations to arrive at an expression for the periodic phase error, $\Delta\phi_{pe}$. See Eq. 6-1, where θ is the deviation of the polarizer angle from 45 deg and the variables A-F are defined in Eqs. 6-2 through 6-7.

$$\Delta\phi_{pe} = -\tan^{-1}\left(\frac{A + B\sin(2\theta) + C\cos(2\theta)}{D + E\sin(2\theta) + F\cos(2\theta)}\right) \tag{6-1}$$

$$A = (-(\xi^2\sin(\beta)^2+\chi^2\cos(\beta)^2)\cos(d\varepsilon_1/2)\sin(d\varepsilon_2/2)-(\xi^2\cos(\alpha)^2+\chi^2\sin(\alpha)^2)\sin(d\varepsilon_1/2)\cos(d\varepsilon_2/2))\cos(\Delta\phi)+(\xi^2\cos(\alpha)\sin(\beta)+\chi^2\sin(\alpha)\cos(\beta))\cos(d\varepsilon_1/2+ d\varepsilon_2/2)\sin(\Delta\phi) \tag{6-2}$$

$$B = ((\xi^2\sin(\beta)^2-\chi^2\cos(\beta)^2)\cos(d\varepsilon_1/2)\sin(d\varepsilon_2/2)+(\xi^2\cos(\alpha)^2-\chi^2\sin(\alpha)^2)\sin(d\varepsilon_1/2)\cos(d\varepsilon_2/2))\cos(\Delta\phi)+(-\xi^2\cos(\alpha)\sin(\beta)+\chi^2\sin(\alpha)\cos(\beta))\cos(d\varepsilon_1/2+ d\varepsilon_2/2)\sin(\Delta\phi) \tag{6-3}$$

$$C = \xi\chi(\cos(\beta)\sin(\beta)\cos(d\varepsilon_1/2)\sin(d\varepsilon_2/2)(1-\cos(2\Delta\phi))+\sin(\alpha)\sin(\beta)\cos(d\varepsilon_1/2)\cos(d\varepsilon_2/2)\sin(2\Delta\phi)-\cos(\alpha)\cos(\beta)\sin(d\varepsilon_1/2)\sin(d\varepsilon_2/2)\sin(2\Delta\phi)-\sin(\alpha)\cos(\alpha)\sin(d\varepsilon_1/2)\cos(d\varepsilon_2/2)(1+\cos(2\Delta\phi))) \tag{6-4}$$

$$D = ((\xi^2\sin(\beta)^2+\chi^2\cos(\beta)2)\cos(d\varepsilon_1/2)\sin(d\varepsilon_2/2)+(\xi^2\cos(\alpha)^2+\chi^2\sin(\alpha)^2)\sin(d\varepsilon_1/2)\cos(d\varepsilon_2/2))\sin(\Delta\phi)+(\xi^2\cos(\alpha)\sin(\beta)+\chi^2\sin(\alpha)\cos(\beta))\cos(d\varepsilon_1/2+ d\varepsilon_2/2)\cos(\Delta\phi) \tag{6-5}$$

$$E = ((-\xi^2\sin(\beta)^2+\chi^2\cos(\beta)^2)\cos(d\varepsilon_1/2)\sin(d\varepsilon_2/2)+(- \xi^2\cos(\alpha)^2+\chi^2\sin(\alpha)^2)\sin(d\varepsilon_1/2)\cos(d\varepsilon_2/2))\sin(\Delta\phi)+(-\xi^2\cos(\alpha)\sin(\beta)+\chi^2\sin(\alpha)\cos(\beta))\cos(d\varepsilon_1/2+ d\varepsilon_2/2)\cos(\Delta\phi) \tag{6-6}$$

$$F = \xi\chi(\cos(\beta)\sin(\beta)\cos(d\varepsilon_1/2)\sin(d\varepsilon_2/2)\sin(2\Delta\phi)+\cos(\alpha)\cos(\beta)(\cos(d\varepsilon_1/2)\cos(d\varepsilon_2/2)-\sin(d\varepsilon_1/2)\sin(d\varepsilon_2/2)\cos(2\Delta\phi))+\sin(\alpha)\sin(\beta)(-\sin(d\varepsilon_1/2)\sin(d\varepsilon_2/2)+\cos(d\varepsilon_1/2)\cos(d\varepsilon_2/2)\cos(2\Delta\phi))+\sin(\alpha)\cos(\alpha)\sin(d\varepsilon_1/2)\cos(d\varepsilon_2/2)\sin(2\Delta\phi)) \tag{6-7}$$

In these equations, $d\varepsilon_1$ and $d\varepsilon_2$ are the ellipticities of the two collinear beams (ideally zero), α and β are the orientation of the two polarizations relative to the polarizing beam splitter axes (together the two ideally zero angles determine both non-orthogonality between the two polarizations and rotation of the polarization axes relative to the polarizing beam splitter), ξ and χ are the transmission coefficients for the polarizing beam splitter (ideally equal to one), and $\Delta\phi = \frac{4\pi n \cdot \Delta l}{\lambda_{vac}}$ is the phase change introduced by a given displacement, Δl (λ_{vac} is the source vacuum wavelength and n is the refractive index for the propagating medium) for a single pass configuration of the interferometer. The displacement error, Δl_{pe}, due to the periodic phase error is given in Eq. 6-8.

$$\Delta l_{pe} = \frac{\Delta\phi_{pe} \cdot \lambda_{vac}}{4\pi n} \tag{6-8}$$

An example of the variation in periodic error with nominal displacement is provided in Figure 6-1A. The conditions are: $d\varepsilon_1 = d\varepsilon_2 = 0$, $\alpha = -\beta = 2$ deg, $\xi = \chi = 1$, $\theta = 20$ deg, $\lambda_{vac} = 633$ nm, and $n = 1$. It is seen that first order error dominates. This is highlighted by computing the spatial discrete Fourier transform and normalizing the frequency axis to error order. See Figure 6-1B, where the first and second order error amplitudes are 2.95 nm and 0.15 nm, respectively, for the given conditions. The frequency distribution in error values (Figure 6-1C) was determined by Monte Carlo simulation. Because it is equally likely that displacement is recorded at any location along the moving path, Δl is described using a uniform distribution and, in each iteration of the Monte Carlo simulation (100,000 total), is randomly sampled to determine the nominal phase $\Delta\phi$. This value is then used to compute the periodic error using Eqs. 6-1 through 6-8. The strongly non-normal distribution seen in Figure 6-1C is obtained due to the profile slopes around zero values in the sinusoidal error. The standard deviation is 2.09 nm.

A second example is provided in Figure 6-2. In this case, both first and second order error are significant for the conditions: $d\varepsilon_1 = d\varepsilon_2 = 0$, $\alpha = -\beta = 20$ deg, $\xi = \chi = 1$, $\theta = 2$ deg, $\lambda_{vac} = 633$ nm, and $n = 1$. Their amplitudes are 2.56 nm and 6.74 nm, respectively. The distribution is again non-normal, but now contains four peaks rather than two due to the second order error contribution. The standard deviation is 5.12 nm. Many other distributions are possible depending on the frequency mixing conditions.

To determine the periodic error uncertainty, Monte Carlo simulation is used. This approach is applied, rather than the Taylor series expansion method described in references [17, 91], because the periodic error phase in Eq. 6-1 is identically zero for ideal values of the input variables. Selection of ideal mean values presumes that all misalignments/imperfections have

been corrected to within the uncertainty limits (i.e., all known biases have been removed to within the applicable limits).

For demonstration purposes, standard uncertainties of $u(d\varepsilon_1)$ = 0.1 deg, $u(d\varepsilon_2)$ = 0.1 deg, $u(\alpha)$ = 2 deg, and $u(\theta)$ = 2 deg were selected. Normal distributions were assumed in all cases. The corresponding mean values were $d\varepsilon_1 = d\varepsilon_2 = 0$ deg, $\alpha = \beta = 0$ deg, and $\theta = 0$ deg. The transmission coefficients, ξ and χ, are bounded by a maximum value of 1. Therefore, a uniform distribution with a range of ±0.05 was selected about a mean value of 0.95 for each[1]. Uncertainties in λ and n were not considered at this stage; these are treated in the section that evaluates the combined standard uncertainty in displacement where the remaining uncertainty contributors are added. Finally, λ_{vac} = 633 nm and n = 1 were used and a uniform distribution for Δl with a range from zero to λ was again applied. Results are provided in Figure 6-3, which shows the distribution of Δl_{pe} values for the selected input uncertainties. The mean value is zero and the standard deviation is 1.77 nm (100,000 iterations). The reader may note that the distribution is non-normal, with a higher likelihood of obtaining zero error than a normal distribution would suggest.

As an exercise, the products of the sensitivities, $\frac{\partial \Delta l_{pe}}{\partial x}$, and standard uncertainties, $u(x)$, for each input x were calculated; see Table 6-1. The individual contributors were isolated by setting all uncertainties except the term in question equal to zero. Presumably, this would enable the individual contributors to be compared, similar to the error budget and analytical Taylor series approaches. However, as seen in the table, the apparent individual contributions for ξ, χ, and θ are zero. This is clearly not the case. Rather, these terms are only zero for ideal mean

[1] The standard deviation for this case is 0.05/√3 [91].

values and no variation in all other inputs. For any other case, their contributions are non-zero. This emphasizes the utility of using the Monte Carlo technique to simultaneously consider all uncertainties for this evaluation.

Table 6-1. Apparent individual uncertainty contributors for Δl_{pe}

x	$\bar{x}$	$u(x)$	$\frac{\partial \Delta l_{pe}}{\partial x} u(x)$ (nm)
$d\varepsilon_1$	0	0.1 deg	0.03
$d\varepsilon_2$	0	0.1 deg	0.03
α	0	2 deg	1.25
β	0	2 deg	1.25
ξ	0.95[2]	$\frac{0.05}{\sqrt{3}}$	0
χ	0.95[3]	$\frac{0.05}{\sqrt{3}}$	0
θ	0	2 deg	0

Periodic Error Measurements

Experimental data were collected using the setup shown in Figure 4-1 in Chapter 4 to show the various periodic error levels depending upon the angular misalignment of the linear polarizer and half wave plate. Example comparisons between measurement results and the Cosijns *et al.* model are provided in Figures 6-4 and 6-5. For Figure 6-4, the polarizer was rotated 39 deg from its nominal 45 deg orientation in order to provide a scenario with significant first order error. The other model parameters were: $n = 1$, $\lambda_{vac} = 633$ nm, $d\varepsilon_1 = d\varepsilon_2 = 0$ deg, $\alpha = -\beta = 1.5$ deg, and $\xi = \chi = 1$. In Figure 6-5, the half wave plate was adjusted 10 deg from its nominal orientation (fast axis vertical). In this case, both first and second order errors were present. The model parameters were: $n = 1$, $\lambda_{vac} = 633$ nm, $d\varepsilon_1 = d\varepsilon_2 = 0$ deg, $\alpha = -\beta = 20$ deg (a 1 deg rotation of the half wave plate gives a 2 deg change in the linear polarization angle), $\theta = 2$ deg, and $\xi = \chi = 1$. Good

[2] The mean value was set equal to 1 when evaluating other inputs.

agreement is seen. In both cases, the phase measuring electronics used a sampling frequency of 312.5 kHz. Also, the displacement measuring resolution was 0.3 nm for the single pass interferometer configuration implemented here.

To evaluate the Monte Carlo approach to periodic error uncertainty evaluation, two sets of measurements were performed. First, the polarizer angle was varied from -41 deg to +37 deg about the nominal value and the first and second order errors identified using the Fourier transform approach described previously. Second, the half wave plate angle was varied from -16 deg to +14 deg about its nominal value and the periodic error determined. These measurement results were compared to model predictions using nominal input values: 1) Figure 6-6 shows results for the polarizer tests with $n = 1$, $\lambda_{vac} = 633$ nm, $d\varepsilon_1 = d\varepsilon_2 = 0$ deg, $\alpha = -\beta = 1.5$ deg, $\theta = -41$ deg to +37 deg, and $\xi = \chi = 1$; and 2) Figure 6-7 displays the half wave plate results with $n = 1$, $\lambda_{vac} = 633$ nm, $d\varepsilon_1 = d\varepsilon_2 = 0$ deg, $\alpha = -\beta = -32$ deg to +28 deg, $\theta = 2$ deg, and $\xi = \chi = 1$. These figures also show mean values from Monte Carlo simulations, where the Monte Carlo results include one standard deviation (1σ) error bars. In Figure 6-6A, good agreement is seen. Additionally, for polarizer angles near the nominal value (axis value of zero) it is observed that the Monte Carlo means are larger than the model values. This trend matches the experimental results. In Figure 6-6B, reasonable agreement is observed, but the measured errors lie outside the 1σ error bars for small angles. These error levels approach the resolution limit (0.3 nm), which was not considered as an uncertainty contributor at this stage. In Figure 6-7A, the larger Monte Carlo mean errors near the nominal half wave plate angle again more closely agree with experiment than the model values determined from mean inputs. In Figure 6-7B, although the general trends agree, the experimental errors generally fall outside the Monte Carlo error bars. This could be the result of incorrect estimates of the mean input values.

The Monte Carlo simulations for first and second order uncertainty evaluation required the following steps: 1) sample the input values for $d\varepsilon_1$, $d\varepsilon_2$, α, β, θ, ξ, and χ from the predefined distributions (see Table 6-2); 2) calculate the periodic error profile using the Cosijns *et al*. model; 3) identify the first and second order periodic error amplitudes using the Fourier transform approach; and 4) record the results for each simulation iteration. The mean values and standard deviations from all iterations (10,000) were then taken to represent the best estimates of the first and second order error expectation values and standard uncertainties, respectively.

Table 6-2. Monte Carlo simulation input values for first and second order error uncertainty evaluation (all distributions were normal except for ξ and χ which were uniform).

Polarizer tests			Half wave plate tests	
x	$\bar{x}$	$u(x)$	$\bar{x}$	$u(x)$
$d\varepsilon_1$	0	0.1 deg	0	0.1 deg
$d\varepsilon_2$	0	0.1 deg	0	0.1 deg
α	1.5 deg	1 deg	-32 to +28 deg	1 deg
β	-1.5 deg	1 deg	+32 to -28 deg	1 deg
ξ	0.95	$\frac{0.05}{\sqrt{3}}$	0.95	$\frac{0.05}{\sqrt{3}}$
χ	0.95	$\frac{0.05}{\sqrt{3}}$	0.95	$\frac{0.05}{\sqrt{3}}$
θ	-41 to +37 deg	1 deg	2 deg	1 deg

Displacement Combined Standard Uncertainty

In this section, the additional displacement uncertainty contributors described in Chapter 2 are reviewed and the analytical displacement equation is provided.

Abbe Error

The potential for Abbe error exists whenever the measurement beam is not collinear with the motion axis (assume they are parallel here). The relationship between the true, l, and measured, l_m, displacement is $l = l_m - d_{\text{offset}} \tan(\psi)$, where d_{offset} is the Abbe offset between the

measurement beam and motion axis and ψ is uncompensated rotation about a line normal to the plane containing both the measurement beam and motion axis.

Cosine Error

Cosine error is inherent to displacement measurement interferometry because the beam and motion axis cannot be perfectly aligned (i.e., some uncertainty always remains). The corresponding true/measured displacement relationship is $l = l_m \sec(\gamma)$, where γ is the positive angular misalignment. The reader may note that, for any value of γ, the measured displacement is smaller than the true displacement (i.e., a bias is introduced). The reported value, l_r, can be corrected for the bias using $l_r = \bar{l}_m\left(1 + u^2(\gamma)\right)$, where $\bar{l}_m$ is the expectation value of l_m and $u^2(\gamma)$ is the variance of γ [17].

Deadpath Error

Deadpath error occurs when the path lengths from the polarizing beam splitter to the fixed and moving targets are unequal at initialization and there is an uncompensated change in the refractive index, Δn, of the propagating medium (air is considered here) during the measurement. The true/measured displacement relationship is $l = l_m - \Delta n \cdot DP$, where DP is the deadpath, or difference between the path lengths. The value of the refractive index for air may be expressed as a function of absolute temperature, T (K), pressure, P (Pa), percent relative humidity, RH, and carbon dioxide content, CO_2 (ppm) as shown in Eq. 6-9 [18]. An evaluation of this equation at conditions of standard temperature and pressure (20 deg C and 101323.2 Pa) with 50% RH and an assumed CO_2 level of 355 ppm yields an air index value of 1.0002713.

$$n = 1 + 271.8 \times 10^{-6} \frac{P}{101325} \frac{293.15}{T}\left(1 + 0.54\left(\frac{CO_2 - 300}{1 \times 10^{-6}}\right)\right) - 1 \times 10^{-8} RH \tag{6-9}$$

The reader may note that Eq. 6-9 does not implicitly consider air turbulence, which affects index through localized time-dependent fluctuations in temperature and pressure [15, 23]. This could be incorporated, however, by adding noise (in addition to the variations caused by uncertainties in the temperature, pressure, and relative humidity transducers) to the index values within the Monte Carlo simulation.

Atmospheric Error

This error occurs when there is an uncompensated change in index during a measurement. The error relationship is $l = l_m - \Delta n \cdot PD$, where *PD* is the physical displacement of the moving retroreflector after initialization. Resolution limits in the displacement measurement system can be conveniently included as perturbations in *PD*.

Material Thermal Expansion Error

Changes in temperature, and the associated thermal deformations, can lead to errors associated with the interferometer optics. The corresponding relationship is $l = l_m - \Delta T \cdot C_{th}$, where ΔT is the change in temperature and C_{th} is a constant typically supplied by the interferometer manufacturer.

Other Phase Errors

In addition to periodic error, nonlinearities can also be introduced by the phase measuring electronics, $\Delta\phi_{elect}$ [12, 24]. Also, a change in overlap between the reference and measurement beams, or beam shear, during a measurement can lead to errors due to the imperfect, non-planar wavefronts, $\Delta\phi_{shear}$.

Laser Wavelength Stability

Variation in the source wavelength during a measurement naturally leads to errors. The level of variation is typically small and provided by the laser manufacturer.

The final displacement relationship is provided in Eq. 6-10. This equation considers periodic error as well as the terms identified in the previous sections. To demonstrate the application of Eq. 6-10, a Monte Carlo simulation is completed to evaluate $u_c(l)$ for a range of displacements. The inputs are provided in Table 6-3 and the simulation results are shown in Figure 6-8.

$$l = \frac{\left(\Delta\phi + \Delta\phi_{pe} + \Delta\phi_{elect} + \Delta\phi_{shear}\right)\lambda_{vac}}{4\pi n}\sec\left(\gamma\right) - d_{\text{offset}} \cdot \tan\left(\psi\right) - \Delta n \cdot DP - \Delta n \cdot PD - \Delta T \cdot C \tag{6-10}$$

Figure 6-8A shows both the difference between the Eq. 6-10 mean value and nominal displacement, l_0, and the 1σ error bars (100,000 iterations). As expected, the uncertainty increases substantially over the 1 mm to 1000 mm interval. It is also seen that the mean displacement from Eq. 6-10 is consistently smaller than the nominal value. This is caused by the single-sided cosine error distribution (note that the bias is present even though the mean value of γ is zero). Figure 6-8B highlights this bias (squares) and also shows the bias removal using $l_r = \bar{l}_m\left(1 + 0.5u^2\left(\gamma\right)\right)$ (circles).

Table 6-3. Monte Carlo simulation input values for $u_c(l)$ evaluation.

x	$\bar{x}$	$u(x)$	Distribution type
$d\varepsilon_1$	0	0.1 deg	Normal
$d\varepsilon_2$	0	0.1 deg	Normal
α	1 deg	1 deg	Normal
β	-2 deg	1 deg	Normal
ξ	0.95	$\frac{0.05}{\sqrt{3}}$	Uniform
χ	0.95	$\frac{0.05}{\sqrt{3}}$	Uniform
θ	2 deg	1 deg	Normal
$\Delta\phi_{elect}$	0	0	-
$\Delta\phi_{shear}$	0	0	-
λ_{vac}	633 nm	$6\text{x}10^{-6}$ nm	Normal

Table 6-3. Continued

P	101323.2 Pa	$\frac{50}{\sqrt{3}}$ Pa	Uniform
T	20 deg C	$\frac{0.2}{\sqrt{3}}$ deg C	Uniform
RH	50%	$\frac{2}{\sqrt{3}}$ %	Uniform
CO_2	355 ppm	0 ppm	-
AO	0 mm	1 mm	Normal
DP	50 mm	1 mm	Normal
PD	1 to 1000 mm	$\frac{0.3}{\sqrt{3}}$ nm*	Uniform
C_{th}	25 nm/deg C	1 nm/deg C	Normal
γ	0	0.03 deg	Normal
ψ	100 μrad	10 μrad	Normal

*This uncertainty represents the resolution of the interferometer, which depends on the phase measuring electronics and optical configuration.

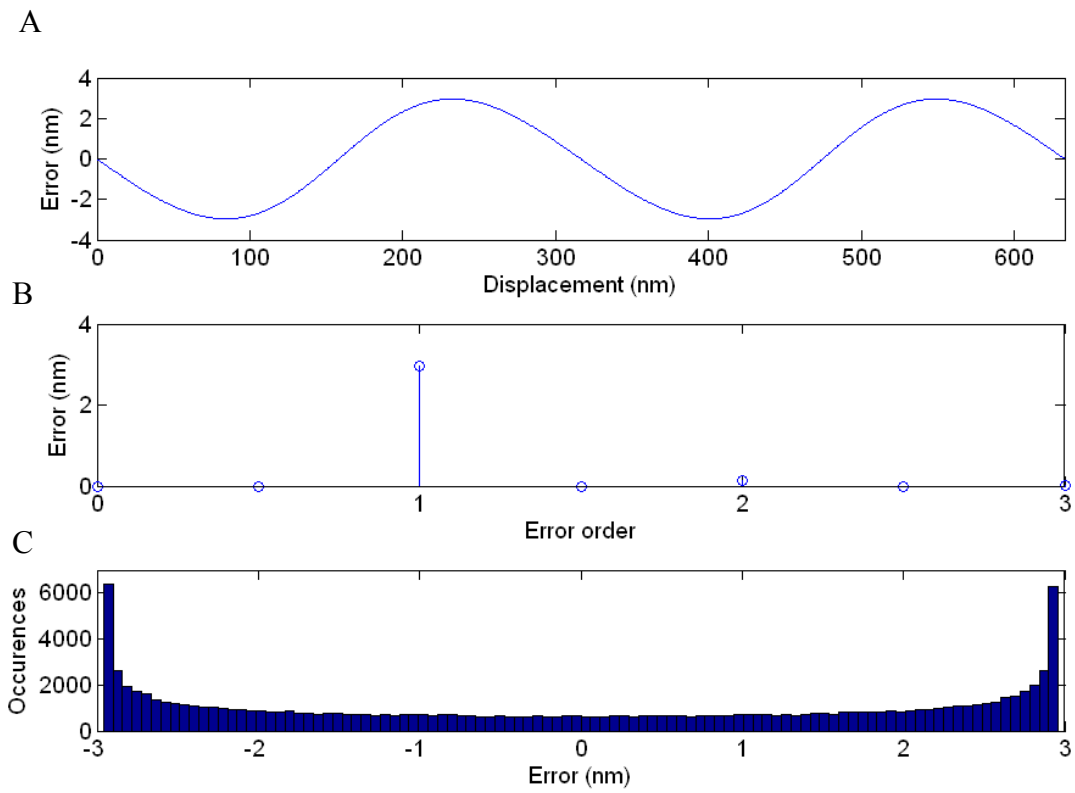

Figure 6-1. An example of periodic error variation with conditions that dominates first error order. A) Periodic error as a function of nominal displacement for $d\varepsilon_1 = d\varepsilon_2 = 0$, $\alpha = -\beta = 2$ deg, $\xi = \chi = 1$, $\theta = 20$ deg, $\lambda_{vac} = 633$ nm, and $n = 1$. B) Spatial Fourier transform of periodic error with the frequency axis normalized to error order (i.e., 1 represents first order error). C) Distribution of periodic error.

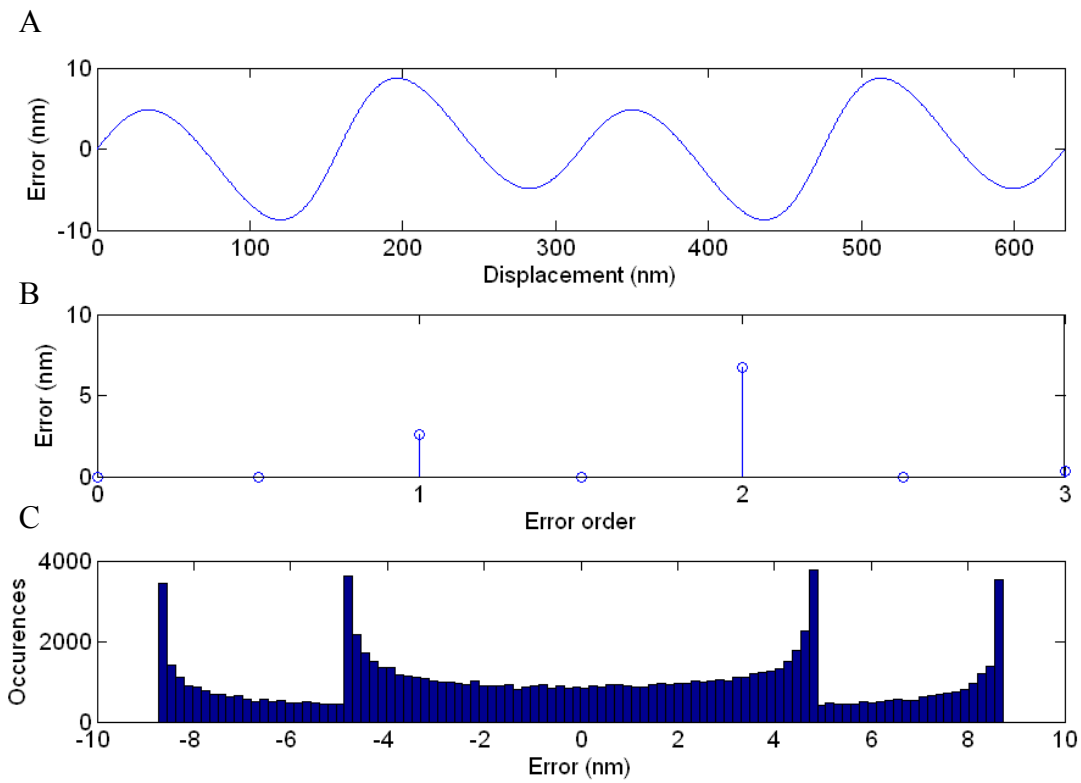

Figure 6-2. An example of periodic error variation with conditions that dominates both first and second error orders. A) Periodic error for $d\varepsilon_1 = d\varepsilon_2 = 0$, $\alpha = -\beta = 20$ deg, $\xi = \chi = 1$, $\theta = 2$ deg, $\lambda_{vac} = 633$ nm, and $n = 1$. B) Spatial Fourier transform of periodic error. C) Distribution of periodic error.

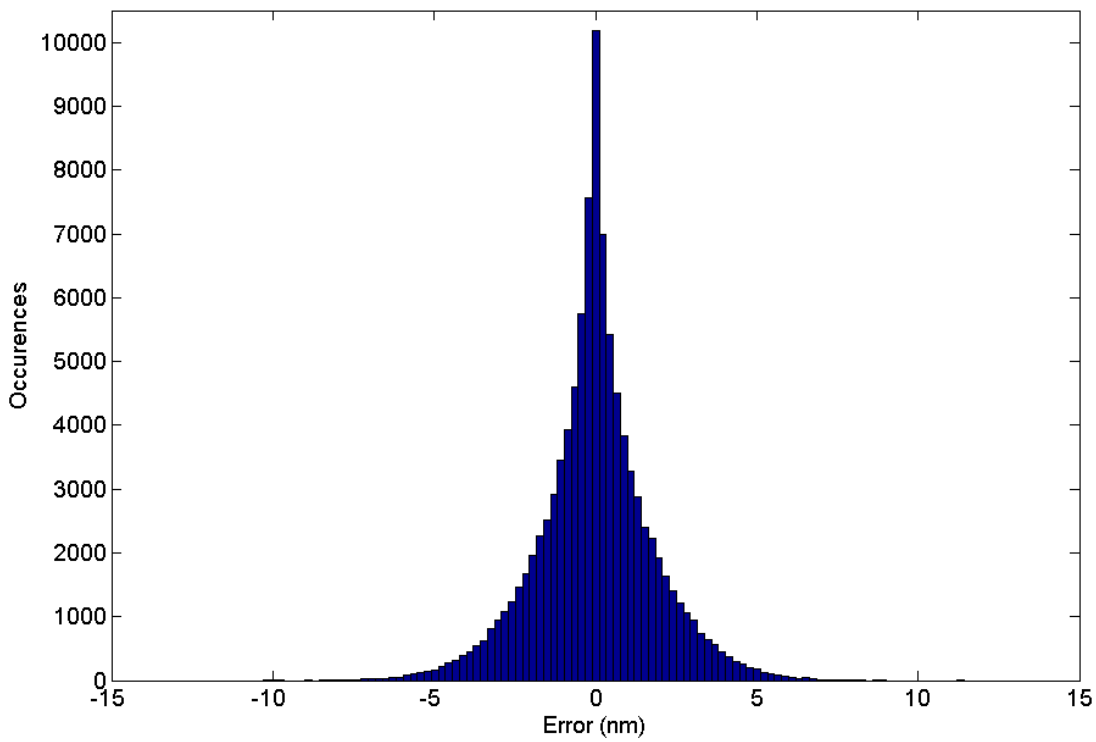

Figure 6-3. Histogram of Δl_{pe} values for normal distributions of $d\varepsilon_1$, $d\varepsilon_2$, α, β, and θ with u$(d\varepsilon_1)$ = $u(d\varepsilon_2)$ = 0.1 deg, $u(\alpha) = u(\beta) = u(\theta)$ = 2 deg and zero mean values; and uniform distributions of ξ and χ with ranges of ±0.05 and mean values of 0.95.

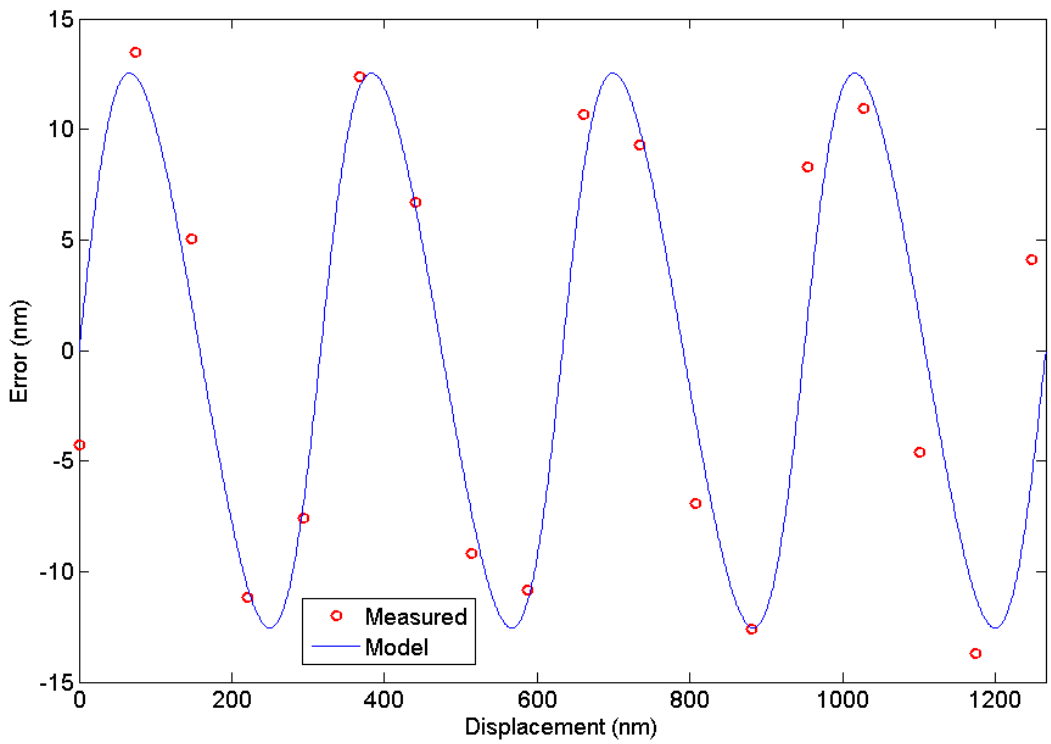

Figure 6-4. Measurement/model comparison for 39 deg polarizer misalignment – first order error dominates. Other model parameters were: $n = 1$, $\lambda_{vac} = 633$ nm, $d\varepsilon_1 = d\varepsilon_2 = 0$ deg, $\alpha = -\beta = 1.5$ deg, and $\xi = \chi = 1$.

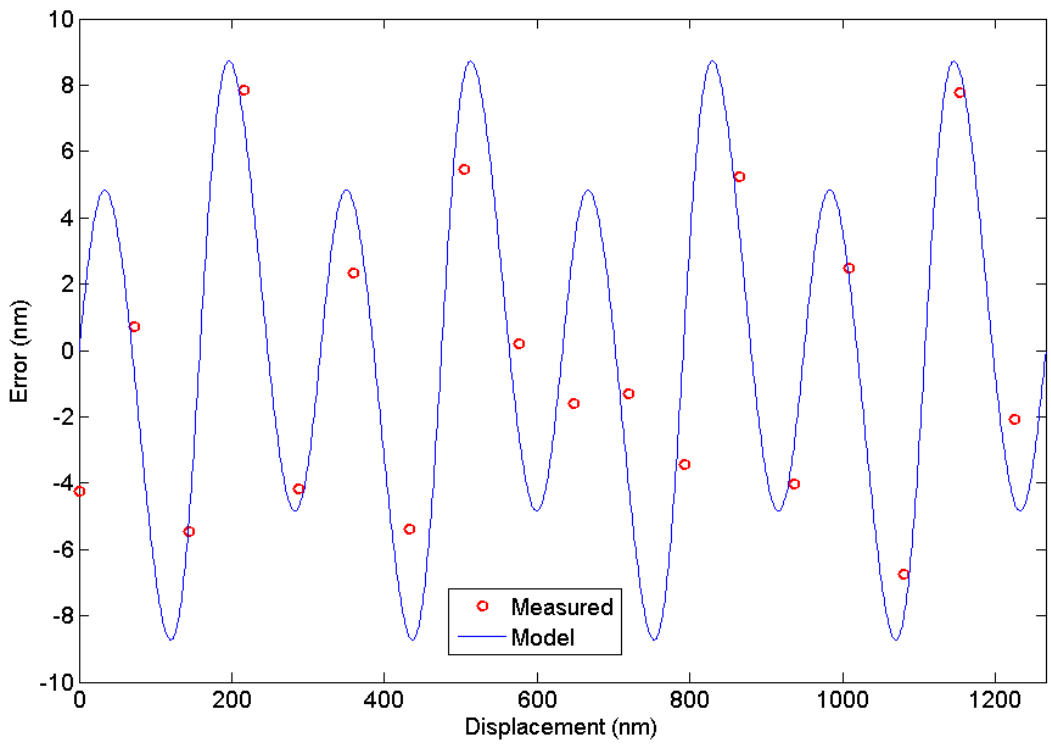

Figure 6-5. Measurement/model comparison for 10 deg half wave plate misalignment – first and second order errors are present. Model parameters were: $n = 1$, $\lambda_{vac} = 633$ nm, $d\varepsilon_1 = d\varepsilon_2 = 0$ deg, $\alpha = -\beta = 20$ deg, $\theta = 2$ deg, and $\xi = \chi = 1$.

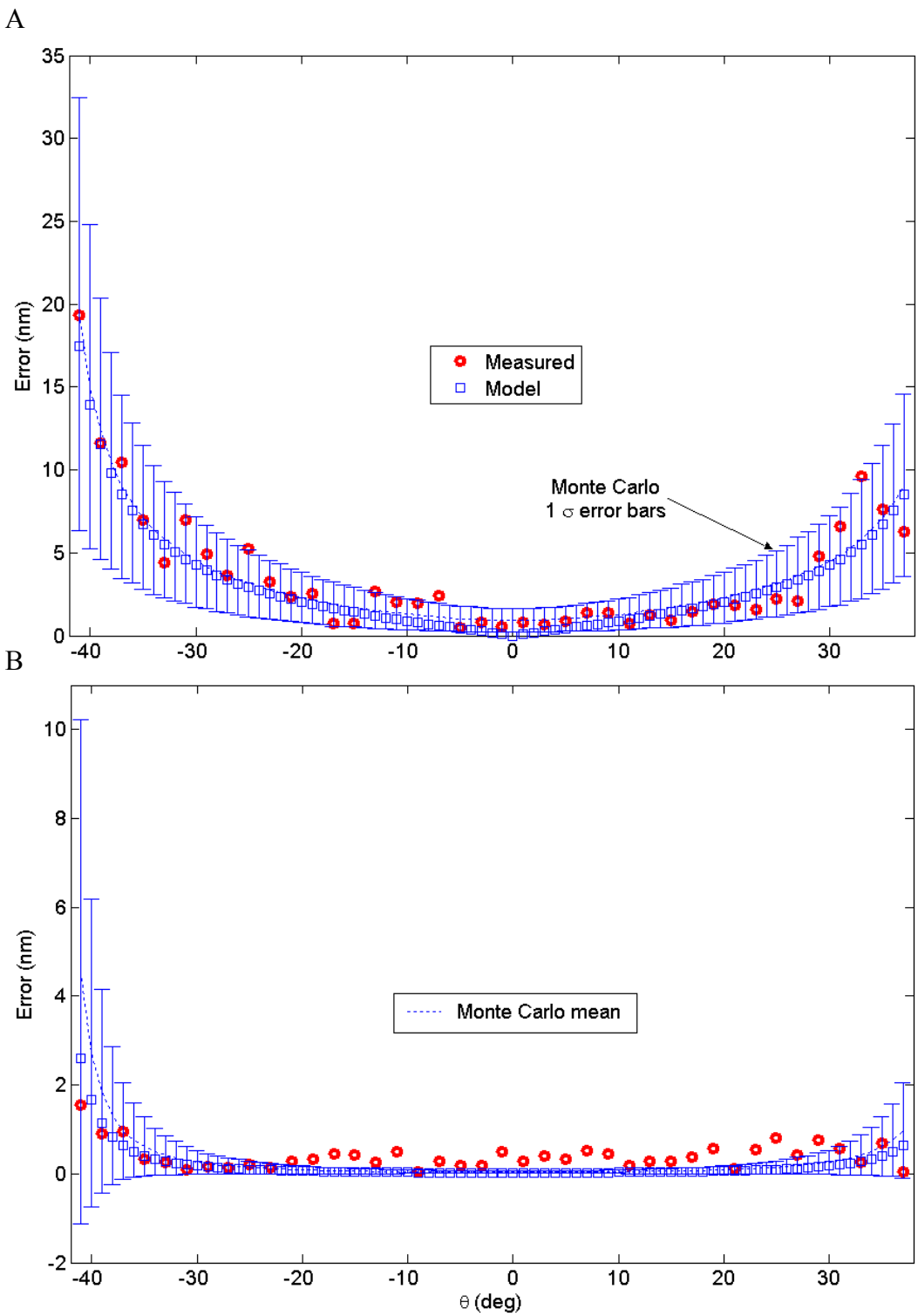

Figure 6-6. Comparisons between measurements (circles), model (squares), and Monte Carlo simulation (dotted line) for variable polarizer angle tests. A) First order errors. B) Second order errors.

A

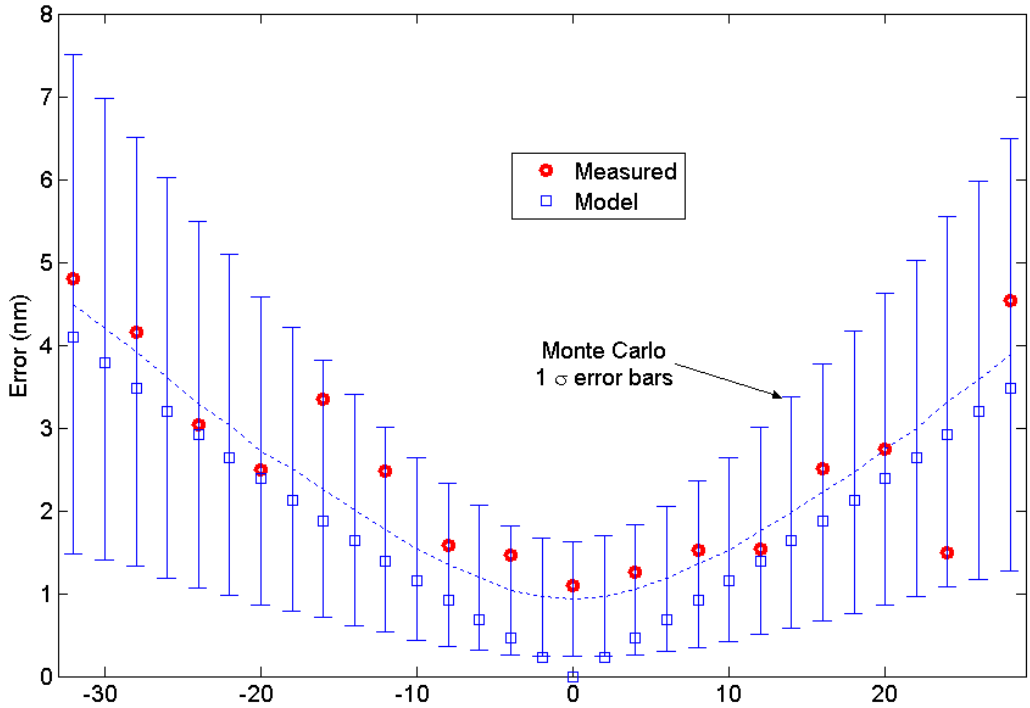

B

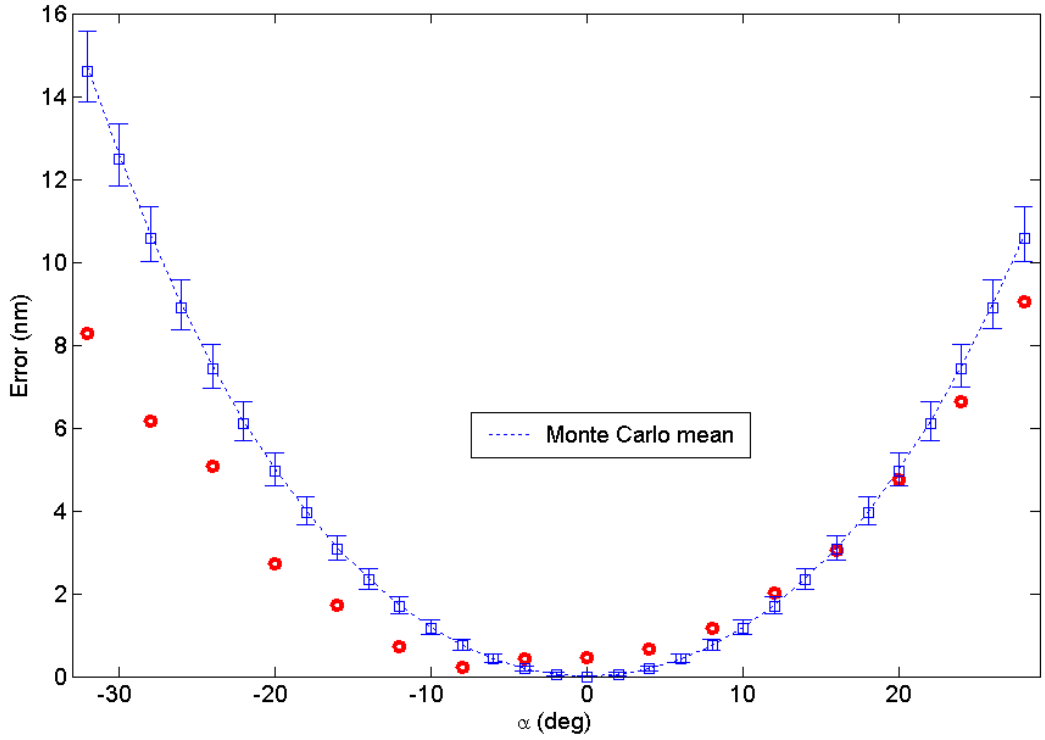

Figure 6-7. Comparisons between measurements (circles), model (squares), and Monte Carlo simulation (dotted line) for variable half wave plate angle tests. A) First order errors. B) Second order errors.

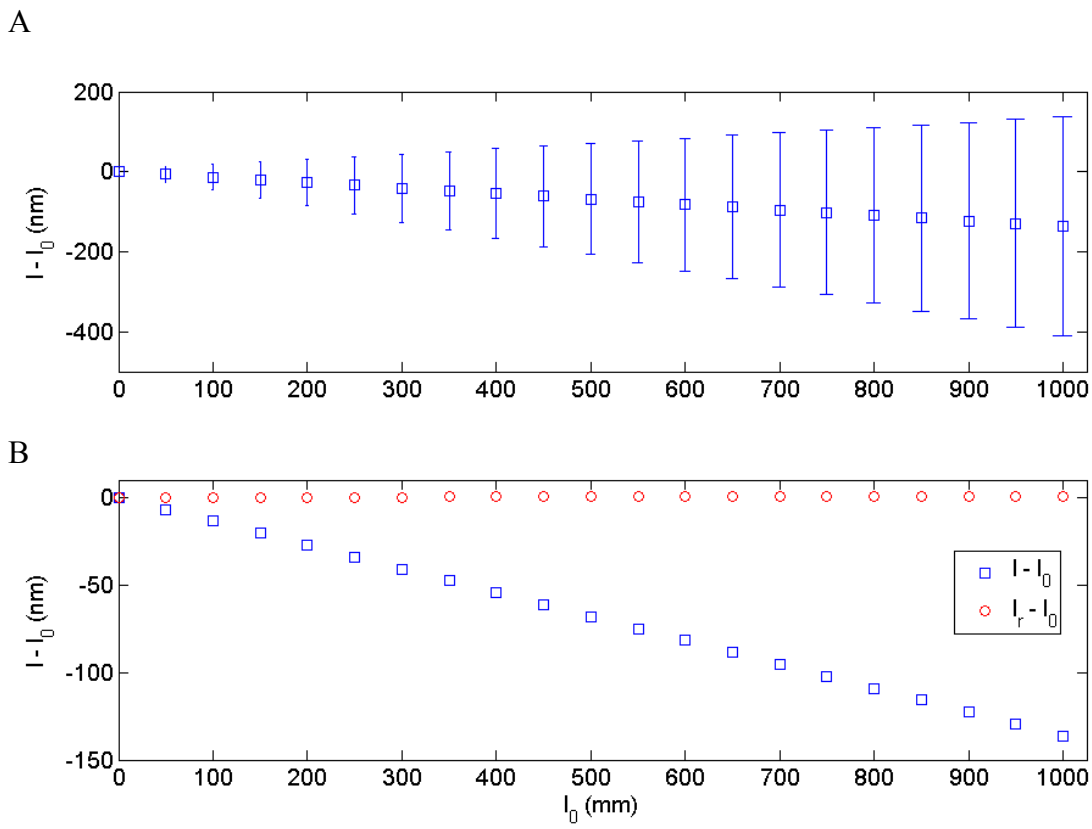

Figure 6-8. Monte Carlo simulation results for Eq. 6-10 using the data in Table 6-3. A) Difference between mean Eq. 6-10 values and nominal displacement with 1σ error bars. B) Uncorrected (squares) and corrected (circles) difference.

CHAPTER 7
NEW HETERODYNE INTERFEROMETER DESIGN

The presence of periodic error in a traditional heterodyne interferometer system that uses polarization dependent optics to separate orthogonal and linearly polarized beams was shown in Chapter 4. Although numerous studies have been completed to correct/compensate for periodic error, it remains an inherent error source due to the potential for frequency mixing. In this chapter, a new heterodyne interferometer design is described that eliminates periodic error. The setup and results for the new acousto-optic modulator-based displacement measuring interferometer (AOM DMI) design are detailed. The absence of periodic error is demonstrated in the frequency domain.

Acousto-Optic Modulator

In the AOM DMI design, a pair of AOMs is used to generate, and keep spatially separate, the heterodyne frequencies. The basic elements of an AOM are a glass body with a piezoelectric transducer (PZT) attached at one end and a frequency source (stable quartz oscillator) to drive the PZT [92]. Actuation of the PZT at the oscillator driving frequency generates acoustic waves within the glass which leads to periodic spatial variations in the glass refractive index due to the changes in density (i.e., a moving diffraction grating is produced). When laser light is incident on the moving diffraction grating, it is diffracted into multiple separate beams (or orders). The diffraction angle, γ, is given by Eq. 7-1, where $m = 0, \pm1, \pm2, \ldots$ is the order number and υ is the acoustic wavelength. Under high driving frequencies and by proper design, a portion of the light is diffracted into the 1st order ($m = 1$) beam while the rest (0th order beam) passes through the glass; see Figure 7-1. The amplitude of the acoustic waves within the glass determines the

---

Reprinted with permission from Kim H, Schmitz T, Beckwith J. Periodic error in heterodyne interferometry: Examination and Elimination. In: Halsey D, Raynor W, ed. Handbook of Interferometers: Research, Technology and Applications. Hauppauge, NY: Nova Science; 2009.

amount of light diffracted into the 1st order beam. Adjusting the power level of the PZT driver can therefore be used to balance the intensity between the two beams.

$$\sin\gamma = \frac{m\lambda}{2\upsilon} \tag{7-1}$$

The diffracted wave can be considered to originate from the moving diffraction grating. Since the motion of a source causes a Doppler shift, the frequency of the diffracted wave is shifted from the incident light frequency. The Doppler shifted frequency due to the moving diffraction grating, $f_{d,sound}$, is the ratio of the velocity, v, and the wavelength, υ, of the sound wave, $f_{d,sound} = v/\upsilon$ so that the Doppler frequency is equivalent to the oscillator driving frequency. When the incident light encounters an approaching acoustic wave, the frequency of the diffracted beam, f_{dif}, is up-shifted as shown in Figure 7-2A, and when it encounters a receding wave, the frequency of the diffracted beam is down-shifted as shown in Figure 7-2B. The frequency of the diffracted wave for each order can be identified by Eqs. 7-2 (approaching) and 7-3 (receding).

$$f_{dif} = f_0 + mf_{d,sound} \tag{7-2}$$

$$f_{dif} = f_0 - mf_{d,sound} \tag{7-3}$$

New Interferometer Configuration

A photograph and schematic diagram of the new AOM DMI setup are provided in Figure 7-3. There were three fundamental requirements for the AOM DMI design: 1) frequency mixing was to be eliminated by keeping the two frequencies spatially separate; 2) both measurement and reference signals needed to be generated; and 3) optical feedback into the laser cavity had to be avoided. Additionally, it was preferred that the beat frequency be adjustable. The solution to these requirements is described in the following paragraphs.

With reference to Figure 7-3B, a single frequency laser is used as the light source rather than the two frequency source applied in polarization dependent configurations. The beam passes through a half wave plate and is incident on the first acousto-optic modulator (AOM1). Setting the angle of AOM1 (f_1 driving frequency) to the incident beam as specified in Eq. 7-1 produces the 0th order and 1st order beams. The frequency of the 0th order beam is simply the optical frequency, f_0, while the 1st order beam frequency is $f_0 + f_1$. The 0th order beam continues toward the second acousto-optic modulator (AOM2), which is driven at the frequency f_2, while the 1st order beam is directed toward the fixed retroreflector (RR) for the measurement signal and one of the two retroreflectors for the reference signal. The 0th order beam from AOM1 passes through AOM2. The 1st order (diffracted) beam from AOM2 with a frequency of $f_0 + f_2$ is directed toward the moving retroreflector and the second retroreflector for the reference signal. The undiffracted beam is not used. Both the 1st order beams from AOM1 and AOM2 are retroreflected and recombined at AOM1 (i.e., it functions essentially as a beamsplitter). The reference interference signal (Ref) is produced after passing through a linear polarizer oriented at 45 deg with respect to the vertical axis. It is the solid line in Figure 7-3B and has a beat frequency equal to two times the difference between the two AOM (user selected) driving frequencies as shown in Eq. 7-4. The measurement interference signal (Meas) is produced using the same linear polarizer. It is the dashed line in Figure 7-3B and is Doppler shifted by, f_d (due to the target motion) from the beat frequency as shown in Eq. 7-5. In both cases, the beat frequency is determined as the difference between the frequencies of the two interfered beams; the signals are collected using two photodetectors with fiber-optic pickups. The reader may note that the angle of the 1st order diffracted beam in Figure 7-3B is exaggerated. Sufficient distance is needed

for the beams from the AOMs to be separated and directed onto each retroreflector due to the small diffraction angle from the AOMs.

$$\begin{array}{l} f_0 + f_1 \\ \underline{f_0 + 2f_2 - f_1} \\ \text{Ref} = 2\left(f_2 - f_1\right) \end{array} \tag{7-4}$$

$$\begin{array}{l} f_0 + f_1 \\ \underline{f_0 + 2f_2 - f_1 \pm f_d} \\ \text{Meas} = 2\left(f_2 - f_1\right) \pm f_d \end{array} \tag{7-5}$$

Periodic Error Elimination

In this section, the frequency content of interference signals from the AOM DMI (collected using a spectrum analyzer) is presented. The undesired interference terms, which cause periodic error, are not observed in the spectrum. Data was collected while the target displaced in the $+x$ direction (see Figure 7-3A). The beat frequency, $\Delta f = 2\left(f_2 - f_1\right)$, for the first alignment was 3.64 MHz; it was obtained by setting f_1 to 40 MHz and f_2 to 41.82 MHz. Figures 7-4A and 7-4B show the frequency content for velocities of 5,000 mm/min and 10,000 mm/min. The corresponding Doppler shifts (up-shifted) are 0.26 MHz and 0.53 MHz, respectively. It is seen that only the desired *ac interference* signal, 3.64 + 0.26/0.53 MHz, and *dc power* peaks are present with no content at the *ac reference* signal (first order periodic error) frequency of 3.64 MHz or the leakage induced *ac interference* signal (second order periodic error) frequency of 3.64 – 0.26/0.53 MHz.

In Figure 7-5, spectra for a single target velocity (10,000 mm/min) for various: A) linear polarizer angles; and B) half wave plate angles are shown. Again, unwanted interference signals

are not present for any angular orientation. This result indicates that the new interferometer does not depend on polarization of the laser source. The test results of the polarization coded displacement measuring interferometer (see Figure 4-1A) for the same test conditions are provided in Figure 7-6 for comparison purposes. It is seen that both first and second order periodic error are present in both cases.

One of the advantages of the new interferometer design is the ability to tune the beat frequency by adjusting the driving frequencies of the two acousto-optic modulators. This makes the new design compatible with existing phase measuring hardware/software independent of the system specific beat frequency (common commercial options are 3.65 MHz and 20 MHz). To demonstrate the variable beat frequency capability, the driving frequency for AOM2 was modified to f_2 = 42.5 MHz, while f_1 was maintained at 40 MHz. This gave a new beat frequency of Δf = 5 MHz. Figure 7-7 shows the spectra for this new configuration at target velocities of A) 5,000 mm/min; and B) 10,000 mm/min. No periodic error content is observed.

Size Reduction

Although the elimination of frequency leakage-induced periodic error was successfully demonstrated for the AOM DMI, the size of the new design is too large for practical application. Reducing the setup footprint is necessary.

The size of the AOM-DMI is enlarged by the small beam separation from the first AOM (AOM1) in the setup. As discussed, the diffracted beam angle is proportional to the wavelength of the incident beam (633 nm for He-Ne laser) and inversely proportional to the wavelength of acoustic wave propagating in the glass body for an AOM. The diffraction angle of the first order beam in the setup is 7 mrad (0.4 deg). Therefore, a significant distance (1500 mm) is needed

between the first AOM and second AOM (AOM2) to direct the first diffracted and undiffracted beams into the reference and measurement retroreflectors, respectively. See Figure 7-8.

A photograph and schematic diagram of the reduced size AOM DMI setup are provided in Figure 7-9. In Figure 7-9B, a single frequency stabilized He-Ne laser is again used as the light source. The output beam of the He-Ne laser is collimated and passes through the first acousto-optic modulator (AOM1), oriented at the Bragg angle, which produces the 0th order and 1st order (diffracted) beams. The right angle prism with hole is inserted at the shortest distance from AOM1 where the 0th and 1st order beams are visually separated. The 1st order beam is directed toward the fixed retroreflector for the measurement signal and one of the two (fixed) retroreflectors for the reference signal (Ref. RR1) by reflecting at the prism surface, while the 0th order beam continues toward the second acousto-optic modulator (AOM2) by passing beside the prism. The 1st order (diffracted) beam from AOM2 is directed toward the moving target retroreflector and second retroreflector for the reference signal (Ref. RR2). The retroreflected beam from Ref. RR2 returns to AOM2 and passes through the hole of the right angle prism to recombine and interfere at AOM1 with the reflected beam from the Ref. RR1. The frequency of the reference signal is two times the frequency difference between the two AOMs driving frequencies. The retroreflected beams from both fixed and moving retroreflectors are also recombined at AOM1 to serve as the measurement signal. The frequency of the measurement signal is the same as the reference signal for no target motion, but up or down-shifted by the Doppler frequency during target motion (depending on direction). Finally, both the measurement and reference signals are passed to the photodetectors using multi-mode fiber optics. With the new setup (1400 mm (L) x 620 mm (W)), approximately a 65% area reduction from the original setup (2240 mm (L) x 1100 mm (W)) is achieved.

As noted, in the new setup design, a right angle prism with a hole is used to reduce the size relative to the initial setup. Figure 7-10 shows the prism with dimensions of 15 mm × 15 mm × 21.2 mm (A × B × C). The prism material is BK7 glass with an enhanced aluminum coating on the hypotenuse. To fabricate the required hole through the prism center, an electroplated diamond core drill was used. Figures 7-11A and 7-11B show the diamond core drill and its surface, respectively. The diameter of the beam passing through the prism is approximately 2 mm so that a 4.8 mm (3/16") hole provided sufficient clearance. Figure 7-12 shows the drilling operation setup, where the right angle prism was submerged in the water to reduce heating. The drilling was operated at a feedrate of 0.23 mm/min. The prism after drilling is shown in Figure 7-13.

As comparison, Table 7-1 lists the optical components and approximate costs for both the traditional interferometer and the AOM DMI. The main components that differentiate the two interferometers are the laser, polarizing beam splitter, and acousto-optic modulator. In traditional interferometers, overlapping beams that are generated within a two-frequency He-Ne laser head are separated by a polarizing beam splitter, while two acousto-optic modulators are used to separate beams from a single frequency stabilized He-Ne laser in the AOM DMI. The total costs are similar, but the AOM DMI offers improved accuracy by eliminating periodic error.

Table 7-1. Optical components and their prices for both the traditional interferometer and AOM DMI.

Traditional interferometers			AOM DMI		
Components	Quantity	Price/ea	Components	Quantity	Price/ea
Two-frequency He-Ne laser	1	$ 8,242.00	Single frequency He-Ne laser	1	$ 3,861.00
Polarizing beam splitter	1	$ 180.00	Acousto-optic modulator	2	$ 697.00
Non-polarizing beam splitter	1	$ 180.00	Modulator driver	2	$ 877.00
Retroreflector	2	$ 275.00	Non-polarizing beam splitter	2	$ 180.00
Right angle prism	1	$ 52.50	Retroreflector	4	$ 275.00
			Right angle prism	8	$ 52.50

Experimental Results

In this section, frequency content of the measurement signal collected using an analog spectrum analyzer for the new setup is presented. Since the beat frequency, or frequency difference between two beams, has been shown to be tunable in the AOM DMI, frequency content of the measurement signal for the reduced-size setup is again reported for two different beat frequencies that are used in commercially-available phase measuring electronics.

Figures 7-14 and 7-15 show the frequency content for constant velocity target motion of 10,000 mm/min for beat frequencies of 3.64 MHz and 20 MHz, respectively. The Doppler frequency for the selected velocity is 0.53 MHz. Only the intended ac interference signal at the Doppler up-shifted frequency for the selected motion direction (+x in Figure 7-9A) is seen. No extra peaks (i.e., leakage induced interference terms) are observed.

The frequency content during oscillatory target motion, where the Doppler frequency can be both up-shifted and down-shifted, is presented. Figures 7-16A and 7-16B show snapshots of power spectra while the target moves in the –x (down-shifted) and +x directions (up-shifted) in Figure 7-9A, respectively. It can be seen that the magnitude of the Doppler frequency is varied with respect to the target velocity. Again, there exists no frequency leakage induced interference terms.

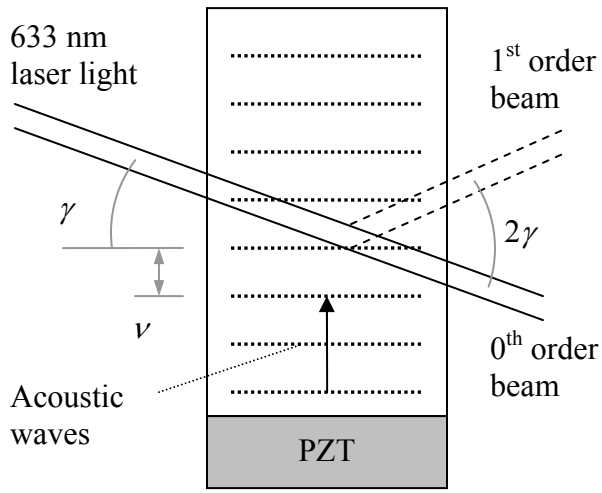

Figure 7-1. Acousto-optic modulator schematic. The incident beam is diffracted into the 0th and 1st order beams.

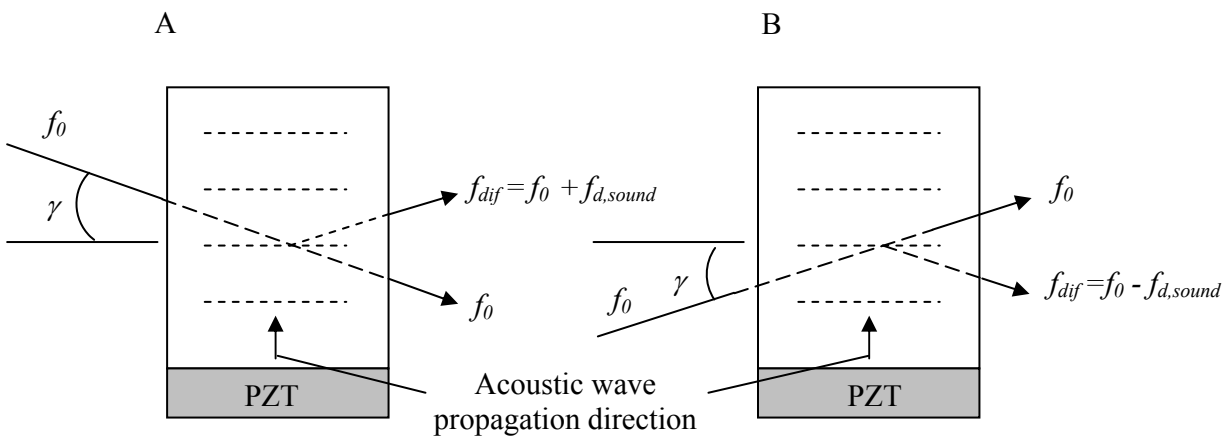

Figure 7-2. Frequency of diffracted beam. A) Up-shifted. B) Down-shifted.

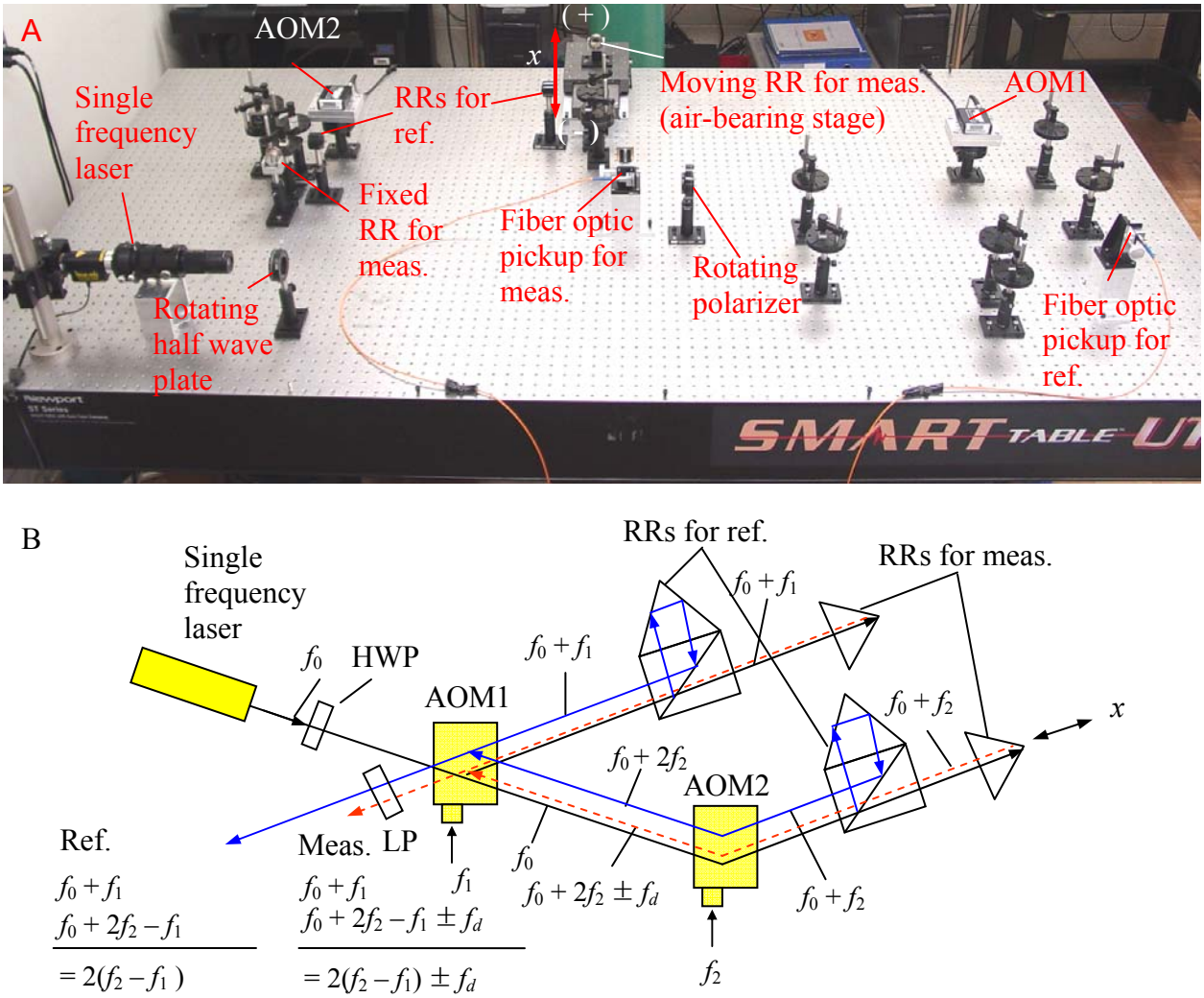

Figure 7-3. AOM DMI setup. A) Experimental setup of heterodyne interferometer using acousto-optic modulators to spatially separate the beams. B) Schematic of acousto-optic modulator based interferometer showing the beam separation and combination at each AOM. (RR is used to abbreviate retroreflector.)

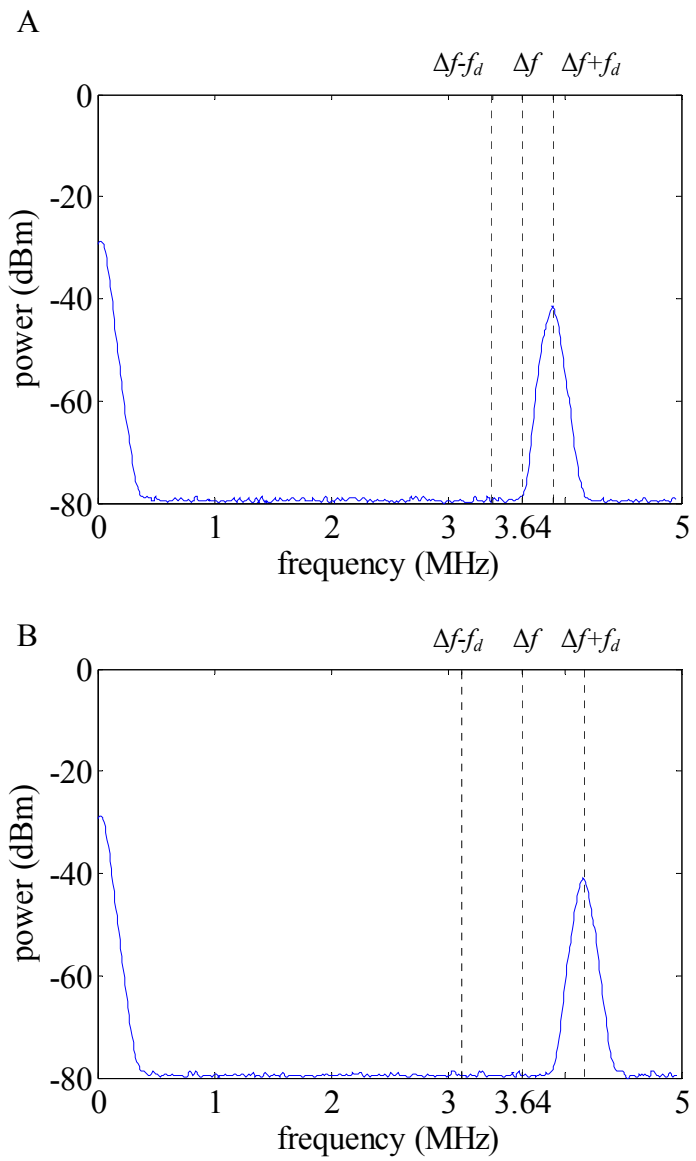

Figure 7-4. Desired *ac interference* term and *dc power* peaks for. A) 5,000 mm/min (f_d = 0.26 MHz). B) 10,000 mm/min (f_d = 0.53 MHz). No other content is present.

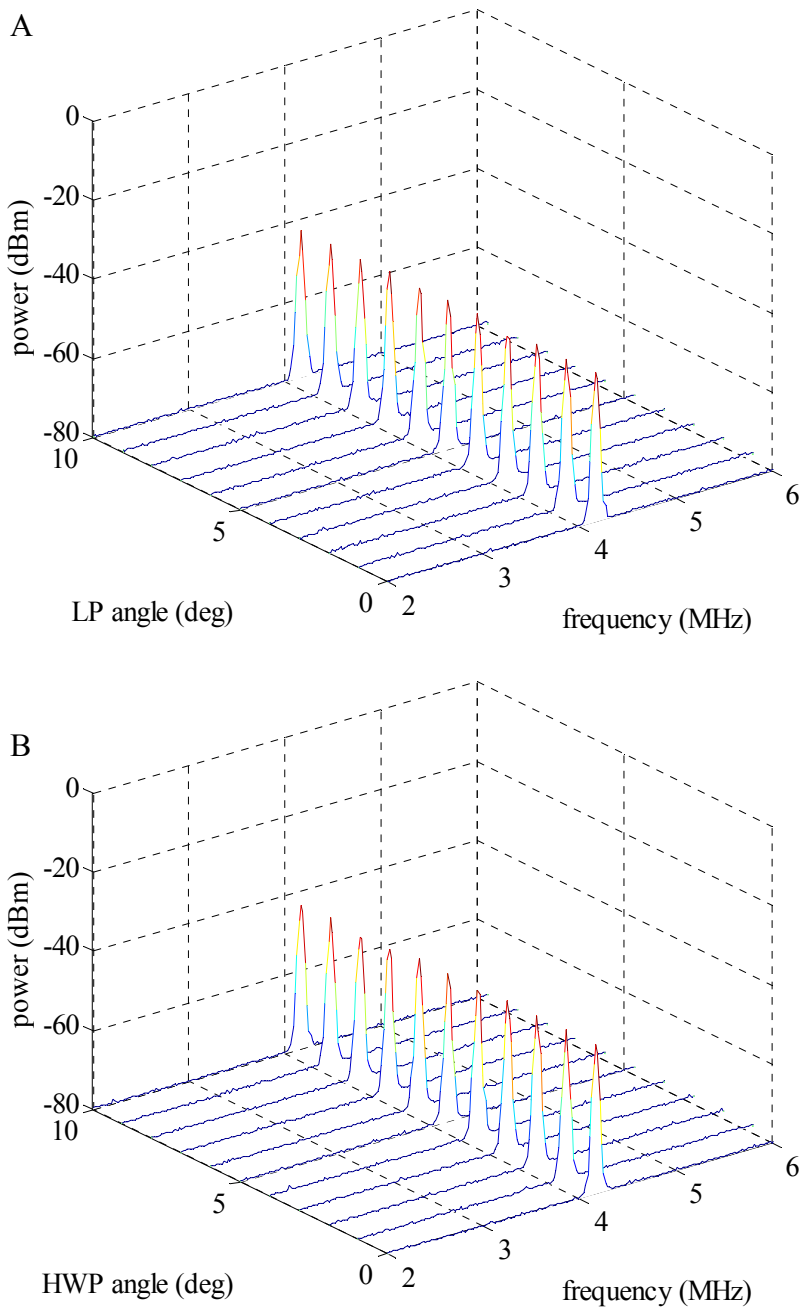

Figure 7-5. No undesired frequency content is present for the AOM DMI. A) Linear polarizer (LP) angle variation. B) Half wave plate (HWP) angle variation.

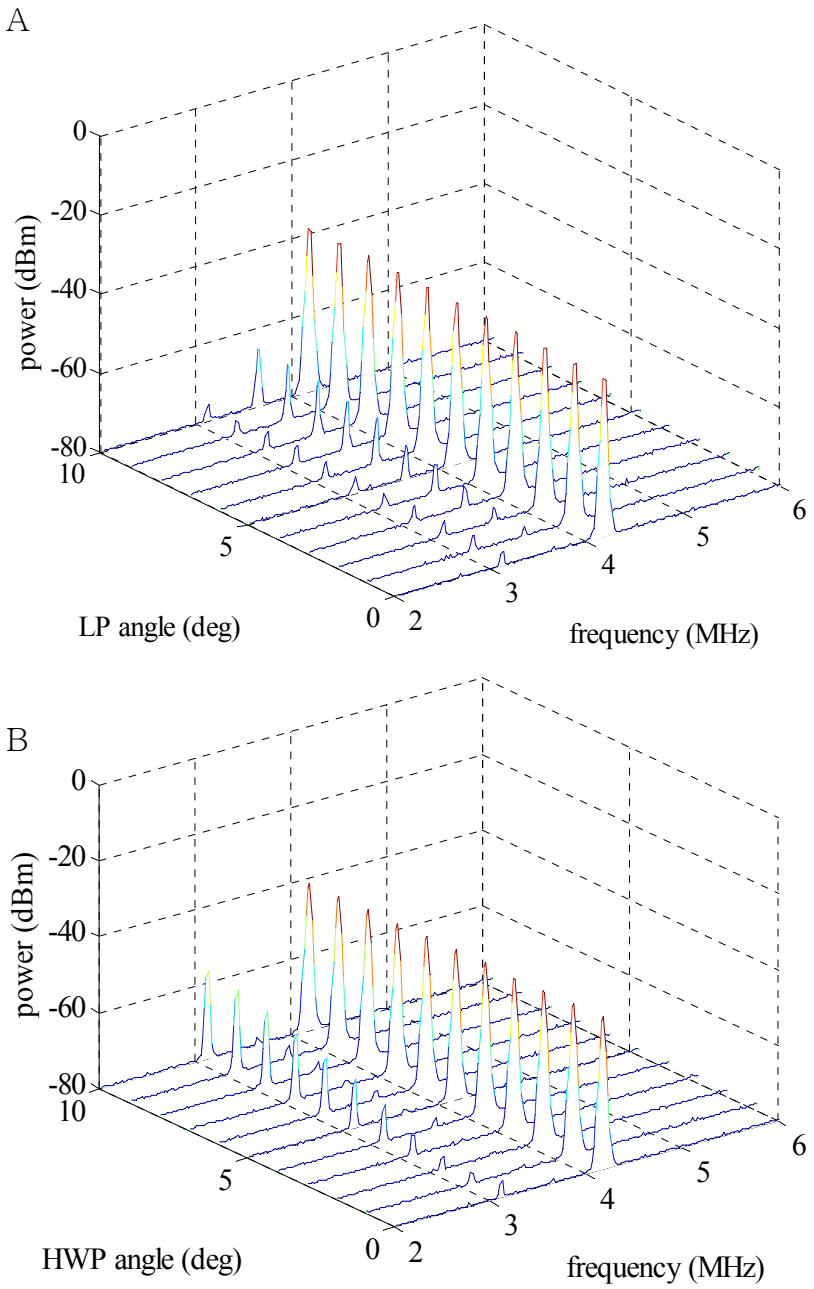

Figure 7-6. Errors for polarization coded DMI. The leakage induced interference terms (*ac reference* and *ac interference*) accompany the desired *ac interference* signal. The data was collected at the same angular orientations as in Figure 7-5. A) Linear polarizer (LP) angle variation. B) Half wave plate (HWP) angle variation.

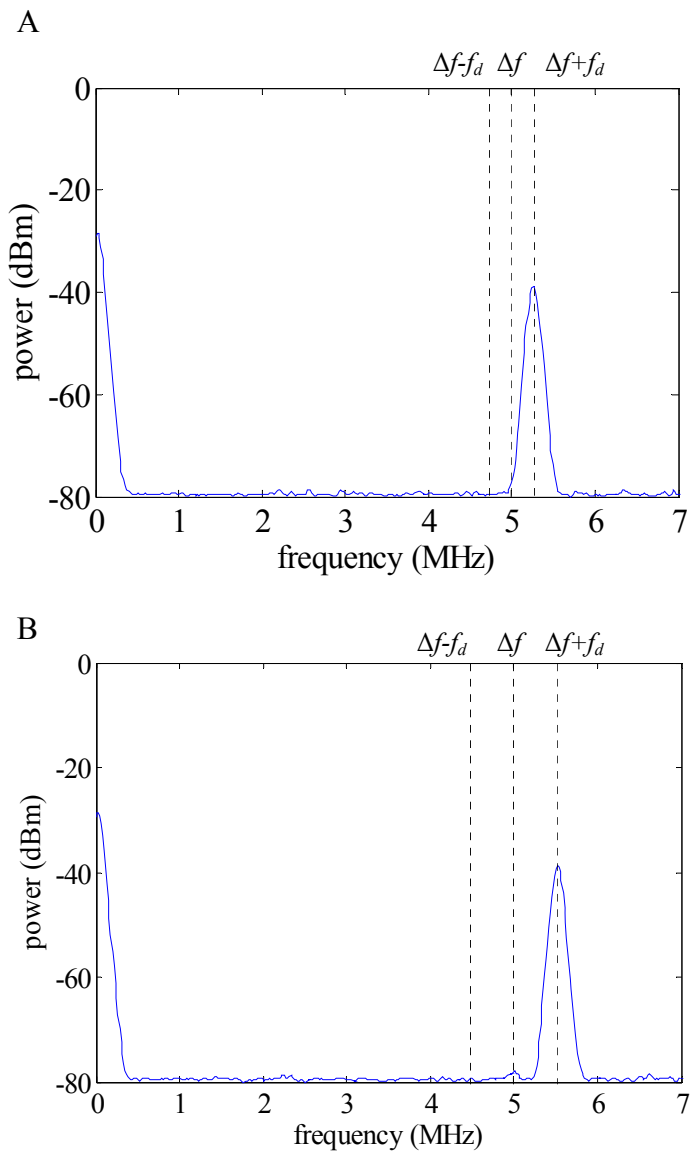

Figure 7-7. Results for the new beat frequency, Δf, of 5 MHz. No periodic error frequency content is observed for two target velocities. A) 5,000 mm/min. B) 10,000 mm/min.

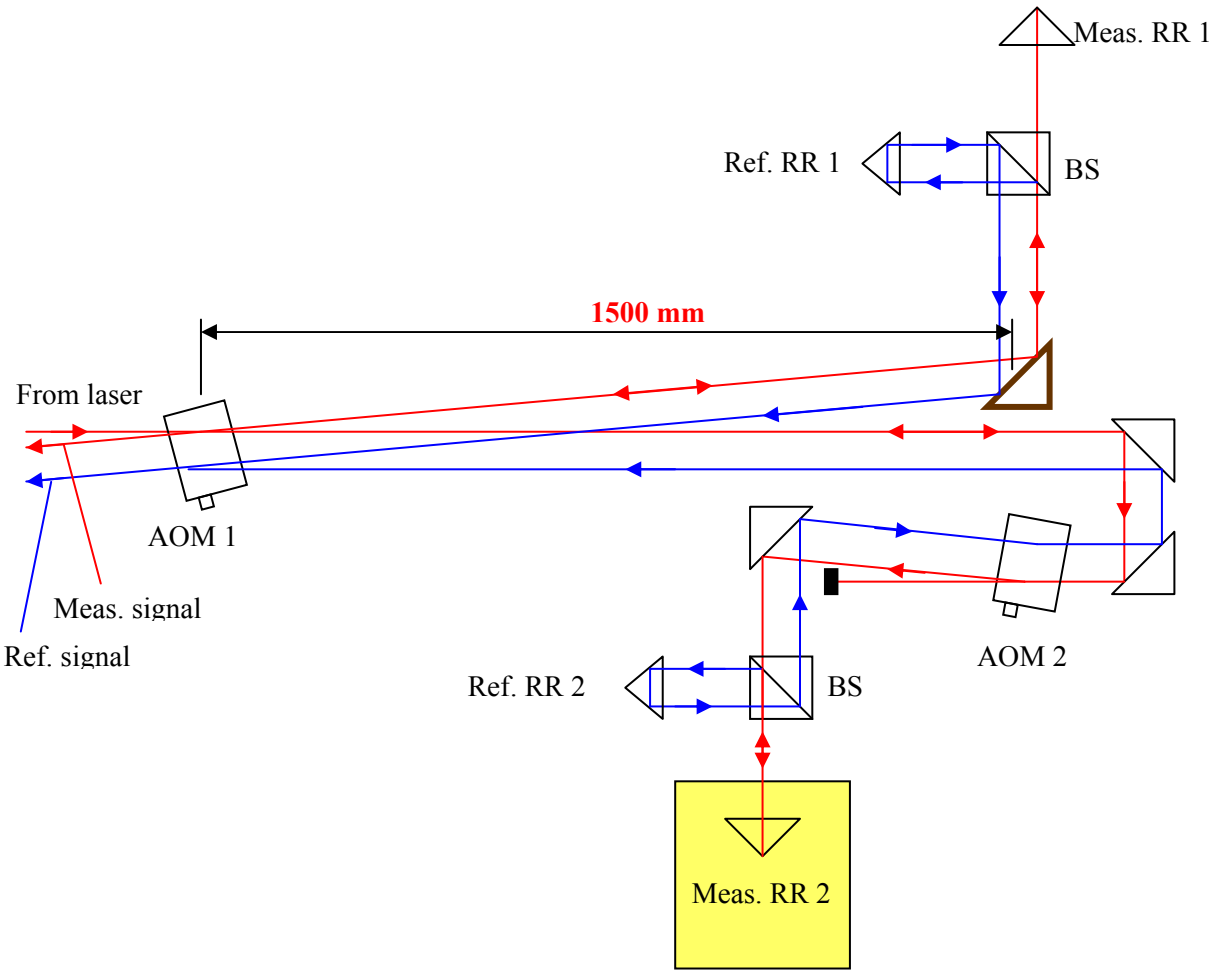

Figure 7-8. Schematic of the current AOM-DMI setup. (RR is used to abbreviate retroreflector.)

A

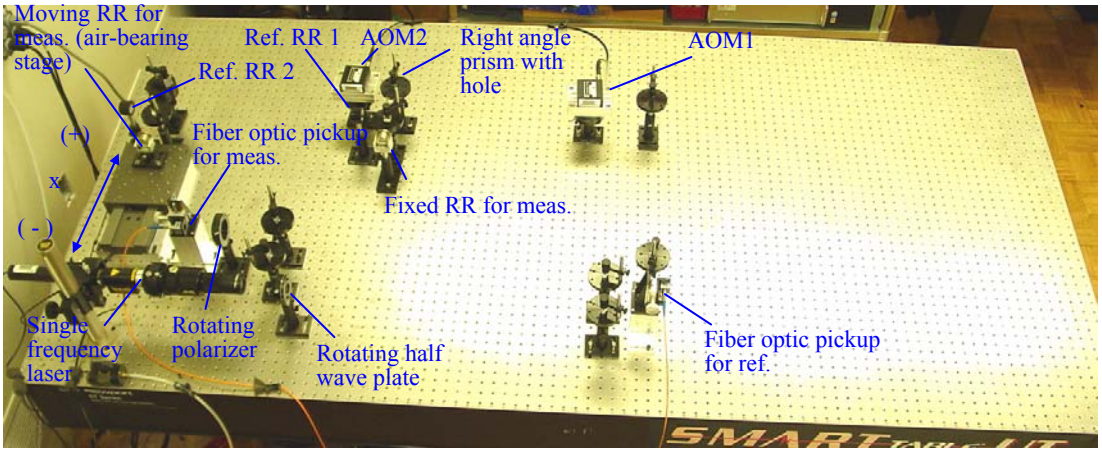

B

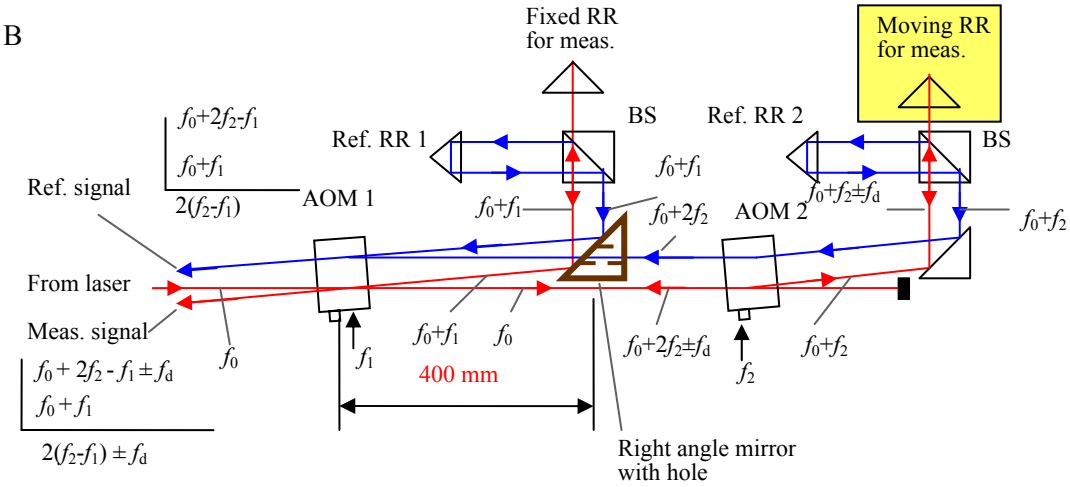

Figure 7-9. Size reduced AOM DMI setup. A) The size reduced setup using the right angle prism with the hole. B) Schematic of the size reduced setup showing the beam separation and combination at each AOM. (RR is used to abbreviate retroreflector.)

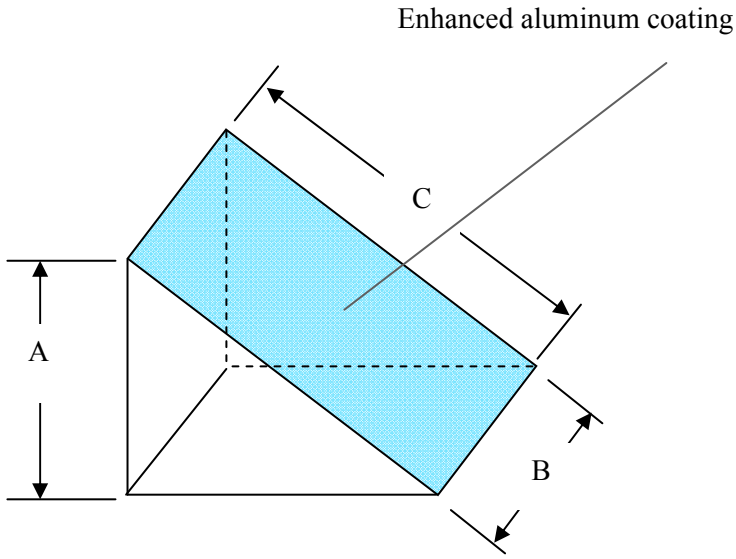

Figure 7-10. Technical drawing for the right angle prism.

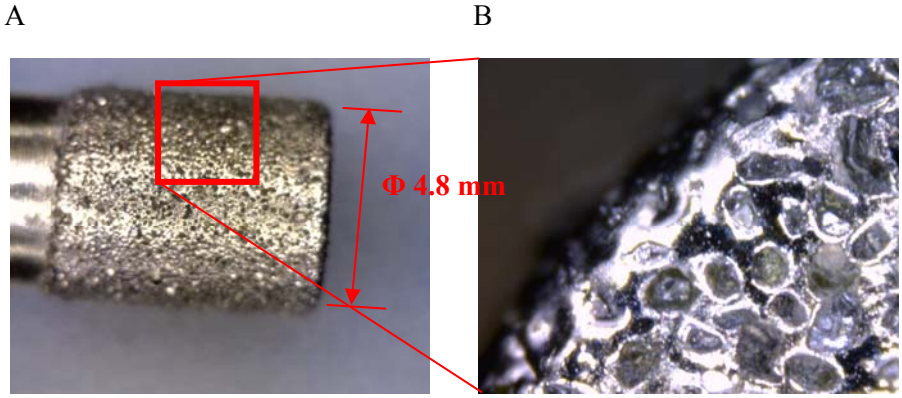

Figure 7-11. An electroplated diamond core drill. A) An electroplated diamond core drill with an outer diameter of 4.8 mm. B) Diamonds coated on the surface of the drill.

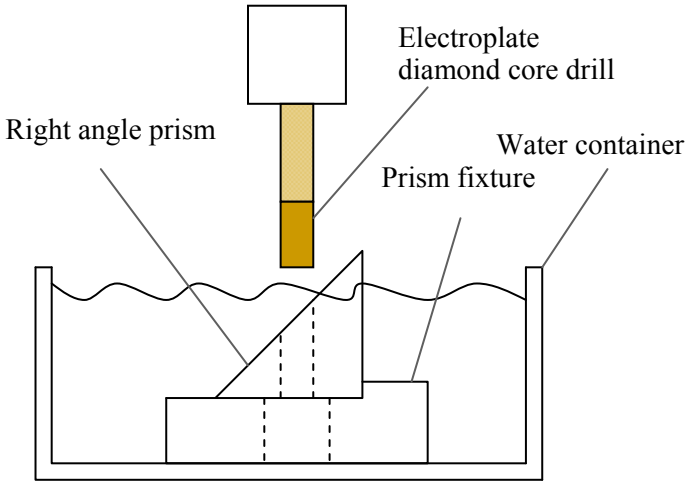

Figure 7-12. Schematic of drilling operation for a right angle prism using a diamond core drill in the submerged (water) environment.

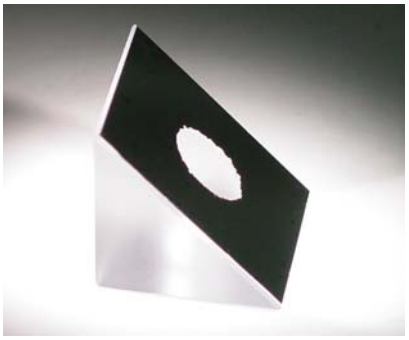

Figure 7-13. The right angle prism with hole at the center. The hole was produced using a diamond core drill.

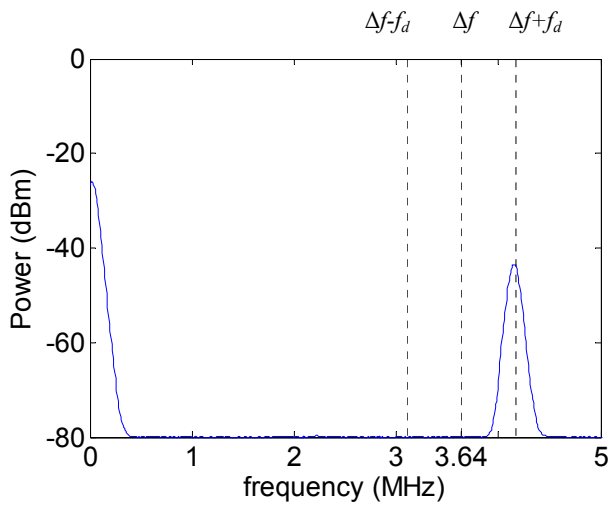

Figure 7-14. Frequency contents of the measurement signal during the constant velocity of 10,000 mm/min (Doppler frequency, f_d, is equal to 0.53 MHz) at the beat frequency, Δf, of 3.64 MHz. Only intended ac interference and optical power terms are present.

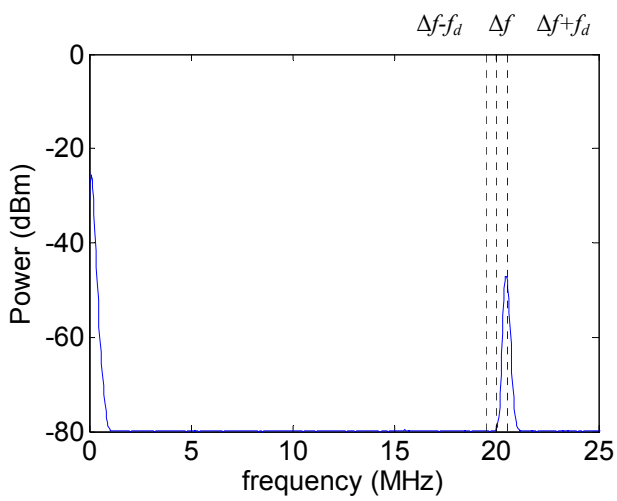

Figure 7-15. Frequency contents of the measurement signal during the constant velocity of 10,000 mm/min (Doppler frequency, f_d, is equal to 0.53 MHz) at the beat frequency, Δf, of 20 MHz. Only intended ac interference and optical power terms are present.

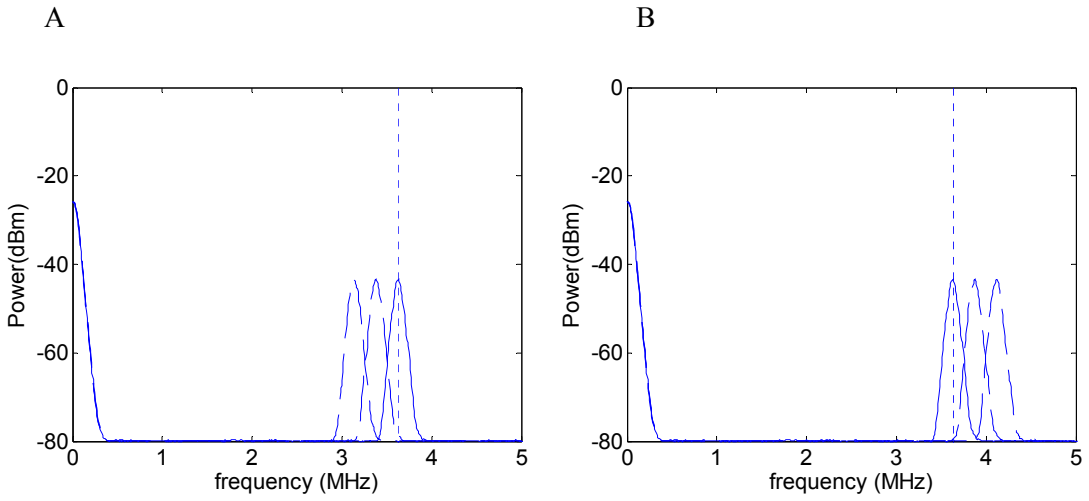

Figure 7-16. Snapshots of power spectra during oscillatory target motion at the beat frequency, Δf, of 3.64 MHz. A) The target moves toward -x direction (Doppler down-shifted). B) The target moves toward +x direction (Doppler up-shifted) in Fig. 9A. Only the intended *ac interference* signals are observed.

CHAPTER 8
CONCLUSIONS

Completed Work

In this research, periodic error in heterodyne interferometry was studied. Periodic error calculation, uncertainty evaluation, and its elimination were investigated. First, a generalized approach was described to calculate periodic error magnitudes by Monte Carlo evaluation. This improved upon prior work [2] where the first and second order error magnitudes were separately calculated. In the new approach, the general case was treated where both the first and second order error components were considered simultaneously. Experiments showed good agreement between the new approach and periodic error magnitudes determined from the discrete Fourier transform of position signals collected using traditional phase measuring electronics.

Second, a single analytical expression for the displacement recorded using a traditional heterodyne interferometer in terms of the various uncertainty contributors was presented. These included: 1) periodic error; 2) Abbe error; 3) cosine error; 4) deadpath error; 5) atmospheric error; 6) material thermal expansion error; 7) laser wavelength stability; and 8) phase nonlinearities from the phase measuring electronics and beam shear. The displacement uncertainty was then evaluated using Monte Carlo simulation. A numerical example demonstrated the well-known cosine error bias, as well as the correction of this bias using the variance in the misalignment angle. In this analysis, the analytical expression reported by Cosijns *et al*. [5] was used to describe the periodic error. Comparisons between the periodic error model and experiments for a variety of frequency mixing conditions were provided

Third, a new displacement measuring interferometer design with no periodic error was demonstrated. In the new design, the two (heterodyne) frequencies were generated and spatially separated using acousto-optic modulators to avoid the potential for frequency mixing. This

contrasted with the traditional setup, where the two optical frequencies are initially coincident with orthogonal polarization states and then separated using polarization dependent optics (polarization coded). Experimental results at multiple target velocities were presented for two arrangements of the new design, which also showed the capability to arbitrarily set the beat frequency. Spectral content was collected using a spectrum analyzer to verify zero periodic error in the new design. These results were compared to data obtained from a traditional polarization coded heterodyne interferometer. It was shown that variations in the optical alignment caused different levels of first and second order periodic error in the traditional setup, but not in the new design. However, the small diffraction angle (7 mrad) between the two beams exiting the acousto-optic modulator caused the large setup size of the initial design. Therefore, the footprint of the new heterodyne displacement measuring interferometer was reduced using a right angle prism with a hole through its center. It is anticipated that the new, periodic error-free interferometer design will enable improved measurement accuracy for various applications, including position feedback for lithographic stepper stages, precision cutting machines, and coordinate measuring machines, as well as transducer calibration, for example.

To summarize, the contributions to periodic error research in the field of displacement measuring interferometry are:

- calculation of first and second order periodic error magnitudes for the general case using spectrum analyzer data;
- evaluation of uncertainty for heterodyne displacement measuring interferometry via Monte Carlo simulation; and
- elimination of periodic error by a new interferometer design.

Future Work

An acousto-optic modulator-based heterodyne displacement measuring interferometer (AOM DMI) realized successful periodic error elimination. Due to the large setup size, the initial

design was modified to reduce the footprint using a right angle prism with a hole at the center. Although the modified design reduced the setup size significantly compared to the original design (65% area reduction), it is still large compared to traditional interferometers. Figures 8-1A and B show setup sizes for both the typical traditional interferometer and the modified AOM DMI, respectively, for single axis measurement. The traditional interferometer setup area (800 mm × 350 mm) is approximately three times smaller than that of the AOM DMI (1400mm × 620 mm).

Acousto-optic devices have been used in lasers for Q-switching [92], laser scanning, and in spectroscopy for frequency control [93] because they provide diffraction, frequency modulation, and intensity modulation of light. For these applications, only the diffracted beam is used and the undiffracted beam is blocked. Therefore, the diffraction angle has not been an issue in these cases. However, the acousto-optic modulator in the new heterodyne displacement measuring interferometer uses both the diffracted and undiffracted beams to generate the interference signal. The size of the new interferometer setup heavily depends on the diffraction angle (as described in Chapter 7). Consequently, research on new acousto-optic modulator designs to increase the beam separation would enable miniaturization of the AOM DMI.

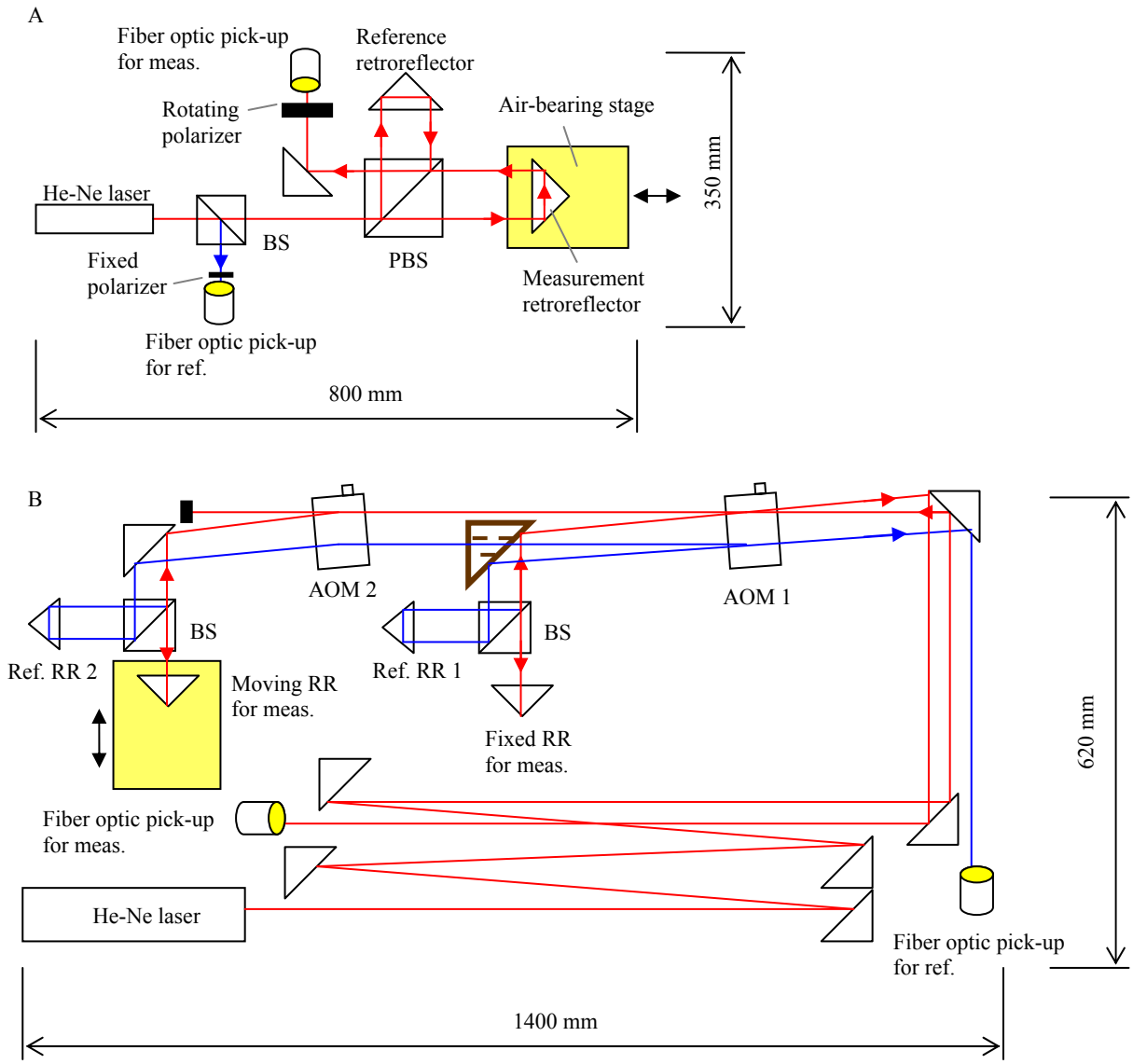

Figure 8-1. Setup size comparison. A) Traditional interferometer (800 mm × 350 mm). B) AOM DMI (1400 mm × 620 mm).

LIST OF REFERENCES

[1] Kim H, Schmitz T, Beckwith J. Periodic error in heterodyne interferometry: Examination and Elimination. In: Halsey D, Raynor W, ed. Handbook of Interferometers: Research, Technology and Applications. Hauppauge, NY: Nova Science; 2009.

[2] Badami V, Patterson S. A frequency domain method for the measurement of nonlinearity in heterodyne interferometry. Precision Engineering 2000; 24(1):41–49.

[3] Donaldson R. Error budgets. In: Hocken R, editor. Technology of Machine Tools. Machine Tool Accuracy, vol. 5. Machine Tool Task Force (UCRL–52960–5); 1980.

[4] Slocum A. Precision Machine Design. Englewood Cliffs, NJ: Prentice Hall; 1992.

[5] Cosijns S, Haitjema H, Schellekens P. Modeling and verifying non-linearities in heterodyne displacement interferometry. Precision Engineering 2002; 26:448–455.

[6] Pedrotti L, Pedrotti M, Pedrotti S. Introduction to Optics, 3rd Ed. New Jersey: Pearson Education; 2007.

[7] Hariharan P. Basics of Interferometry, 2nd Ed. Boston: Academic Press; 2007.

[8] Hlubina P. White-light spectral interferometry with the uncompensated Michelson interferometer and the group refractive index dispersion in fused silica. Optics Communications 2001; 193:1–7.

[9] Eom T, Kim J, Jeong K. The dynamic compensation of nonlinearity in a homodyne laser interferometer. Measurement Science and Technology 2001; 12:1734–1738.

[10] Schmitz T, Houck III L, Chu D, Kalem L. Bench-top setup for validation of real time, digital periodic error correction. Precision Engineering 2006; 30:306–313.

[11] Peggs G, Yacoot A. A review of recent work in sub-nanometer displacement measurement using optical and X-ray interferometry. Philosophical Transactions of the Royal Society of London Series A-Mathematical Physical and Engineering Sciences 2002; 360(1794):953–968.

[12] Schmitz T, Beckwith J. An investigation of two unexplored periodic error sources in differential-path interferometry. Precision Engineering 2002; 27(3):311–322.

[13] Chu D. Alta P. Phase digitizer. United States Patent No. US 6 480 126 B1, 2002

[14] Agilent Technologies. Achieving maximum accuracy and repeatability. Santa Clara, CA 2001.

[15] Edlen B. The refractive index of air. Metrologia 1966; 2:71–80.

[16] Bobroff N. Residual errors in laser interferometry from air turbulence and nonlinearity. Applied Optics 1987; 26(13):2676–2682

[17] Bobroff N. Recent advances in displacement measuring interferometry. Measurement Science and Technology 1993; 4:907–926.

[18] Fedotova G. Analysis of the measurement error of the parameters of mechanical vibrations. Measurement Techniques 1980; 23(7):577–580.

[19] Quenelle R. Nonlinearity in interferometric measurements. Hewlett-Packard Journal 1983; 34(4):10.

[20] Barash V, Fedotova G. Heterodyne interferometer to measure vibration parameters. Measurement Techniques 1984; 27(7):50–51.

[21] Sutton C. Nonlinearity in length measurements using heterodyne laser Michelson interferometry. Journal of Physics E: Scientific Instrumentation 1987; 20:1290–1292.

[22] Estler WT. High-accuracy displacement interferometry in air. Applied Optics 1985; 24:808–815.

[23] Steinmetz C. Sub-micron position measurement and control on precision machine tools with laser interferometry. Precision Engineering 1990; 12(1):12–24.

[24] Oldham N, Kramar J, Hetrick P, Teague, E. Electronic limitations in phase meters for heterodyne interferometry. Precision Engineering 1993; 15(3):173–179.

[25] Demarest F. High-resolution, high-speed, low data age uncertainty, heterodyne displacement measuring interferometer electronics. Measurement Science and Technology 1998; 9: 1024–1030.

[26] Popella B. The influence of the atmosphere on the wavelength of the He-Ne laser and the solution of correction of the laser interferometer. Optica Acta 1972; 19(7):604.

[27] Jones, F. Simplified equation for calculating the refractivity of air. Applied Optics 1980; 19(24): 4129–4130.

[28] Jones F. The refractivity of air. Journal of Research of the National Bureau of Standards 1981; 86:27–32.

[29] Schellekens P, Wilkening G, Reinboth F, Downs M, Birch K, Spronck J. Measurements of the refractive index of air using interference refractometers. Metrologia 1986; 22:279–287.

[30] Birch K, Reinboth F, Ward R, Wilkening G. The effect of variations in the refractive index of industrial air upon the uncertainty of precision length measurement. Metrologia 1993; 30:7–14.

[31] Číp O, Petrů F, Matoušek V, Lazar J. Direct measurement of index of refraction of air by means of high-resolution laser interferometry. Physica Scripta 2005; T118:48–50.

[32] Rosenbluth A, Bobroff N. Optical sources of nonlinearity in heterodyne interferometers. Precision Engineering 1990; 12(1):7–11.

[33] Augustyn W, Davis P. An analysis of polarization mixing errors in distance measuring interferometers. Journal of Vacuum Science and Technology B 1990; 8(6):2032–2036.

[34] Xie Y, Yu Y. Zeeman laser interferometer errors for high precision measurements. Applied Optics 1992; 31(7):881–884.

[35] De Freitas J, Player M. Importance of rotational beam alignment in the generation of second harmonic errors in laser heterodyne interferometry. Measurement Science and Technology 1993; 4:1173–1176.

[36] Hou W, Zhao X. Drift of nonlinearity in the heterodyne interferometer. Precision Engineering 1994; 16(1):25–35.

[37] De Freitas J, Player M. Polarization effects in heterodyne interferometry. Journal of Modern Optics 1995; 42(9):1875–1899.

[38] Howard L, Stone J. Computer modeling of heterodyne interferometer errors. Precision Engineering 1995; 12(1):143–146.

[39] Wu C, Su C. Nonlinearity in measurements of length by optical interferometry. Measurement Science and Technology 1996; 7:62–68.

[40] Park B, Eom T, Chung M. Polarization properties of cube-corner retroreflectors and their effects on signal strength and nonlinearity in heterodyne interferometers. Applied Optics 1996; 35(22):4372–4380.

[41] De Freitas J. Analysis of laser source birefringence and dichroism on nonlinearity in heterodyne interferometry. Measurement Science and Technology 1997; 8:1356–1359.

[42] Li B, Liang J. Effects of polarization mixing on the dual-wavelength heterodyne interferometer. Applied Optics 1997; 36(16):3668–3672.

[43] Wu C, Deslattes R. Analytical modeling of the periodic nonlinearity in heterodyne interferometry. Applied Optics 1998; 37(28):6696–6700.

[44] Petrů F, Číp O. Problems regarding linearity of data of a laser interferometer with a single-frequency laser. Precision Engineering 1999; 23(1):39–50.

[45] Dubovitsky S, Lay O., Seidel D. Elimination of heterodyne interferometer nonlinearity by carrier phase modulation. Optics Letters 2002; 27(8): 619–621.

[46] Zhao H, Zhang G. Nonlinear error by orientation and elliptic polarization in a two-beam interferometer. Optical Engineering 2002; 41:3204–3208.

[47] Wu C. Subdivision of Nonlinearity in Heterodyne Interferometers. Fringe 2005 The 5th International Workshop on Automatic Processing of Fringe Patterns. Springer Berlin Heidelberg ISBN 978-3-540-26037-0 2006; 327–333.

[48] Hou W. Optical parts and the nonlinearity in heterodyne interferometers. Precision Engineering 2006; 30(3):337–346.

[49] Stone J, Howard L. A simple technique for observing periodic nonlinearities in Michelson interferometers. Precision Engineering 1998; 22(4):220–232.

[50] Yin CY, Dai GL, Chao ZX, Xu Y, Xu J. Determining the residual nonlinearity of a high-precision heterodyne interferometer. Optical Engineering 1999; 38(8):1361–1365.

[51] Loner D, Knarren B, Cosijns S, Haitjema H, Schellekens P. Laser polarization state measurement in heterodyne interferometry. Annals of the CIRP 2003; 52(1):439–442.

[52] Knarren B, Cosijns S, Haitjema H, Schellekens P. Fiber characterization for application in heterodyne laser interferometry with nanometer uncertainty, part I: polarization state measurements. Optical Engineering 2005; 44(2):025002.

[53] Knarren B, Cosijns S, Haitjema H, Schellekens P. Fiber characterization for application in heterodyne laser interferometry with nanometer uncertainty, part II: modeling and analysis. Optical Engineering 2005; 44(2):025003.

[54] Topcu S, Chassagne L, Alayli Y, Juncar P. Improving the accuracy of homodyne Michelson interferometers using polarization state measurement techniques. Optics Communications 2005; 247(1-3): 133–139.

[55] Kim, H.S. and Schmitz, T., 2009, Periodic Error Calculation from Spectrum Analyzer Data, Precision Engineering, doi:10.1016/j.precisioneng.2009.06.001.

[56] Tanaka M, Yamagami T, Nakayama K. Linear interpolation of periodic error in a heterodyne laser interferometer at subnanometer levels. IEEE Transactions on Instrumentation and Measurement 1989; 38(2):552–554.

[57] Hou W, Wilkening G. Investigation and compensation of the nonlinearity of heterodyne interferometers. Precision Engineering 1992; 14(2):91–98.

[58] Patterson S, Beckwith J. Reduction of systematic errors in heterodyne interferometric displacement measurement, In: Proceedings of the 8th International Precision Engineering Seminar (IPES), Compiegne, France, 1995. pp. 101–104.

[59] Wu C, Su C. Nonlinearity in measurements of length by optical interferometry. Measurement Science and Technology 1996; 7(1):62–68.

[60] Wu C, Su C and Peng G-S. Correction of nonlinearity in one-frequency optical interferometry. Measurement Science and Technology 1996; 7(4):520–524.

[61] Wu C, Lawall J, Deslattes R. Heterodyne interferometer with subatomic periodic nonlinearity. Applied Optics 1999; 38(19):4089–4094.

[62] Nakatani N. Heterodyne interferometers using orthogonally polarized and two-frequency shifted light sources with super-high extinction ratio. Optical Review 1999; 6(5):443–448.

[63] Lawall J, Kessler E. Michelson interferometry with 10 pm accuracy. Review of Scientific Instruments 2000; 71(7):2669–2676.

[64] Guo J, Zhang Y, Shen S. Compensation of nonlinearity in a new optical heterodyne interferometer with doubled measurement resolution. Optics Communications 2000; 184(1–4):49-55.

[65] Wang C, Augousti A, Mason J. Real time evaluation and correction of nonlinear errors in single frequency interferometers. Transactions of the Institute of Measurement and Control 2000; 22(5):405–412.

[66] Schmitz T, Beckwith J. Acousto-optic displacement-measuring interferometer: a new heterodyne interferometer with Ångstrom-level periodic error. Journal of Modern Optics 2002; 49(13):2105–2114.

[67] Wu C, Lin S, Fu J. Heterodyne interferometer with two spatial separated polarization beams for nanometrology. Optical and Quantum Electronics 2002; 34:1267–1276.

[68] Eom T, Choi T, Lee K, Choi H, Lee S. A simple method for the compensation of the nonlinearity in the heterodyne interferometer. Measurement Science and Technology 2002; 13:222–225.

[69] Yeh H-C, Ni W-T, Pan S-S. Real-time motion control with subnanometer heterodyne interferometry. International Journal of Modern Physics D: Gravitation, Astrophysics and Cosmology 2002; 11(7):1087–1099.

[70] Halverson P, Spero R. Signal processing and testing of displacement metrology gauges with picometre-scale cyclic nonlinearity. Journal of Optics A-Pure and Applied Optics 2002; 4(6):S304–S310.

[71] Bitou Y. Polarization mixing error reduction in a two-beam interferometer. Optical Review 2002; 9(5):227–229.

[72] Lay O, Dubovitsky S. Polarization compensation: a passive approach to reducing heterodyne interferometer nonlinearity. Optics Letters 2002; 27(10):797–799.

[73] Wu C. Periodic nonlinearity resulting from ghost reflections in heterodyne interferometry. Optics Communications 2003; 215(1-3):17–23.

[74] Li Z, Herrmann K, Pohlenz F. A neural network approach to correcting nonlinearity in optical interferometers. Measurement Science and Technology 2003; 14(3):376–381.

[75] Dai G, Pohlenz F, Danzebrink H-U, Hasche K, Wilkening G. Improving the performance of interferometers in metrological scanning probe microscopes. Measurement Science and Technology 2004; 15:444–450.

[76] Keem T, Gonda S, Misumi I, Huang QX, Kurosawa T. Removing nonlinearity of a homodyne interferometer by adjusting the gains of its quadrature detector systems. Applied Optics 2004; 43(12):2443–2448.

[77] Keem T, Gonda S, Misumi I, Huang QX, Kurosawa T. Simple, real-time method for removing the cyclic error of a homodyne interferometer with a quadrature detector system. Applied Optics 2005; 44(17):3492–3498.

[78] Schmitz T, Chu D, Houck III L. First order periodic error correction: Validation for constant and non-constant velocities with variable error magnitudes. Measurement Science and Technology 2006; 17: 3195–3203.

[79] Hong M, Jeon J, Park K, You K. Adaptive nonlinearity compensation of heterodyne laser interferometer. Knowledge-based Intelligent Information and Engineering Systems, Part 2, Proceedings 2006; 4252:545–552.

[80] Číp O, Petrů F, Buchta Z, Lazar J. Small displacement measurements with subatomic resolution by beat frequency measurements. Measurement Science and Technology 2007; 18:2005–2013.

[81] Olyaee S, Nejad SM. Nonlinearity and frequency-path modelling of three-longitudinal-mode nanometric displacement measurement system. IET Optoelectronics 2007; 1(5): 211–220.

[82] Teng H, Lang K. Heterodyne interferometer for displacement measurement with amplitude quadrature and noise suppression. Optics Communications 2007; 280(1): 16–22.

[83] Schmitz T, Evans C, Davies A, Estler WT. Displacement uncertainty in interferometric radius measurements. Annals of the CIRP 2002; 51(1):451–454.

[84] Schmitz T, Kim HS. Monte Carlo evaluation of periodic error uncertainty. Precision Engineering 2007; 31(3):251–259.

[85] Wu C, Su C, Peng G, Huang Y. Polarimetric, nonlinearity-free, homodyne interferometer for vibration measurement. Metrologia 1996; 33(6):533–537.

[86] Köning R, Dixson R, Fu J, Vorburger T. The role of periodic interferometer errors in the calibration of capacitance displacement sensors for nanometrology applications. Measurement Science and Technology 2001; 12: 2002–2008.

[87] Wu C. Heterodyne interferometric system with subnanometer accuracy for measurement of straightness. Applied Optics 2004; 43(19):3812–3816.

[88] Evans C, Holmes M, Demarest F, Newton D, Stein A. Metrology and calibration of a long travel stage. Annals of the CIRP 2005; 54(1):495–498.

[89] Deng Y, Li XJ, Wu YB, Hu JG, Yao JQ. Analysis of frequency mixing error on heterodyne interferometric ellipsometry. Measurement Science and Technology 2007; 18(11):3339–3343.

[90] International Organization for Standardization (ISO). Guide to the Expression of Uncertainty in Measurement. Geneva 1995.

[91] Taylor B, Kuyatt C. NIST Technical Note 1297 Guidelines for Evaluating and Expressing the Uncertainty of NIST Measurement Results. Gaithersburg, MD 1994.

[92] Lekavich J. Acousto-optic beam modulators and deflectors control laser beams in many applications. Lasers & Applications 1986; April:59–64.

[93] Chang IC. Acousto-optic devices and applications. In: Bass M, Stryland E, Williams D, Wolfe W, 2nd Ed. Handbook of Optics. New York, NY: McGraw-Hill; 1995.

BIOGRAPHICAL SKETCH

The author was born in Changnyeong, Kyeongnam Korea in 1976. After finishing his middle school education at his hometown, he went to Changwon where he completed his high school education. He remained there to pursue his undergraduate degree in mechanical engineering at Changwon National University (CNU). At CNU, he received a full scholarship, including tuition waiver and stipend, throughout his undergraduate studies. As a mandatory requirement, he served in the military (Republic of Korea Navy) for 28 months. While studying at CNU, he was sponsored by the project named Brain Korea 21st to go to University of Nebraska for one year as a full scholar exchange student. After graduation, the author worked for three years before joining the Ph.D. program at University of Florida (UF), where he was awarded a UF Alumni Fellowship. During his Ph.D. studies, he received several honors including the NAMRI/SME Outstanding Paper Finalist Award, Samsung Electromechanical 4th 1nside Edge International Paper Competition Silver Prize, Student Scholarship for the Annual American Society for Precision Engineering Conference, and a UF Outstanding Academic Achievement Award. The author plans to seek a university faculty position after graduation.